Time resolved photoelectron spectroscopy with ultrafast soft x-ray light

by

Lora Nugent-Glandorf

B.S., Wheaton College, 1996

A thesis submitted to the
Faculty of the Graduate School of the
University of Colorado in partial fulfillment
of the requirements for the degree of
Doctor of Philosophy
Department of Chemistry and Biochemistry
2001

This thesis entitled:
Time resolved photoelectron spectroscopy with ultrafast soft x-ray light
written by Lora Nugent-Glandorf
has been approved for the Department of Chemistry and Biochemistry

Stephen R. Leone

Prof. W. Carl Lineberger

Date

The final copy of this thesis has been examined by the signatories, and we find that both the content and the form meet acceptable presentation standards of scholarly work in the above mentioned discipline.

Nugent-Glandorf, Lora (Ph.D., Physical Chemistry)

Time resolved photoelectron spectroscopy with ultrafast soft x-ray light

Thesis directed by Prof. Stephen R. Leone

Understanding the nature of chemical bonding in molecules has long been of fundamental interest, and manipulating specific chemical bonds has found practical potential in many areas, such as polymer chemistry, biophysics, and genetics. Photoelectron spectroscopy (using photons to eject electrons from a molecule to determine electron energies and bonding properties) has been a proven technique for gaining insight into the electronic structure of the simplest atoms to large molecules. Here, I describe experiments designed to investigate bonding in a simple molecule (Br_2) by measuring electronically excited molecular states and dissociative transient electronic states via time-resolved photoelectron spectroscopy with soft x-ray light. High-harmonic generation produces a novel, femtosecond source of soft x-rays by focusing an ultrafast 800 nm Ti:Sapphire laser into a rare gas jet. I outline the details of the experimental apparatus, including the optical layout, two-grating separation and compression of the high-harmonic pulses, and the magnetic bottle photoelectron spectrometer. The feasibility of using the generated soft x-ray pulses for photoelectron spectroscopy is established, and the spectral and temporal nature of the pulses are determined. The photoelectron spectrum of the bound excited B state of neutral Br_2 is measured and the issues involved in ionization from excited electronic states is discussed. The time-resolved dissociation of the excited C state of Br_2 is observed using a visible pump (400 nm) and a soft x-ray probe. Key results point to challenging new problems involving the cross-sections and shapes of photoelectron features arising from dissociating states, as well as understanding the role of cross-correlation processes versus dissociative wavepacket signals. UV-pump/soft x-ray probe photoelectron spectroscopy promises to offer a unique and powerful way to probe excited electronic states and dissociation dynamics of neutral molecules in the gas phase on ultrafast time scales.

Acknowledgements

First of all, I would like to thank my advisor, Steve Leone, who is largely responsible for making my graduate school experience a positive one. Not only was this project originally formed from his ideas, but has also seen success due to his advice, knowledge and experience. Steve has been a great advisor on all fronts, from the technical and conceptual realm to personal advice for career and life in general. For all this, and for his continuing support of me as a scientist, I am very grateful. Thanks also to Ronnie Bierbaum, my co-advisor, for her help and support.

I would also like to recognize OSEP, the Optical Science and Engineering Program at CU, for continuing financial support and the opportunity to do a research internship. I chose to do my internship with Dr. Richard Haight, an IBM researcher at the T.J. Watson Research Center in Yorktown Heights, NY. I am also indebted to Rich for his patience, advice, time and the opportunity to work for him. Funding for this project was received from the Air Force Office of Scientific Research, as well as additional equipment purchased with specific grants from the National Science Foundation.

Next, there are all the people who worked with me over the last 4+ years on this project. In the beginning, MK and Jen made a great team to work with as we attempted to make an empty room into some semblance of an experiment, as well as providing a great deal of comic relief. Next came Mike Scheer, whose brains and quintessential german-ness made the x-ray project into the great instrument it is today. The bulk of the data presented here was a result of Mike and I working together. During my absence in New York, I should thank Tobias Voss

for his work in the lab and for keeping Mike in check while I was away. Along the way we were happy to have Ed Grant and Xeuming Yang, both visiting professors to JILA, work with us while on sabbatical. Also thanks to Anneliese, a pre-grad student and a good friend for her work on Al_2Br_6. Thanks also goes to David Samuels, the grad student who joined the project a year ago, for his hard work in the lab in the last months and for the new ideas he brings to the project. And to all the Leone group, past and present, thanks for all your free advice, patience and friendships. Other key players in the realization of this experiment were Hans Green, Blaine Horner and Dave Alchenberger from the instrument shop, and Paul Buckingham and James Fung-a-Fat from the electronics shop. To all the support staff at JILA, thank you for making this such a great place to do science!

To those teachers in the past who encouraged me in many ways, Mr. Warren Pettit, Dr. Brian Miller, Dr. Narl Hung, and Dr. Mark Niemchzeck, thank you for your influence on my life and career.

There is no room to thank all my friends who have helped me survive grad school in various ways, but I am overwhelmingly grateful to all of you. Special thanks and love to Paula, Allie, and Tara for great times at Tuesday lunches which kept me going, and to Jen and Sara for continuing to be good friends and always making me laugh. To Kitty, my only friend at IBM, thanks for helping me survive life away from home. And to the Bible study folks, you have been a great encouragement to me in my personal and spiritual life, which has helped me to be a better person.

Of course, I can't go without mentioning my husband Dave, who has provided me with unconditional love and support through our 5 years of marriage, and who is my inspiration. And to my family, my parents and sister and brother and their families, for always welcoming me home and for their constant encouragement and love, I am forever thankful for all of you.

Contents

Chapter

Appendix

Tables

Table

Figures

Figure

Chapter 1

Introduction

1.1 Background

Since the discovery of the atom and its structure, consisting of a nucleus containing smaller particles (neutrons and protons) and electrons which surround the nucleus, scientists have been studying the electronic structure of atoms and molecules. More specifically, the field of quantum mechanics has attempted to understand electronic structure, among other things, and how it relates to the chemical bonds that are formed between atoms. Fundamentally, understanding the nature of chemical bonding is important for the advancement of science. Many practical uses stemming from our knowledge of chemical bonds exist as well in all fields of science, from understanding the gene sequences in DNA to controlling chemical reactions in the atmosphere that cause pollution.

To get at the fundamental electronic structure underlying bonding in molecules, scientists have long relied on the experimental technique of photoelectron spectroscopy. Photons are used to eject electrons from molecules or atoms (termed 'ionization'), and the energy of the electrons is used to infer orbital energies, or discreet energy levels of the electrons in a molecule. When atoms come together to form molecules, the electrons in the outer shell (or valence orbitals) are primarily responsible for the formation of chemical bonds. By ejecting these electrons via photoelectron spectroscopy, it is possible to better understand how atomic orbitals become molecular orbitals. Fig. 1.1 is a simplistic picture of two atoms with one specific orbital energy coming together to form two molecular orbitals. In a simplified view, the electrons in these outer

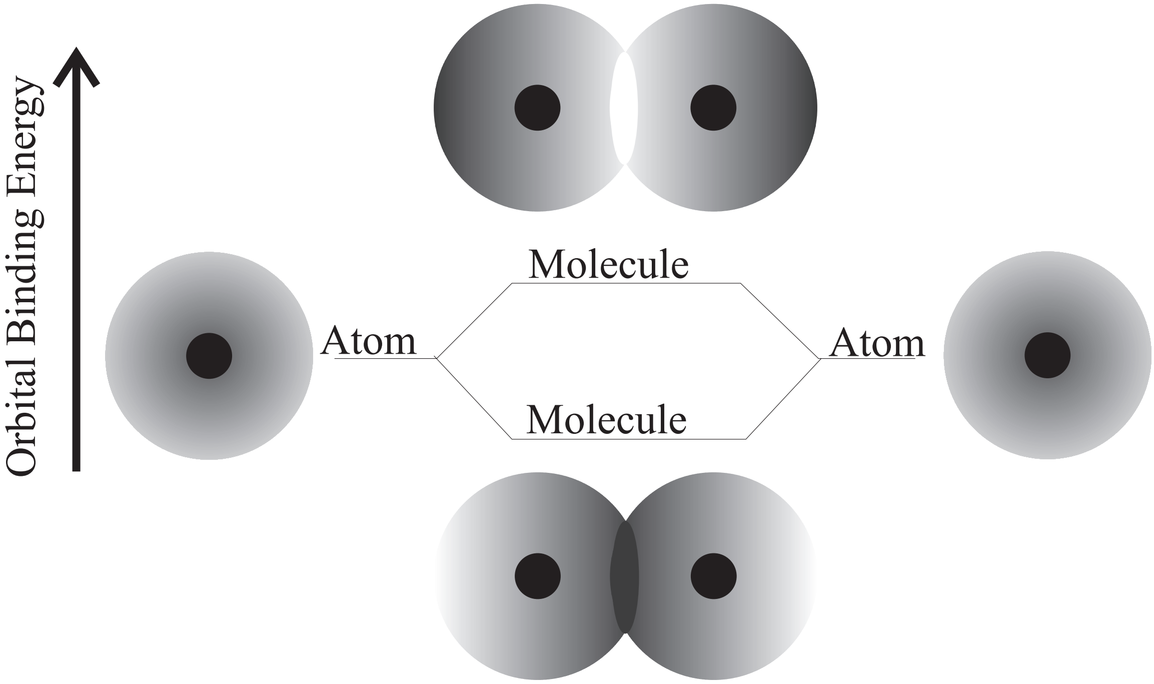

Figure 1.1: A simple molecular orbital picture demonstrating two atoms coming together to form two molecular orbitals.

molecular orbitals now share the space around the two nuclei. In a multi- electron system, a series of molecular orbitals are formed, from the core orbitals (the electrons close to the nucleus) to the valence orbitals (the electrons furthest away from the nucleus and largely responsible for bonding).

In photoelectron spectroscopy, when a photon with a particular energy interacts with a molecule, an electron is ejected, as is demonstrated in Fig. 1.2. To eject a valence or outer electron with a small binding energy, a lower energy photon is sufficient. To eject a core or inner electron with a large binding energy, a higher energy photon is needed. This leads to the conservation of energy given by the equation:

$$\hbar\nu = E_{pe} + I_i \tag{1.1}$$

where $\hbar\nu$ is the photon energy, E_{pe} is the energy of the ejected photoelectron and I_i is the ionization energy, or binding energy of the orbital i. Equation 1.1 is an approximation resulting from Koopmans' theorem, which states that the ionization energy is equal to the orbital energy of the ejected electron. This neglects the fact that the remaining electrons rearrange their distributions when ionization occurs [1].

There are several ways experimentally to measure the energy of the ionized electron in photoelectron spectroscopy. An electrostatic analyzer utilizes the fact that the energy of the electron is related to its velocity, as is given by the extension of equation 1.1 to:

$$E_{pe} = \frac{1}{2}mv^2, \tag{1.2}$$

where v is the velocity of the electron and m is the mass. The electrostatic analyzer consists of two charged plates bent at an angle. When these plates are held at a certain voltage, the deflection path of the electron depends on its speed, and electrons with different speeds will make it through the analyzer to the detector as the voltages are changed (Fig. 1.3(a)). If the voltages are ramped in a consistent way, a full photoelectron spectrum can be obtained. Another common method of analyzing the energies of photoelectrons is with a time-of-flight tube. Here,

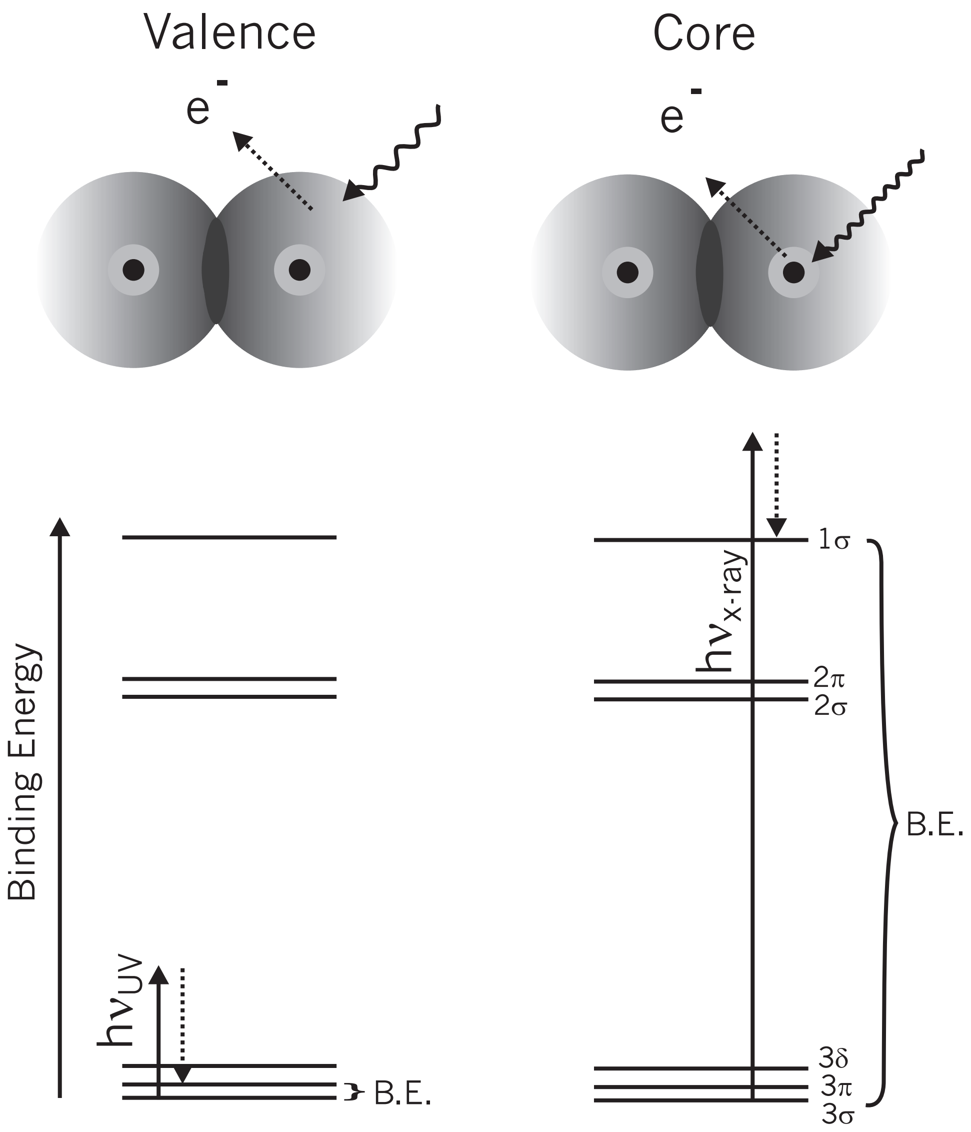

Figure 1.2: **Top:** A pictorial representation of a valence electron being ejected from a valence or bonding orbital with an ultraviolet (UV) photon, and a core electron being ejected from an inner orbital with an x-ray photon. **Bottom:** The electron energy level diagram of the above pictures. On the left, the UV photon has sufficient energy to eject the 3π electron. On the right, a x-ray photon is needed to eject the 1σ electron. The dotted arrows represent the energy of the ejected photoelectron. Binding energy (B.E.) is defined as the energy with which an electron is bound to the nucleus.

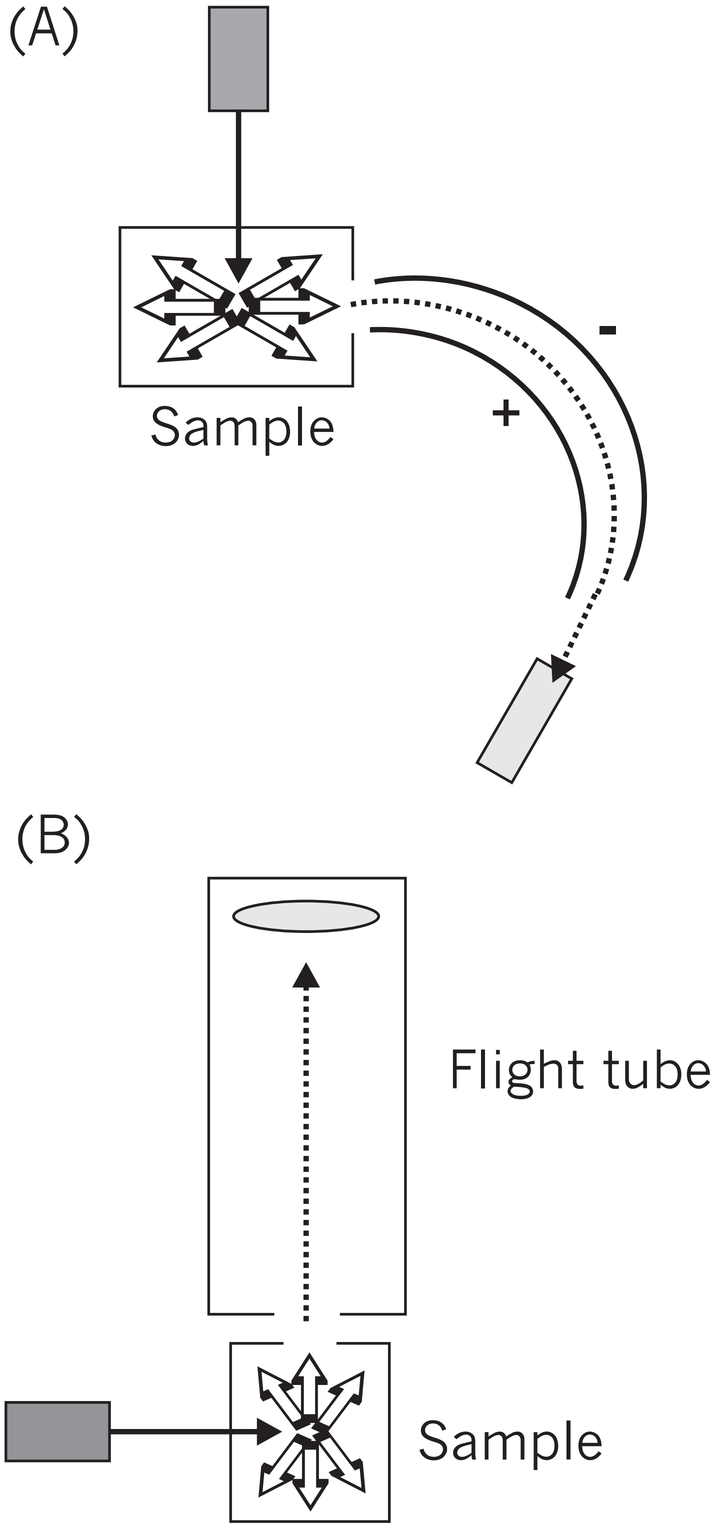

Figure 1.3: (A) A schematic of an electrostatic analyzer where electrons are energy separated by their velocities. Objects shaded with dark gray represent the photon source and the light gray objects are the detectors. The dotted line represents the electron path through the analyzer. (B) A time-of-flight photoelectron analyzer where electrons are energy separated by their arrival time to the detector.

electrons are energy separated based on the arrival time of the electrons to a fast response detector at the end of a long flight tube (Fig. 1.3(b)). The time of arrival is related to the energy of the electrons by further expanding equation 1.2:

$$E_{pe} = \frac{1}{2}m\left(\frac{d}{t}\right)^2, \tag{1.3}$$

where d is the distance traveled by the electron (usually fixed) and t is the time-of-flight. The latter is the type of energy analysis used for the data presented in this thesis.

The technique of photoelectron spectroscopy has several variations. First, the probe wavelength is scanned and total photoelectron signal is detected. Here an enhancement in the signal occurs when the incident photon energy is equal to an electronic or vibrational resonance in the atom or molecule under study, and often has similar features as in an absorption spectrum. A further extension of this first technique is to allow fast kinetic energy photoelectrons to escape and collect the low kinetic energy electrons so that only threshold resonances are measured. A second type of measurement fixes the probe wavelength and scans the energies of the photoelectrons. The energies of the photoelectrons in turn reflect the binding energies of the electrons in the atom or molecule. Coincidence methods are included in this second category, where the electron energies are scanned in coincidence with an ion of a certain mass.

For ultraviolet photoelectron spectroscopy, the He (I) lamp was once the most common light source used. It produces radiation at 584 Å, or 21.2 eV. This photon energy is enough to ionize the electrons in the valence orbitals for almost any molecule. Now, synchrotron light sources are the predominant choice as described below. An example of the ultraviolet photoelectron spectrum of a simple molecule is given in Fig. 1.4, where the photon energy is fixed and the photoelectron energies are measured. There are several noticeable features that give important information about bonding in the HBr molecule. After the molecule is ionized, the outermost orbital (the orbital with the lowest ionization energy) is split into two distinct energy peaks. These arise from the well understood phenomenon of spin-orbit splitting. The electron has a spin and that electron spin can interact with other electron orbitals or its own orbital an-

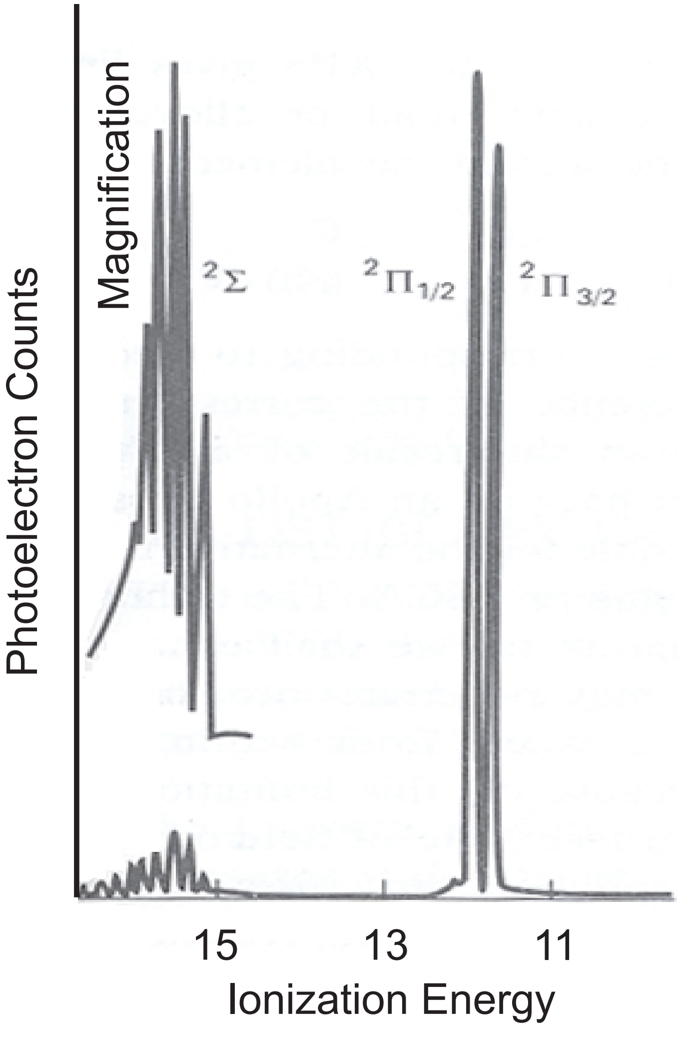

Figure 1.4: The photoelectron spectrum of HBr as a function of ionization energy. The Σ and Π labels are term symbols describing the final state of HBr^+. Spectrum taken from ref. [1]

gular momentum. This interaction causes a splitting of the orbital energies, which results in a doublet peak in the photoelectron spectrum. The series of peaks at a higher ionization energy result from sub-energy levels in the electron orbital, or vibrational energy levels. When a bonding electron is ejected, the H-Br$^+$ molecule can be excited to higher vibrational energy levels, and thus the ejected electrons can lose energy, giving a series of photoelectron peaks.

The field of x-ray photoelectron spectroscopy as a technique has gained momentum in the last several decades with the introduction of synchrotron sources, a light source produced from the acceleration of electrons in a storage ring. Synchrotron sources are capable of generating light from the infrared (μm wavelengths) to the hard x-ray region (Å wavelengths) of the electromagnetic spectrum. An example of the results from an experiment using synchrotron radiation is given in Fig. 1.5 from ref. [2]. In this experiment the 3d core electron energies of Br are measured for different Br-containing compounds. The observed photoelectron spectra (using a photon energy of 96 eV) demonstrate the principle of chemical shifts, where the energies of electronic orbitals of a particular atom shift depending on the nature of the atom on the other side of the chemical bond. For example, the Br atom in the Br-Br bond gives core level energies of $\sim$78.5 and 77.5 eV (again due to spin-orbit splitting), while the Br atom in the C-Br bond in CH_3Br gives core level energies of $\sim$77.3 and 76.3 eV.

1.2 Time-resolved photoelectron spectroscopy

We have seen that photoelectron spectroscopy (both valence and core level) has already given us a wealth of information about bonding in molecules. As the understanding of chemical bonding has progressed, scientists have begun to ask new questions. For instance, how do the electrons in a molecule rearrange when one electron is excited to a higher energy orbital? How do chemical bonds form in time during a chemical reaction? How does a chemical bond break in real time? The experiments presented in this thesis attempt to shed a new light on these fundamental questions.

To address the question of molecules in excited electronic states, a two-photon, two-

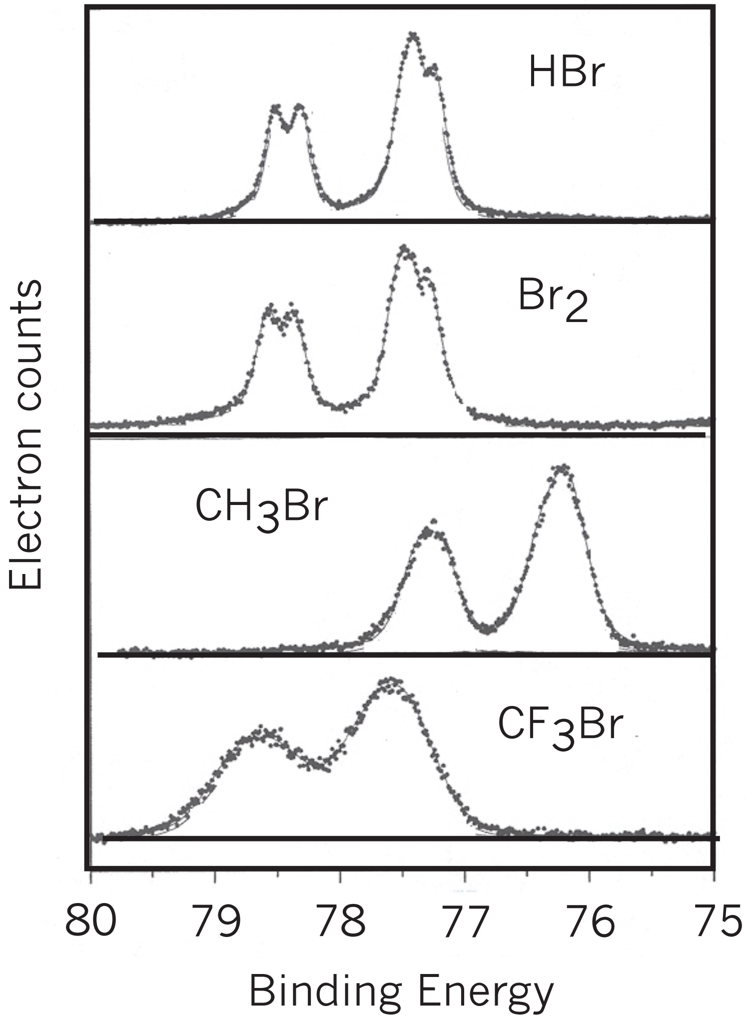

Figure 1.5: Core level photoelectron spectra of HBr, Br_2, CH_3Br and CF_3Br showing the shifting of the 3d Br core levels due to chemical bonding (taken from ref. [2]). Fine structure splitting of the ion states is also present in the spectra.

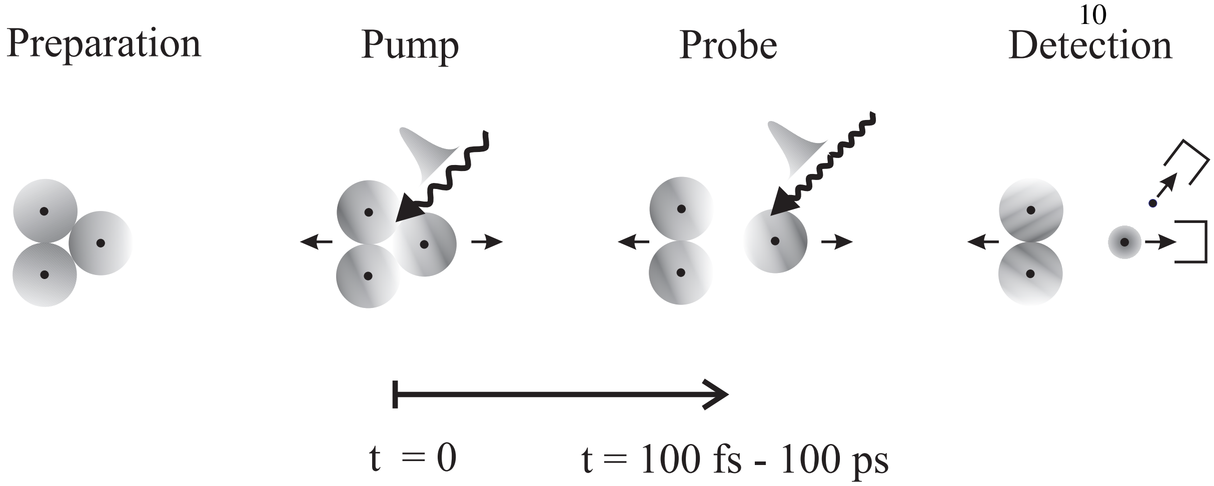

Figure 1.6: A pictorial representation of time-resolved pump-probe photoelectron spectroscopy. The sample molecule is pumped into an electronically excited state with a visible laser pulse. At varying time delays after the pump pulse, a probe laser pulse ionizes the molecule and the photoelectrons are analyzed at each time delay.

color experiment coupled with photoelectron spectroscopy can yield information on the energy redistributions of an excited molecule. A visible photon is used to promote an electron into a higher energy orbital, perturbing the entire electron distribution in the molecule, and then a UV or soft x-ray photon (via photoelectron spectroscopy) is used to measure the energies of the electrons. The related two-photon technique of Raman spectroscopy has yielded vibrational and rotational structure of a large number of molecules.

The processes of bond forming and breaking happen on extremely fast time scales, on the order of 10^{-12} to 10^{-15} seconds. With the invention of ultrafast light sources (lasers that generate very short pulses of light), photoelectron spectroscopy can be extended into the time-resolved realm. Time-resolved photoelectron spectroscopy aims to measure the electron distribution in a molecule as it is going through a transient process, such as dissociation. In general, one ultrafast pulse excites the system under study, and a second ultrafast pulse probes the system at varying time delays by ionizing the molecule and collecting the electrons produced (see Fig. 1.6). Ejected photoelectrons reflect the initial binding energies of the electrons in the molecule, therefore the time-dependent electron energy redistribution can be monitored.

Several research groups have demonstrated the important information gained by time-resolved photoelectron/photoion spectroscopy with visible and UV pulses, including characterization of bound and repulsive electronic states [7, 8, 9], photodissociation and recombination dynamics of negative ions in size selected clusters [10, 11, 12, 13, 14, 15], fast dissociation of Rydberg states [16], and non-adiabatic dynamics of a dimer molecule [17]. An example is shown in Fig. 1.7, where the solvation dynamics of $I_2^-(Ar)_{20}$ clusters were measured on an ultrafast time scale by excitation of the I_2^- chromophore with a 780 nm pulse followed by multi-photon ionization of the excited ion and analysis of the photoelectron energies[3]. The two photoelectron peaks observed are attributed to the spin-orbit states of the I atom ($^2P_{3/2}$ and $^2P_{1/2}$), a result of ionizing the I^- product. The shift in the photoelectron spectrum at early time delays is a reflection of the shifting electron energies as the I_2^- bond is broken. At later times, the photoelectron spectra shift the opposite direction, showing a recombination of the I^- and I fragments due to the surrounding cage of Ar atoms. Thus, it is demonstrated that time-resolved photoelectron spectroscopy is successful at measuring a changing electron distribution in a dynamic system.

1.3 Harmonic generation

In the experiments presented here, we extend the possibilities of time-resolved spectroscopy by combining it with a novel pulsed soft x-ray source. This source originates from a technique called high-order harmonic generation, where an ultrafast Ti:Sapphire laser is focused into a rare gas jet and odd harmonics of the laser are created (from the 3rd to 65th). The properties of the generated light are laser-like, producing coherent, directional, ultrafast light pulses with photon energies from $\sim$5-100 eV. With this range of energies, both valence and core level photoelectron spectroscopy are possible, as will be demonstrated in later chapters. Due to the ultrafast nature of the high harmonic pulses, time-resolved spectroscopy is also possible, where a pulse from the master laser is used as a pump, and the harmonic pulse is used as a probe.

Since the first harmonic spectra were obtained in 1987 [18, 19], an extensive amount of

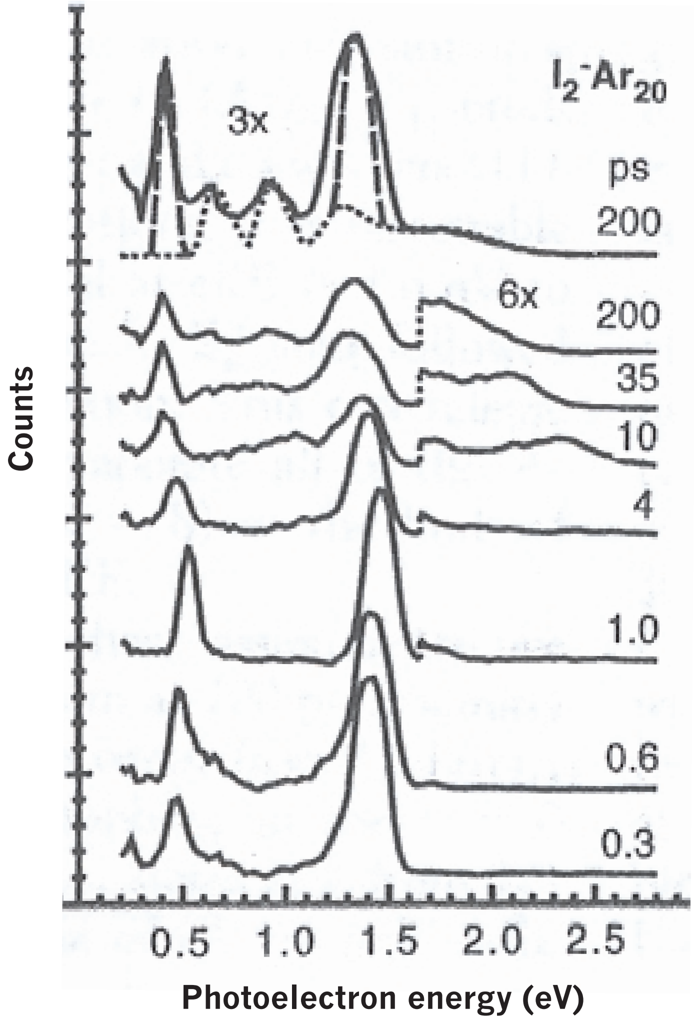

Figure 1.7: An example of a time-resolved photoelectron experiment from ref. [3]. The photoelectron spectrum of $I_2^-(Ar)_{20}$ clusters is shown at various time-delays between the pump and probe pulses.

research has been done to understand the high-order harmonic generation process as well as the properties of the resulting VUV/soft x-ray light. There are many unique characteristics of the harmonic generation process itself, which have been studied through both experiment and theory. It has been found that the extent of harmonic generation depends on several factors, such as the nature of the rare gas medium, several aspects of the focusing conditions and spatial mode of the fundamental laser in the non-linear medium [20], and the length and chirp of the fundamental pulse [21].

To a large extent, theory has successfully modeled these behaviors [22, 23], and the basic process of generating high-order harmonics is well understood. A semi-classical model can qualitatively describe the harmonic generation process, in which the electron tunnels through the barrier formed by the Coulomb potential and the intense laser field. The electron then recombines with the parent atom upon reversal of the optical field, releasing coherent high-order radiation at odd harmonics of the fundamental wavelength [24] (see Fig. 1.8). However, the semi-classical model is unable to predict detailed spectral characteristics; hence, quantum models [25, 26, 27] are required for a more complete description of harmonic generation, and are discussed in more detail in chapter 3.1.

1.4 Coupling the high harmonic source and time-resolved photoelectron spectroscopy

The use of a pulsed high-harmonic soft x-ray source to probe ultrafast chemical dynamics has several advantages. First, probing with a soft x-ray pulse allows the extension of ultrafast photoelectron spectroscopy into the realm of gas phase neutral molecules, without the need for a multi-photon probe step. Multiphoton probe steps, while effective, still have limitations in total probe energy and can cause resonance effects with the host of electronic states in even simple molecules. Though some neutral gas phase molecules have accessible ion states within the ultraviolet region, the choice of target molecules need not be limited by the energy of the probe. While soft x-ray probe wavelengths have the disadvantage of a large background due to ground

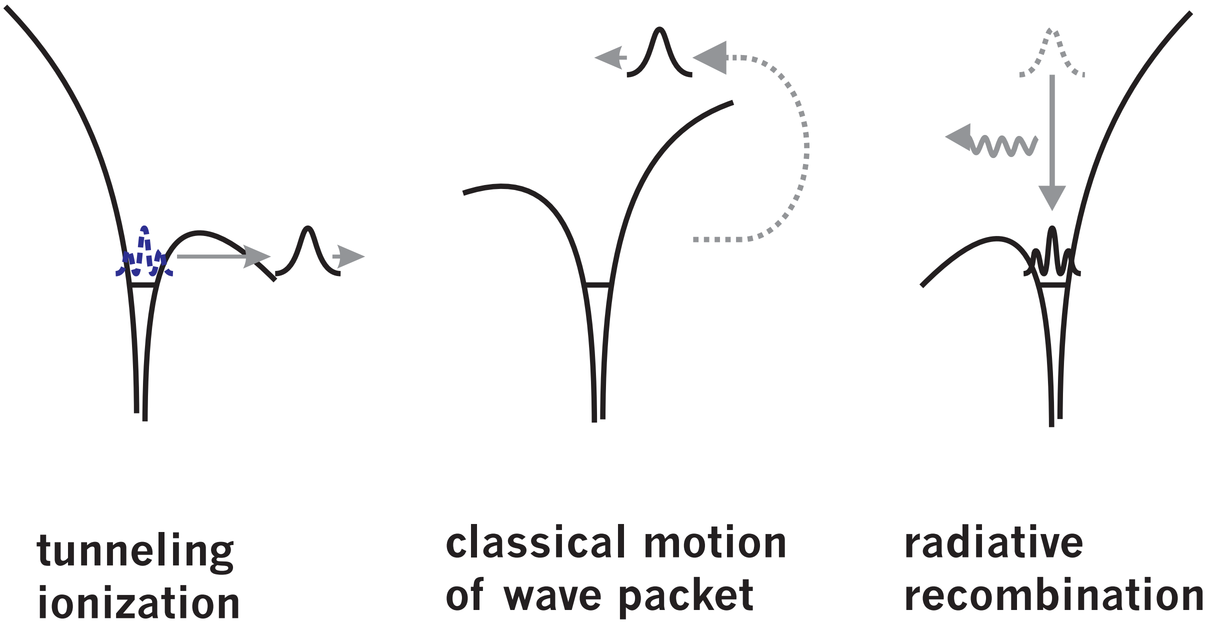

Figure 1.8: A classical picture of high-order harmonic generation with an ultrafast laser. The coulomb potential of the atom is perturbed in the presence of the strong laser field, and tunneling ionization of the electron occurs. The free electron gains energy in the electric field (U_p, pondoromotive potential). As the optical field changes phase, the coulomb potential also oscillates and causes recombination of the electron with the atom, accompanied by the release of a high energy photon.

state absorption from the neutral molecule, careful background subtraction with the use of an optical chopper to sample every other pulse with the pump on/off can overcome this limitation. The large range of photon energies obtained by high-harmonic generation creates a source that is capable of ionizing into both the ground and multiple excited states of the target molecule. This extends the realm of information that can be gained on a particular system, as cross-sections from neutral excited states to various ion electronic states may not only be different, but can also change with time as the neutral excited state wavepacket evolves. Additionally, the versatility of a high-harmonic source allows both valence and core-level time-resolved spectroscopy, giving a complete picture of the energy redistribution within the molecule. While valence level photoelectron spectroscopy yields a wealth of information, how the core level electron energies change upon excitation of a valence electron is not well understood. Core level spectroscopy also gives a site specific probe of atoms in molecules that contain two or more types of atoms, since the core level energies are specific to particular atoms. For example, in a simple molecule like IBr, the core level signature (4d) for the I atom is in the 50 eV region, while Br (3d) levels are in the 70 eV region.

Other groups have demonstrated the application of time-resolved surface photoelectron spectroscopy with soft x-ray light. Picosecond dynamics of electron-phonon interactions on thin organic films was measured by Probst and Haight [28], with a 3.5 eV excite pulse and a 22.4 eV probe pulse, the 11th harmonic of 640 nm. Ultrafast hot electron dynamics on a Pt surface were observed by Siffalovic, et al [29], by focusing a visible and 70 eV high-harmonic pulse on the surface and collecting the photoelectrons from the Pt surface. Lei, et al [30], observed a change in a chemical bond between O_2 deposited on a Pt surface on a sub-picosecond time scale using a visible pump pulse and the 27th harmonic of 800 nm as the probe pulse.

1.5 High-order harmonics and surface photoelectron spectroscopy

Photoelectron spectroscopy has also been used extensively as a probe for surface structure and bonding in condensed phase materials. As part of an internship program, I had the opportunity to work on another instrument designed to use a similar harmonic generation source for surface photoelectron studies. Since the internship was at IBM, improving computer components and the speed with which they are fabricated is high priority. To make a complex computer chip requires 20 layers of microscopic circuitry on a Si wafer. Each layer is patterned onto the Si wafer with a device called a photomask. Fig. 1.9 demonstrates the patterning process, where a light source is incident upon the photomask, a high purity quartz plate with images of the circuit, and the circuit pattern is transfered to the Si wafer.

These photomasks are expensive to make and the ability to precisely repair flaws in the patterns permits a significant reduction in cost and time of chip production. The photomask patterns consist of the deposition of heavy metals on the quartz surface, such as Cr or W. The use of femtosecond ultrafast lasers has already proven to be an effective tool for precise removal of unwanted metal material, such as bridges between small parts of the circuit pattern [31]. The other component in mask repair is the replacement of oblated or chipped metal materials. Deposition and detection of Cr metal without the use of high-temperature ovens, which might further damage the photomask, is the aim of the surface photoelectron spectroscopy experiments. A gaseous metal coordination compound, $Cr(CO)_6$, is thought to be a solution to metal-oven deposition. $Cr(CO)_6$ is deposited on the surface and the surface is subsequently cooled with liquid N_2. The CO ligands are then photolyzed with a UV laser beam in the areas in need of repair, leaving only the Cr metal on the surface. The remaining $Cr(CO)_6$ is released upon heating. To begin to characterize the feasibility of this process, it is necessary to find a way to deposit and detect the Cr on a Si surface. Since ultrafast photoelectron spectroscopy is surface sensitive, a high-harmonic source can be used to detect the core level photoelectron signature of Cr (3p) after it is deposited on the surface. Eventually the dynamics of the deposition of Cr via $Cr(CO)_6$ can also be monitored using time-resolved photoelectron spectroscopy.

In this thesis I describe in detail results obtained using the novel combination of time-resolved photoelectron spectroscopy and a visible/UV pump coupled with a soft x-ray probe. The harmonic generation source and the properties of the incident soft x-ray radiation are out-

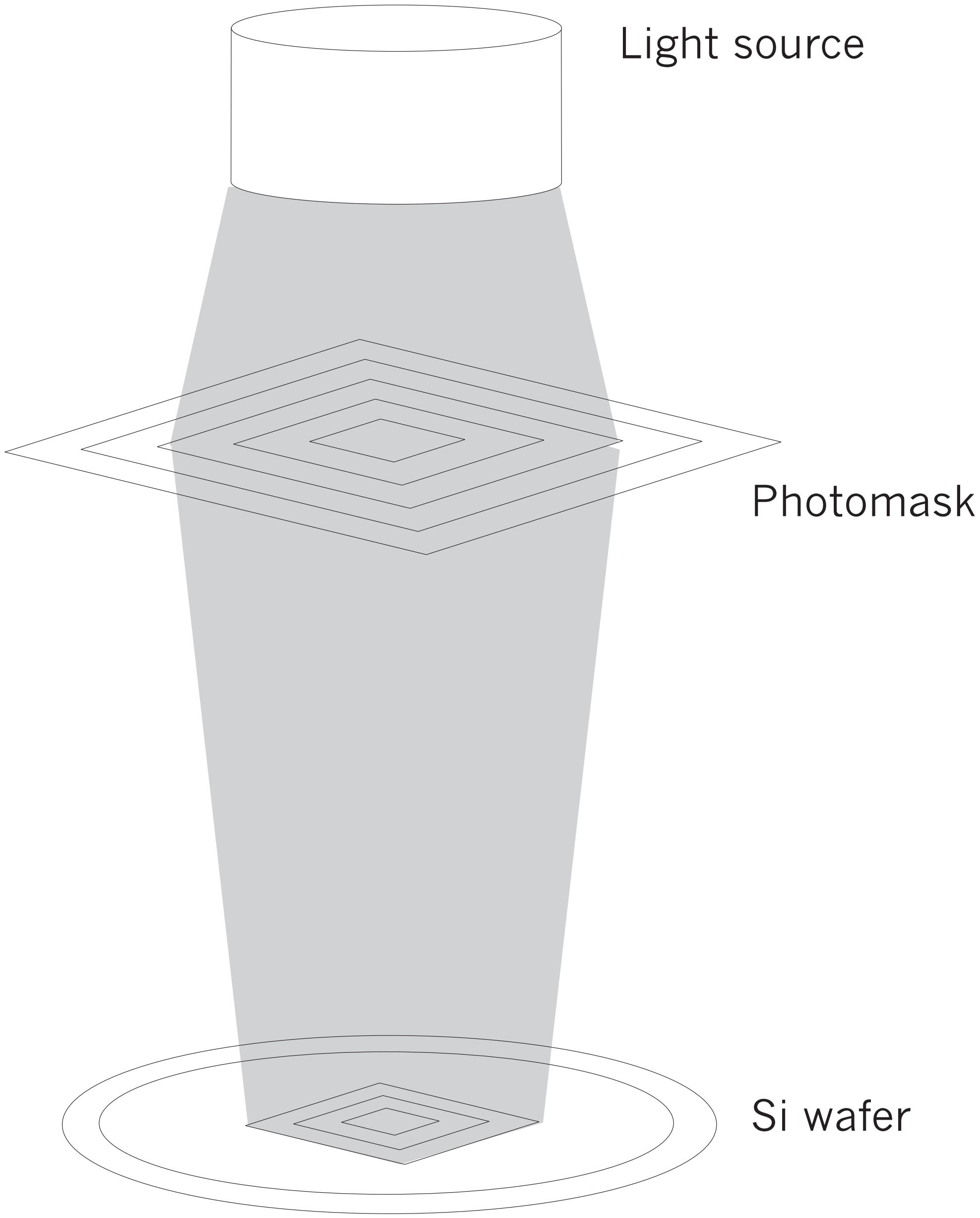

Figure 1.9: The process of imprinting circuitry on a Si wafer using a photomask. The mask is made of high-quality quartz with an image of the circuit deposited on the surface. Photons from a light source are incident on the mask and the pattern is written on the Si wafer.

lined, including a demonstration of tunability and control of the harmonic source, measurements of the energy bandwidths of generated harmonics, and several examples of soft x-ray valence and core level photoelectron spectroscopy of gas phase atoms and molecules, as well as condensed phase samples. Techniques for calibrating the overlap and temporal width of the pump and probe beams are discussed, and above threshold ionization cross-correlation traces between pump and probe beams are shown. The photoelectron spectrum of the bound B state of Br_2 is measured with a 527 nm excitation laser and a 17th harmonic probe. The dynamic photodissociation of Br_2 is observed in a 400 nm pump- 17th harmonic probe set-up, demonstrating the ability to monitor a gas phase reaction in real time.

Chapter 2

The Experimental Apparatus

2.1 Introduction

The instrument was designed for ultrafast UV/visible-pump soft x-ray-probe photoelectron spectroscopy for the purpose of investigating the dissociation of gas phase molecules. This unique approach to studying fundamental gas phase chemical dynamics will open up a new dimension to ultrafast spectroscopy, specifically by the potential to understand both valence and core level energy redistribution in a dissociating molecule. To this end, the instrument described here was built.

A 70 fs, 2.2 mJ Ti:saphhire laser is used to generate high harmonics (up to 100 eV photons) of 800 nm light by focusing $\sim 80\%$ of the beam into a pulsed jet of rare gas (Ne or Ar). These harmonics are frequency separated by a pair of grazing incidence gratings and refocused into the interaction region of a magnetic bottle photoelectron spectrometer. The remaining 20% of the light is frequency doubled or tripled in appropriate non-linear crystals, and subsequently focused and overlapped with the harmonic beam in the interaction region. Samples to be studied are leaked into the chamber through a small nozzle opening. After excitation and ionization of the sample by the pump and probe beams, photoelectrons are collected by a microchannel plate detector located at the end of a 1.4 m flight tube. Here I describe the Ti:Sapphire laser system, the pulsed valve used for harmonic generation, the two-grating set-up used for harmonic selection and compression, and the design and characterization of the magnetic bottle photoelectron spectrometer.

2.2 Laser System

The laser system is a commercial Spectra Physics model, containing a seed Ti:Sapphire oscillator, a pulse stretcher, two stages of amplification and a pulse compressor. A layout of the complete laser system is shown in Fig. 2.1. The seed laser(Tsunmai) is pumped by a diode-pumped cw Nd:VO_4 laser (Millenia) at 532 nm with 4.1 W of average power. The oscillator gives pulses centered at 800 nm with 400 mW average power at a cavity frequency of $\sim$82 MHz. To calibrate the spectral bandwidth (as well as a constant monitoring of mode-locking), 1% of the beam is sent into a fiber optic cable coupled to a small grating monochromator and CCD camera (Ocean Optics Instruments). The signal from the CCD camera is read on an oscilloscope, and the signal is converted to a wavelength scale. To calibrate the oscilloscope signal to a wavelength scale, several known wavelengths (measured independently with a wavemeter) from a cw dye laser were coupled into the fiber optic cable and the position read on the oscilloscope. This calibration curve is shown in Fig. 2.2. The linear relationship between the wavelength and scope position is given by the following equation:

$$\text{Scope Position (time in ms)} = \left(4.37(\pm 0.03) \times 10^{-2}\right) \lambda(nm) - 30.2(\pm 0.2) \tag{2.1}$$

In this way, the bandwidth of the seed laser is measured on a daily basis to be $\sim$16 nm.

The temporal width of the seed pulse is $\sim$57 fs, measured with a commercial autocorrelator. Traces of both the spectral and temporal profile were also measured independently with a commercial FROG (Frequency Resolved Optical Gating) instrument available in the JILA Keck Labs. A good discussion of the FROG technique can be found in Ref. [32]. The results of the FROG are shown in Fig. 2.3, and they agree well with the previously described measurements from the fiber optic and commercial autocorrelator. The dotted line plotted over the temporal trace of the seed pulse in Fig. 2.3 is the phase profile, which is also measured by the FROG instrument. The flat nature of the phase curve indicates that no frequency chirp exists in the pulse. The transform limit (i.e., the shortest pulse possible with a given bandwidth as limited

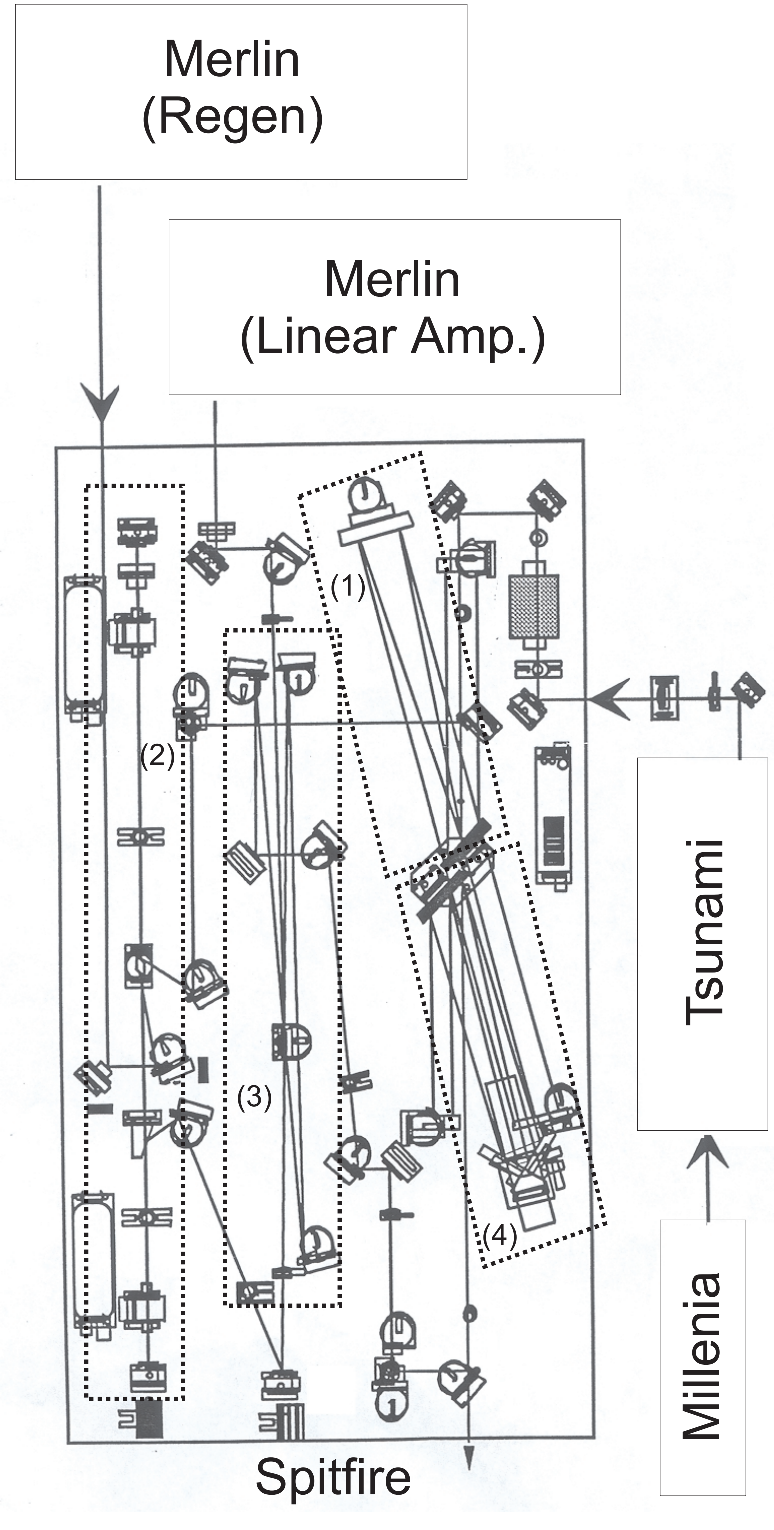

Figure 2.1: A schematic of the Spitfire (two stage Ti:Sapphire amplifier). The seed pulse is first sent through the stretcher (1), and then into the first stage of amplification (Regenerative Amplifier, (2)) where it passes through a Ti:Sapphire crystal. After the maximum gain is achieved from the Regen, the pockels cell rotates the polarization, sending the pulse into the double-pass or Linear Amplifier (3). Finally, the pulse is directed into the compressor (4) and out onto the laser table.

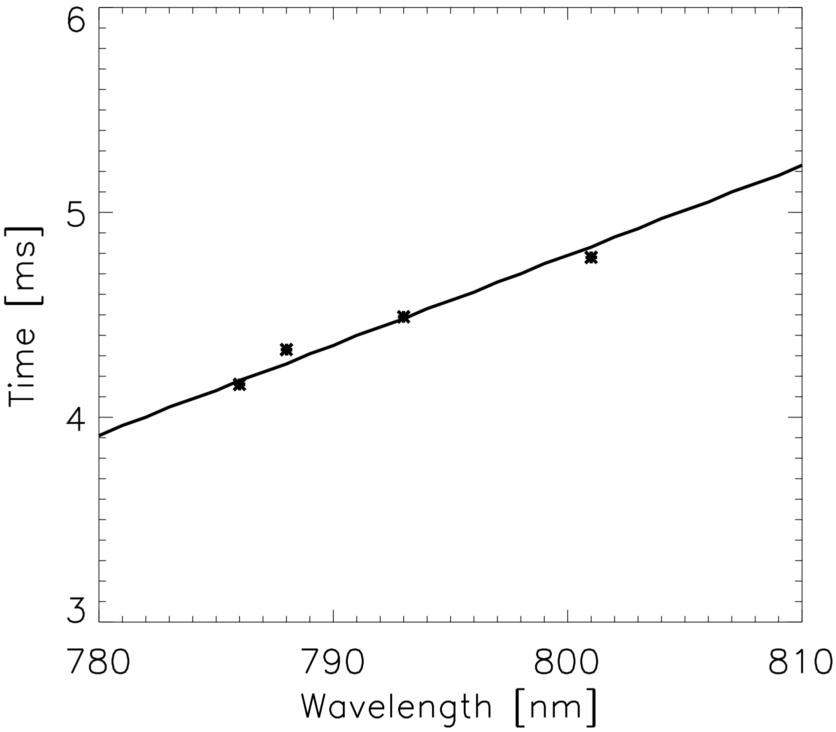

Figure 2.2: A calibration curve for the Ocean Optics fiber-coupled CCD camera that is used to measure the bandwidth of the seed pulse from the Tsunami Ti:Sapphire laser. The points were measured by coupling light from a cw dye laser with known wavelengths into the fiber optic cable and recording the oscilloscope position. A linear fit to the data describes the relationship between wavelength and scope position in ms, allowing for measurement of the Tsunami bandwidth.

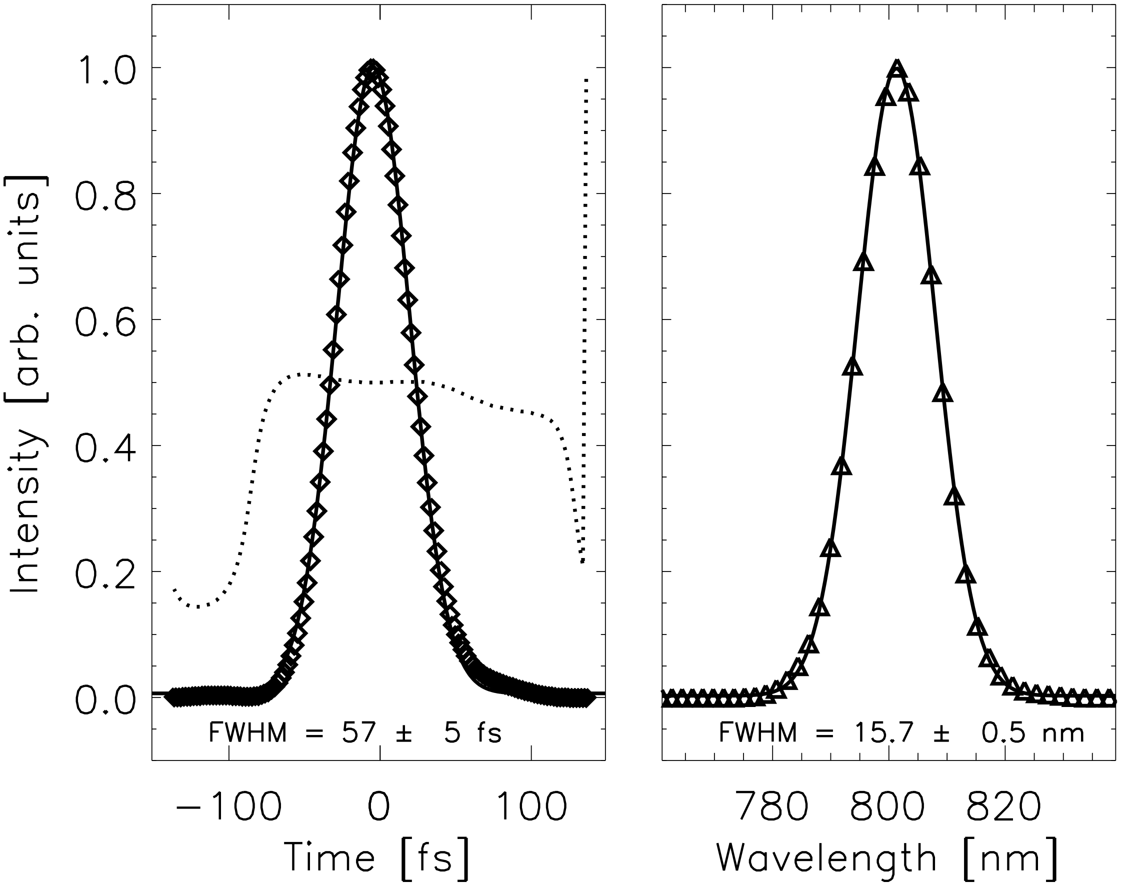

Figure 2.3: The temporal (left) and spectral (right) profile of the seed pulse from the Tsunami Ti:Sapphire laser measured with a commercial FROG instrument available in the JILA Keck labs. The dotted line is a measurement of the phase of the electric field across the pulse, or the amount of frequency chirp in the pulse. A flat phase indicates no frequency chirp across the pulse.

by the uncertainty principle) of an ultrafast Gaussian pulse is given by the simplified equation:

$$\Delta\nu(Hz) \times \Delta t(s) = 0.44. \tag{2.2}$$

For a pulse centered at 800 nm with a 16 nm spectral bandwidth, the limit of the temporal pulse width is calculated to be 59 fs, which is within the experimental error of experimental measurements (both from the commercial autocorrelator and the FROG), showing the transform-limited nature of the seed pulse. Other error could be introduced in such a calculation if the pulse shape is not strictly Gaussian.

The seed pulses are then injected into the amplifier, which first sends the beam through a grating-based stretcher, and then the pulse is directed into a multi-pass regenerative amplifier pumped by a 9 W, 1 kHz, Q-switched Nd:YLF laser. The average power after the first amplification stage is $\sim$1 W. The pulses are further amplified in a double pass linear amplifier, pumped by 12 W of 532 nm light from a Nd:YLF laser identical to the one used in the first stage. The average power before compression is $\sim$3 W and is reduced to 2.2 W after compression due to reflection losses from multiple passes off the compressor grating. The layout of the amplifier is given in Fig. 2.1.

The temporal width of the final output pulse is determined by splitting off 1% of the beam into a home-built single-shot autocorrelator (Fig. 2.4). The autocorrelator divides the beam into two arms, one of which is on a delay stage controlled by a micrometer. The beams are focused with a cylindrical lens into a BBO crystal cut for 2nd harmonic generation. The inset of Fig. 2.4 shows the basic principle of autocorrelation. The horizontal stripe-like focus produced by the cylindrical lens allows the two beams to have a large area of spatial overlap, creating a 400 nm beam that is an image of the overlap of the two pulses. The 400 nm output is then focused onto a CCD camera and the signal is observed on an oscilloscope. When the two pulses overlap in time, the spatial overlap corresponds to their temporal width (related by the speed of light), according to the following equation:

$$\text{pulse width}(fs) = \frac{1}{0.6} \times \left(\frac{2 \times \Delta x_{mic}(\mu m)}{\Delta t_{scope}(ms)}\right) \times \left(\frac{FWHM_{trace}(ms)}{0.3\,\mu m/fs}\right), \tag{2.3}$$

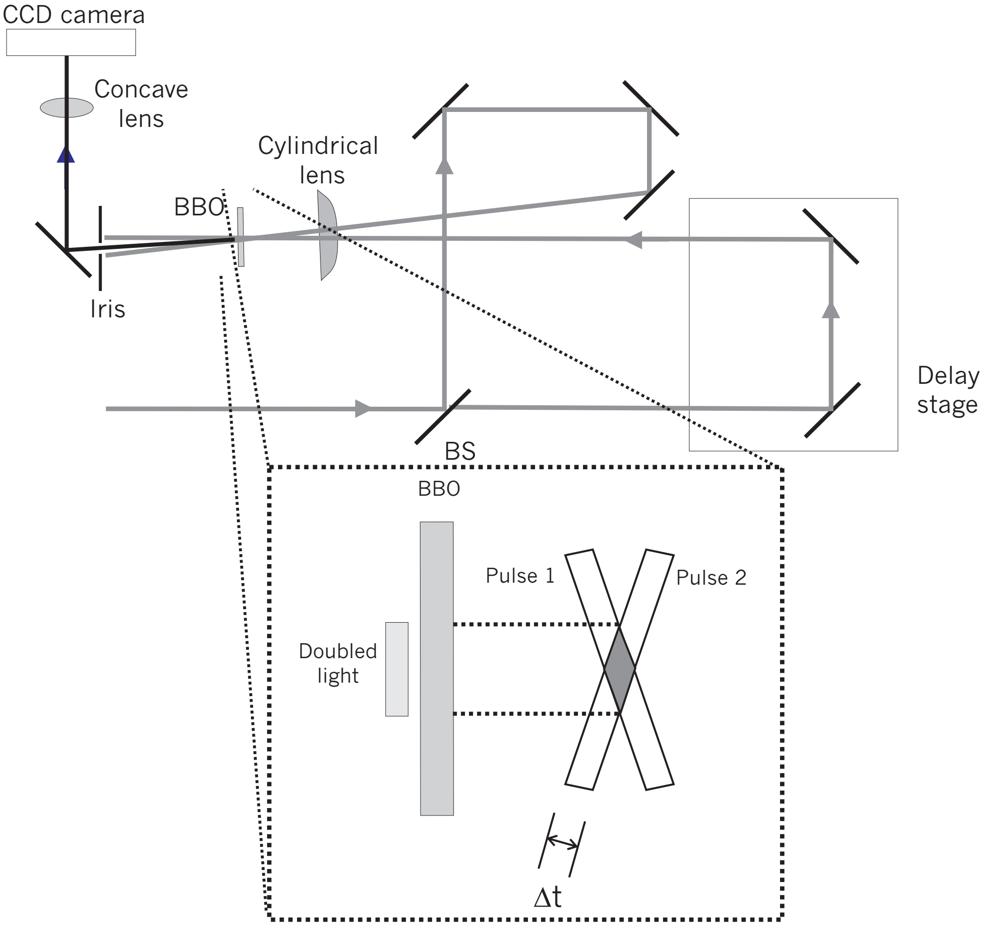

Figure 2.4: A schematic of the single-shot home-built autocorrelator used for determination of the temporal pulse width of the amplified output pulse.

where $\Delta x_{mic}(\mu m)/\Delta t_{scope}(ms)$ is the calibration factor relating the scale on the scope to the micron stage of the mobile arm of the autocorrelator, FWHM$_{trace}$ is the full width at half maximum of the autocorrelation trace, 0.3 μm/fs is the speed of light and 0.6 is a factor accounting for the shape of the autocorrelation trace, assumed to be Gaussian.

The laser system yields a consistent pulse width of 70-80 fs, assuming a Gaussian pulse profile, while the spectral bandwidth is preserved through the amplification process. The final output of the amplified pulse was also measured by the FROG instrument mentioned above. These results are shown in Fig. 2.5. The temporal profile of the amplified pulse has a FWHM of 69± 3 fs, while the spectral profile still has a FWHM of 16 nm. The dotted line indicating the phase or chirp of the pulse is slightly curved compared to the one for the initial seed pulse, indicating a slight frequency chirp in the amplified pulse. This is to be expected in the amplification process, as a small amount of linear frequency chirp results from the mirrors, lenses and Ti:Sapphire crystals encountered by the pulse which cannot be fully compensated for by the compressor grating.

2.3 Optical layout

The layout of the pump and probe optical beams is shown in Fig. 2.6. The 9 mm diameter output beam of the Spitfire travels first through a 80/20 beamsplitter, and the transmitted 80% beam continues through a half-wave plate (labeled 'P'), which is changed between 0° and 45° to match the polarization of the pump beam. After passing through a stepper-motor controlled delay stage, the beam is focused into the vacuum chamber with a 40 cm lens to an $\sim$100 μm spot 1 mm above the output of the pulsed valve where harmonics of the laser are created. The harmonics as well as the residual 800 nm beam travel through a baffle with a 1 mm opening. The combined beam then hits the first concave grating (4 m radius of curvature, 1200 lines/mm) which can be rotated to select a single harmonic. The harmonic and residual 800 nm beam diverge from the focus in the pulsed valve chamber and appear as a $\sim$4 mm spot on the grating. When the grating is rotated to 0th order, the 800 nm beam can be seen through a small win-

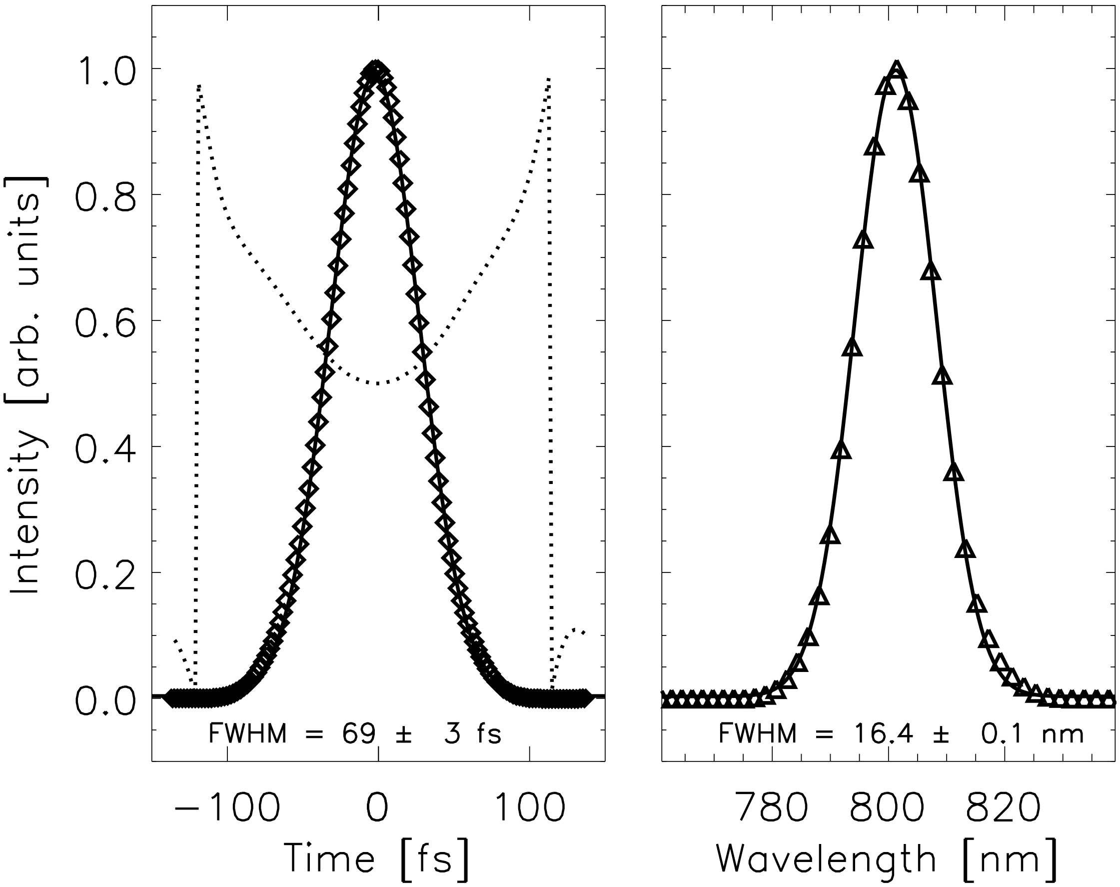

Figure 2.5: The temporal (left) and spectral (right) profile of the pulse from the amplified Ti:Sapphire laser measured with a commercial FROG instrument available in the JILA Keck labs. The slight curvature in the dotted line (representing the phase of the electric field) indicates a slight frequency chirp from the amplification process as compared to the seed pulse.

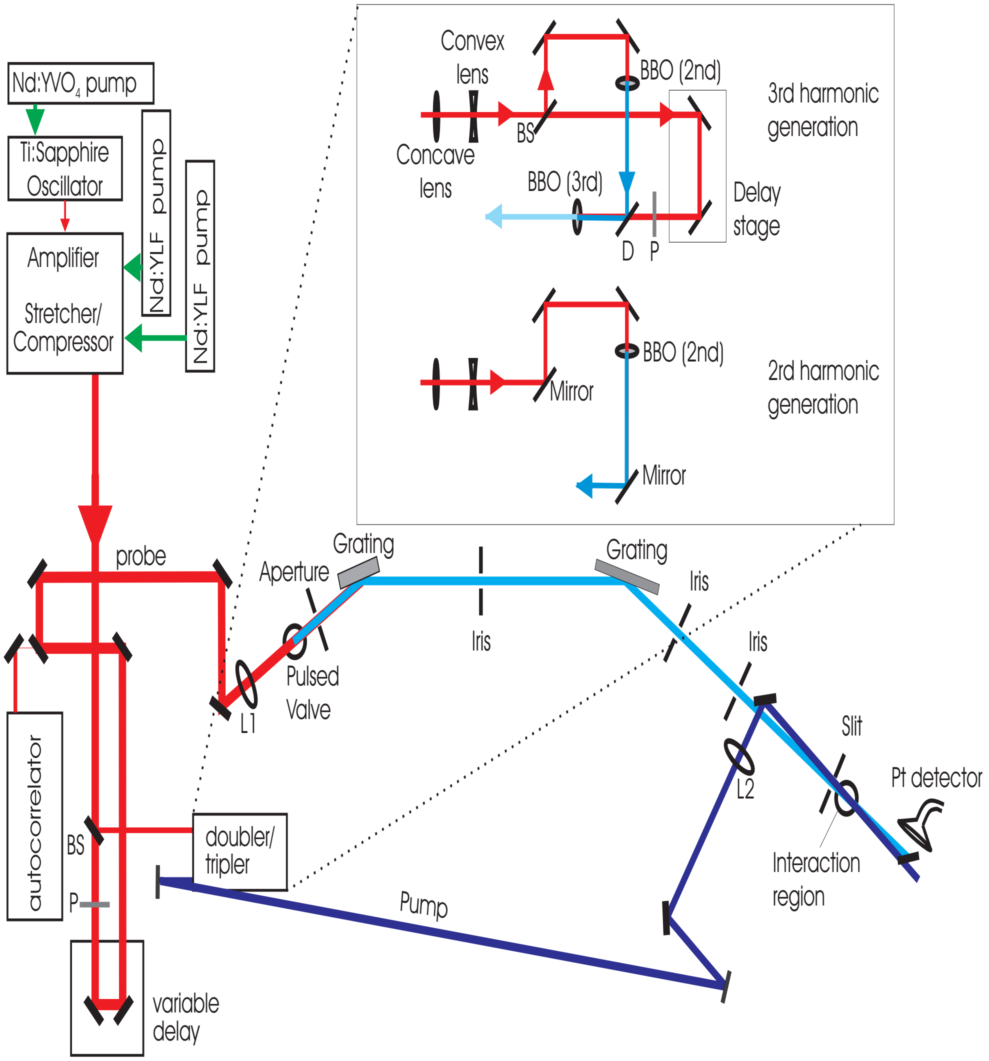

Figure 2.6: The optical layout of the pump and probe beams. The output beam is split into pump and probe beams at the 80/20 beamsplitter (BS). The 20% reflected beam is sent into the doubler/tripler to frequency upconvert the pulse to 400 nm or 266 nm. The pump beam then passes through a 70 cm lens (L2) into the chamber, and after reflection from the mirror inside the vacuum chamber, comes to a focus at the slit. The 400 nm beam comes to an $\sim$1 mm focal spot in the interaction region, with a power density of 2 $\times 10^{11}$ W/cm^2. The transmitted beam (80%) passes through a half-wave plate, a delay stage and is then focused with a 40 cm lens (L1) into the pulsed gas jet and the selected harmonic is directed and focused into the interaction region. The 17th harmonic, as an example, is focused to a 250 μm spot with an estimated power density of 1×10^5 W/cm^2 in the interaction region. **Inset:** First the pump beam is sent through a telescope to reduce the beam size. For 2nd harmonic generation, the 800 nm beam is sent through a BBO crystal. For 3rd harmonic generation, the 800 nm beam is split into 2 beams where one arm is doubled in a BBO crystal and combined again with the second 800 nm arm in a BBO crystal cut for tripling to produce 266 nm output.

dow on an iris (iris 1 in Fig. 2.6) located inside the chamber and used for alignment purposes. The second grating (a toroidal surface with two different radii of curvature) is located ~80 cm from the first. Here the beam has diverged significantly from the tight focus in the pulsed valve chamber and the toroidal surface of the grating serves to refocus the harmonic beam as well as correct for spherical aberrations induced by using spherical optics at grazing incidence angles. While the first spherical grating causes a slight decrease in the angle of divergence of the beam, the toroidal grating is the most effective refocusing optic. It has a radius of curvature of 2 m in the plane defined by the optical beam, and a 40 mm radius of curvature in the plane perpendicular to the optical beam propagation direction. Ray tracing simulations predict an optimal 100-300 μm diameter focus (wavelength dependent) of the harmonic beam in the interaction region when both gratings are rotated to inside first order diffraction. An example of the results of the ray tracing program is given in Fig. 2.7, where the focal plane of the 21st harmonic is shown at the slit. Fig. 2.6. The harmonic beam then passes through two more irises before focusing at the slit, which is located ~5 cm before the interaction region. The beam then passes directly in front of the sample nozzle and hits a piece of Pt metal, and the resulting photoelectrons produced via the photoelectric effect are directed onto an electron multiplier to detect the presence of the harmonics.

The other 20% of the beam is sent through a home-built doubler/tripler to create pump wavelengths of 400 nm or 266 nm. The layout of the doubler/tripler is shown in the inset of Figure 2.6. For doubling, 20% of the original beam (2.3 mJ) is first sent through a telescope to reduce the beam size. It then passes through a 0.1 mm thick BBO crystal cut for 2nd harmonic generation. The average power of the 400 nm beam is 140 μJ, an ~40% conversion efficiency. For tripling, the beam is first sent through a 50/50 beamsplitter and one arm is doubled as described above. The other arm is sent through a delay stage controlled by a micrometer, followed by a half-wave plate set at 45°. The two beams (800 and 400 nm) are then overlapped spatially and temporally in a wavemixing crystal (also BBO, cut for tripiling) with a dichroic mirror to produce 266 nm light. The residual 400 and 800 nm beams are separated out by using optics

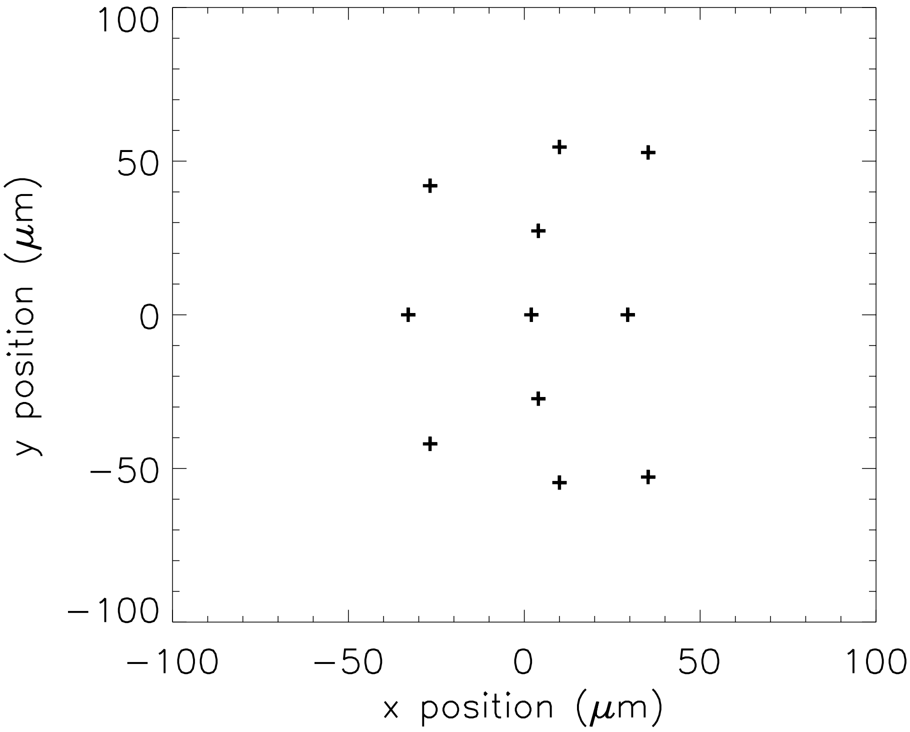

Figure 2.7: A ray tracing simulation of the 21st harmonic beam on the slit (right before the interaction region). The beam has a diameter of ~100 μm in both directions. There is some ellipticity of the beam due to the toroidal grating surface. The toroidal grating was designed for a certain beam geometry, and the actual input beam deviates from that slightly with the addition of the spherical grating. The points represent 11 rays starting from different positions in the initial collimated beam.

coated for 266 nm to direct the tripled beam into the chamber. Approximately 60 μJ of 266 nm is produced, a 15% conversion efficiency from the original 800 nm beam energy. The pump beam can be switched from 266 nm to 400 nm by taking out the tripling crystal and replacing the 50/50 beamsplitter with a mirror.

The distance of the pump beam is matched roughly to the path length of the harmonic beam inside the vacuum chamber, so that the range of the delay stage encompasses the perfect distance. The pump beam is focused with a $\sim$70 cm lens mounted on an x-y-z micrometer stage before entering the chamber after the second grating. The beam reflects off a mirror located less than 1 cm above the harmonic beam and then passes through the top of the slit, which is wider than the center of the slit where the probe beam passes through, allowing for some range of motion to overlap the pump beam with the probe beam (see Fig. 2.6). The two beams overlap in the interaction region at an $\sim 1^\circ$ angle. The pump beam hits a window on the back of the chamber where a mask is placed to aid in alignment.

The most important alignment tool is a mobile aperture ($\sim$1 mm hole in a small piece of copper metal) mounted on a translating vacuum feedthrough. This aperture is placed in the interaction region where the pump and probe beams cross. The typical alignment procedure is as follows: Align the fundamental 800 nm beam (with both gratings rotated to 0th order) and the pump beam (400 or 266 nm) through all the apertures, irises, and the slit located inside and outside of the vacuum chamber (which can be vented during this first step for initial alignment). Here it is important to ensure the 800 nm beam is as centered as possible on both gratings by using an infrared viewer. When both beams are going through the aperture located in the interaction region, keep the mobile aperture in place. After the chamber is under vacuum, remove the aperture and attempt to find the 800 nm + 400 nm multiphoton ionization signal in xenon (described in chapter 6). The x-y-z stage holding the lens that focuses the pump beam can be moved in small steps (10 μm) to optimize the pump-probe signal. Next, turn on the pulsed valve to create harmonics and re-position the mobile aperture into the interaction region. Rotate the toroidal grating to the desired harmonic while leaving the spherical grating at 0th order. Read the signal on the Pt-electron multiplier showing the presence of the harmonic. If the signal increases when the mobile aperture is removed from the interaction region, the grating is not properly aligned. To improve the alignment, move the aperture back into place and iteratively translate and rotate the grating to increase the harmonic signal on the detector. Then attempt to find the harmonic + 400 nm (or 266 nm) above threshold ionization signal in xenon (also described in chapter 6). Again, the x-y-z stage can be adjusted to optimize pump-probe signals. Once this is accomplished, rotate the spherical grating away from the 0th order to the inside 1st order until the harmonic signal reappears. Follow the same procedure for proper alignment of the spherical grating.

2.4 Vacuum Chamber

Figure 2.8 is a diagram of the vacuum chamber containing the pulsed valve, gratings and photoelectron spectrometer. The stainless steel vacuum chamber is pumped by 5 turbo pumps, the location of which are designated by the outgoing arrows in Fig. 2.8. Three of the five turbo pumps have a pumping speed of $\sim$500 L/s (spherical and toroidal grating chamber and interaction chamber), while the flight tube turbo has a pumping speed of $\sim$400 L/s, and the chamber with the pump beam mirror has a pumping speed of $\sim$300 L/s. The pumping speeds were chosen by estimating the volume of the chamber and the gas flow rate (for both the pulsed valve and the sample) and calculating the pumping speed needed to keep the chambers below $\sim 10^{-6}$ Torr. The two pumps located on the interaction chamber and flight tube are chemically resistant, and clean N_2 is flowed at a steady rate over the bearings of all turbo pumps to prevent damage by corrosive gases. Typical base vacuum pressures are 5×10^{-8} to 2×10^{-7} Torr.

2.4.1 Pulsed Valve

The pulsed valve consists of a stainless steel housing containing a gas inlet and a piezo crystal (Fig. 2.9(a)). The piezo crystal is attached to a center plunger with an o-ring seal. When a voltage is applied, the puckering of the crystal causes the plunger to open and allow gas

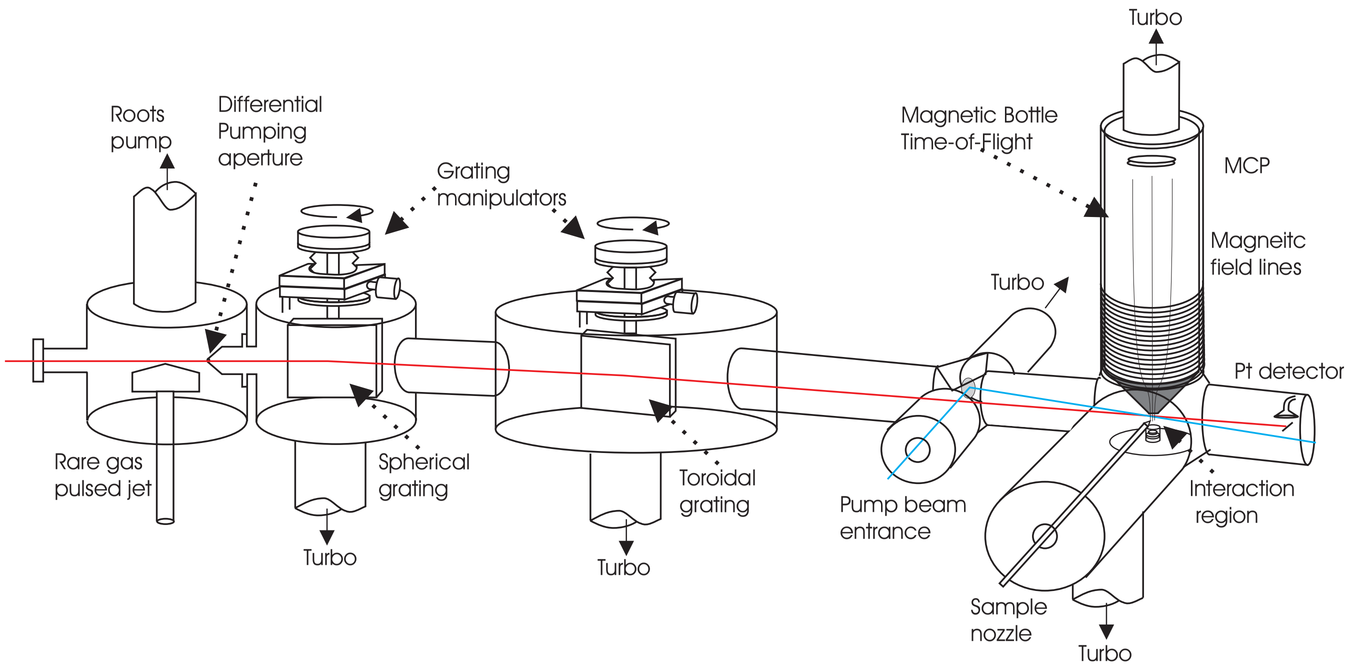

Figure 2.8: A detailed schematic of the vacuum chamber, including the pulsed valve chamber, the two grating chambers, and the magnetic bottle photoelectron spectrometer. The probe laser beam is focused into the pulsed valve gas jet at (A) where the harmonics are created. The harmonic of choice diffracts in 1st order off of the first spherical grating at (B), then again off the second toroidal grating at (C), and enters the interaction region at (D) where it intersects the gaseous sample (E). Ejected photoelectrons are collected in the magnetic bottle time of flight (F) and detected with the MCP detector (G). The pump beam enters the chamber at (H) and reflects off of a mirror located slightly above the harmonic beam and crosses the harmonic beam at a small angle in the interaction region.

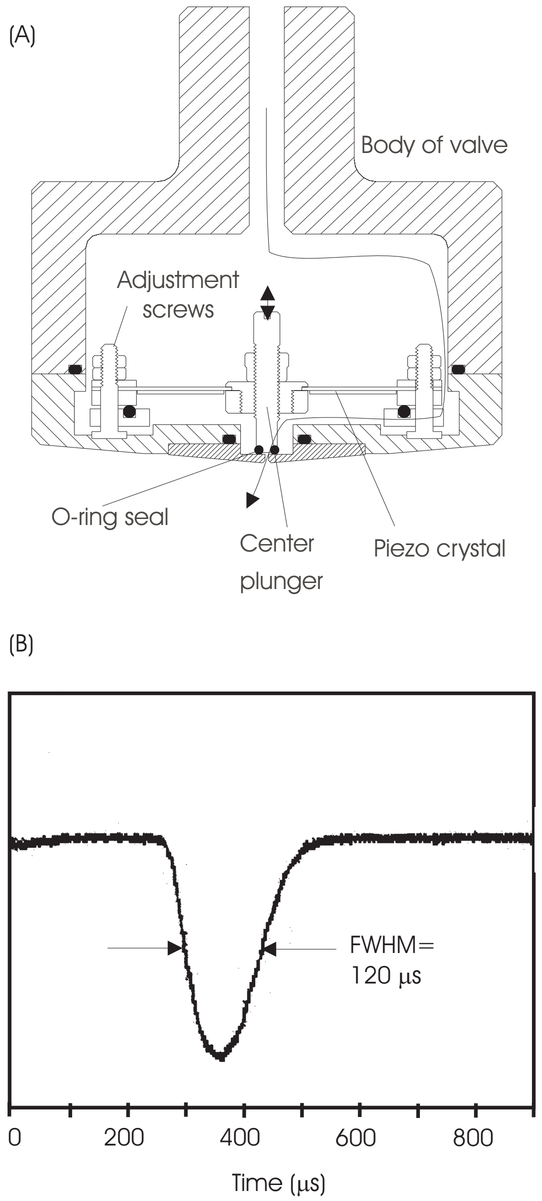

Figure 2.9: (a) A sketch of the pulsed gas jet used for harmonic generation. Gas is released out the 1 mm aperture when the center plunger is lifted by the puckering of the piezo crystal when a voltage is applied. Four adjustment screws hold the piezo crystal in place and the tension tunes the output profile of the gas pulse at a 1 kHz repetition rate. (b) A profile of the output gas pulse measured with a hearing aid microphone. The width of the pulse can be adjusted by the width of the driving voltage pulse.

through the 1 mm diameter opening. A power supply produces -300 V dc output, which first passes through a high voltage pulse generator to generate 120 μs pulses from 0 to -300 V. These pulses are sent to the piezo crystal, causing it to pulse at a 1 kHz repetition rate to match the Ti:Sapphire laser. A voltage pulse with shorter duration was found to damage the piezo crystal. The voltage pulser is triggered by an output from the laser which is delayed by the correct amount to overlap the peak of the gas pulse with the laser pulse. Careful adjustment of the tension of the center plunger as well as four outer screws (labeled in Fig. 2.9(a)) is necessary to obtain a clean 1 kHz gas pulse (for example, if one of the screws is too tight, a double bounce can occur, giving two gas peaks per laser pulse). Upon initial installation, the profile of the gas pulse was measured with a hearing aid microphone placed $\sim$5 cm above the valve opening and the signal amplified 100× before being read on an oscilloscope (Fig. 2.9(b)). The width as well as the height of the gas pulse can be adjusted by adjusting the width and voltage of the driving voltage pulse (always a negative driving pulse). The pulse height (indicating the amount of gas per pulse) is set at the value for maximum harmonic generation while the width of the pulse is set to 100-200 μs. An increase in the pulse height increases the background chamber pressure linearly (15 mTorr per -30 V step for Ne, 1 mTorr per -30 V step for Ar). The chamber pressure increase with increasing pulse width is negligible.

The backing pressure of the gas to the pulsed valve differs depending on whether argon or neon is used as the non-linear media. For low order harmonics (7th-25th), argon is used at a backing pressure of 10 psi. For higher harmonics (27th-65th), neon is used with a backing pressure of 40 psi. The backing pressure is adjusted for maximum harmonic signal on the Pt detector. An example of this is shown in Fig. 2.10, where the signal on the Pt-electron multiplier from the 9th harmonic was recorded as a function of argon backing pressure. The pulsed valve chamber rises to 50 mTorr for argon and 150 mTorr for neon. The pulsed valve chamber is pumped by an 800 L/s roots pump. An estimated $1\ \times 10^{18}$ atoms/cm^3 are in the volume of the laser focus. The 1 mm baffle opening allows the harmonic beam to pass through to the first grating chamber while serving as a differential pumping aperture. The pressure of the first

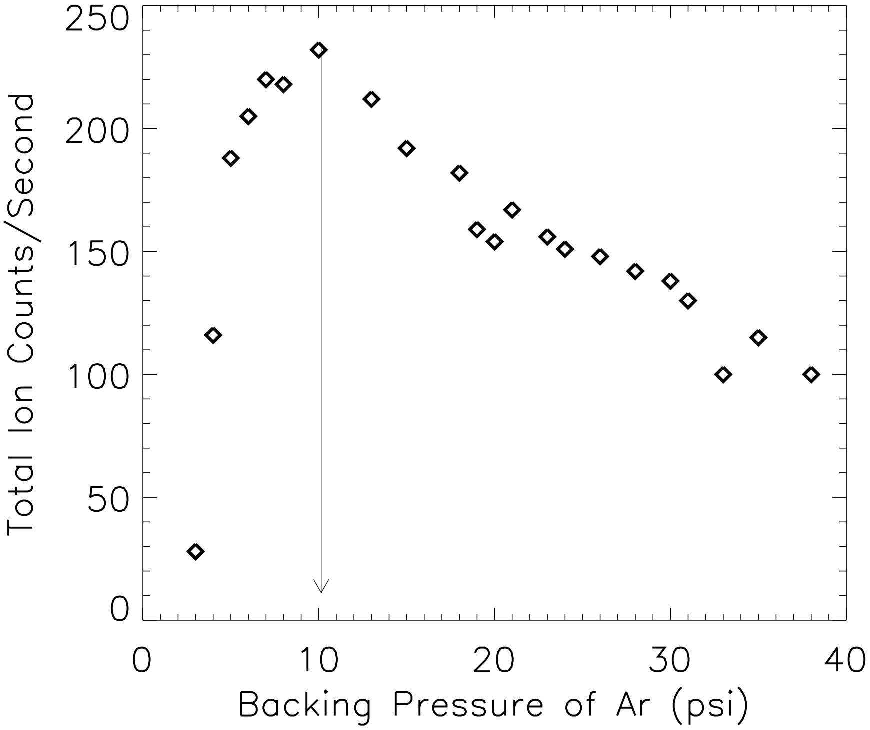

Figure 2.10: An example of adjusting the backing pressure to the pulsed valve and recording the intensity of the harmonic signal from the Pt-electron multiplier using argon as the backing gas for the 9th harmonic of 800 nm. The maximum harmonic signal occurs at $\sim$10 psi argon as shown by the arrow. The decrease in harmonic signal when going to higher backing pressures is due to ionization of the non-linear gas medium with higher gas densities.

grating chamber is 1 $\times 10^{-6}$ Torr while the pulsed valve is running.

2.4.2 Two-grating separation and compression

The separation of the individual harmonics is achieved with a pair of grazing-incidence gratings. Only one grating is required for wavelength separation, but the second is needed to temporally re-compress the pulses. The first spherical grating (1200 lines/mm, 4 m radius of curvature, gold coated) is blazed for normal incidence but used at grazing incidence (165° total angle) for the soft x-ray beam. The 4 m radius of curvature translates to $\sim$1 m input and output arm lengths due to the Rowland circle [33]. The grating is mounted on a 1” thick rod attached to a rotation stage coupled to a baffle, allowing rotation and translation of the grating in vacuum. The baffle is mounted with the top flange attached to a micron translation stage along with set screws to adjust the tilt in all directions. All of these degrees of freedom are necessary for proper alignment of the harmonic beam. The 800 nm beam reflects at 0th order while the grating is turned to the inside first order to pass the selected harmonic. The second grating (300 lines/mm) has a toroidal shape and gold-coated surface with two radii of curvature (2 m in the plane defined by the optical beam, and 40 mm in the plane perpendicular to that one). The severe toroidal surface compensates for the spherical aberrations of using spherical optics at grazing incidence, and the harmonic beam is focused to a spot instead of a vertical line. The toroidal grating was designed specifically for grazing incidence diffraction of the soft x-ray harmonic beam, and it is thus blazed at a shallow (2°) angle for better diffraction efficiency. This grating is also on a similar translation/rotation stage as described above. The temporal compression of the ultrafast pulses using these two gratings is described in chapter 6, and the geometry of gratings in this instrument compared to a compression due to the wavelength spreading of an ultrafast pulse is described (as a theoretical possibility) in ref. [34].

2.4.3 Photoelectron Spectrometer

The photoelectron spectrometer consists of the sample nozzle, the Pt metal plus electron multiplier used to detect the presence of the harmonic beam, a magnetic bottle time-of-flight (TOF) tube, and a microchannel plate detector (MCP) for detection of the photoelectrons. For gaseous samples, a needle valve is used to control the effusive flow of the sample into the chamber through a 1 mm nozzle opening located very close to the overlap of the laser beams. For liquid samples, such as Br_2, the vapor pressure over the liquid is sufficient to leak the gaseous sample into the chamber. Solid samples are heated with heating tape to produce the vapor pressures needed in the interaction region. The interaction chamber rises to a background pressure of no more than 5×10^{-5} Torr during experiments, giving an average sample density of 1.6 $\times 10^{12}$ molecules/cm^3 or slightly greater directly after the nozzle opening. The electron multiplier at the end of the x-ray beam, described earlier, is positively biased to detect electrons coming off a Pt surface caused by the photoelectric effect with the soft x-ray beam. A cone-shaped differential pumping aperture (illustrated in Figure 2.8) is located directly above the interaction region. The differential pumping allows the interaction chamber to rise to higher pressures while holding the flight tube at an acceptable pressure for the MCP detector (approx. 5×10^{-6} Torr), and it also reduces electron-molecule collision effects in the flight tube, which can lead to a large, broad background signal on the MCP detector.

The microchannel plate detector is a double stack of thin (2 mm) plates containing tiny channels. When electrons ejected from the sample enter the channels (coated with a dielectric material), they multiply by bouncing off the inside of these channels, creating a cascade of electrons. The front of the MCP is biased at a high positive voltage (+2.4 to 2.8 kV), while the anode (or electron collecter) is biased at +100 to 300 V. This drives the electron multiplication towards the anode, where the current is measured with respect to ground. If a large number of electrons ($\sim 1 \times 10^5$ counts/laser shot) hit the detector within an amount of time shorter than the detector response time ($\leq$ 5 ns), the detector channels become 'saturated', and the signal out is not a true indication of the original number of electrons.

The magnetic bottle configuration ensures good collection efficiency of the ejected photoelectrons [35]. Strong (≈ 7.4 kGauss) SmCo permanent magnets are placed 1 cm below the interaction region, while a 3 A dc current is passed through a coil wrapped around the entire flight tube. This configuration creates a high magnetic field in the interaction region and a low magnetic field in the flight tube, as illustrated by the field lines in Fig. 2.8. The permanent magnet position for highest collection efficiency is $\sim$2 cm below the interaction region, however, the electron energy resolution decreases as the gap is increased. The photoelectron signal decreases approximately 50% by a 5 cm gap. The trajectories of the electrons in the top 2π sphere of the interaction region are thus turned upward by the high magnetic field and a larger percentage of photoelectrons are collected by the MCP than in the case of a normal time-of-flight.

2.4.3.1 Resolution of the Magnetic Bottle Spectrometer

To calibrate the resolution of the magnetic bottle time-of-flight spectrometer, a narrow bandwidth laser source was used to photoionize NO gas. The 9th harmonic of 1064 nm (118 nm) was created by focusing the standard 355 nm output (3rd harmonic) of a commercial Nd:YAG laser into a static cell of Xe gas at 3 Torr. The 118 nm output (10.5 eV) was used to ionize NO slightly above threshold (9.26 eV, [36]), giving low energy photoelectron peaks (below 2 eV). This photoelectron spectrum is shown in Fig. 2.11. Vibrational resolution is achieved in the NO^+ X state, and photoelectrons resulting from v=0, 1, and 2 are observed. In this way the inherent resolution of the system was determined independently of the ultrafast laser. The bandwidth of the NO photoelectron peaks using the nanosecond laser is limited by the resolution of the spectrometer and not by the narrow bandwidth of the laser. The best reported magnetic bottle resolution is $\Delta E_{pe}/E_{pe} \approx 1\%$ [35], when the magnetic fields are meticulously adjusted. The $\Delta E_{pe}/E_{pe}$ of our NO data was found to be $\approx 5\%$, giving the basic resolution for the magnetic bottle spectrometer.

The resolution of the magnetic bottle is best at low photoelectron energies (below 3 eV),

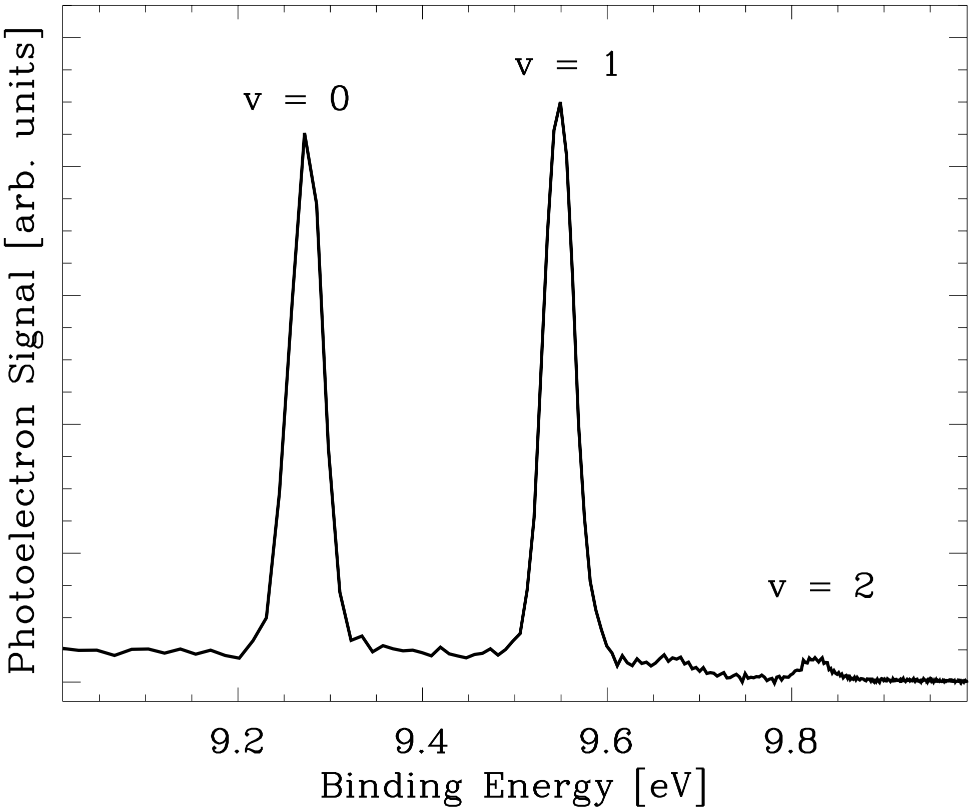

Figure 2.11: Photoelectron spectrum of NO gas taken with the 9th harmonic of a long pulse, narrowband Nd:YAG laser, $E_{h\nu}$=10.496 eV. Here the inherent resolution of the magnetic bottle spectrometer is seen in the peak widths. The vibrational progression of the NO^+ ground state gives rise to the three peaks separated by $\approx$0.28 eV.

where the resolution is limited by the bandwidth of the laser. At intermediate photoelectron energies, the resolution is limited by the magnetic bottle ($\Delta E/E = 5\%$). At very high photoelectron energies, the data collection process determines the limit of resolution, since the time-of-flight signal is recorded in 5 ns bins. To achieve the best resolution for a particular photoelectron energy range, the flight tube itself (a 6 ” diameter tube, $\sim$ 1.2 m long) is electrically isolated from the rest of the interaction chamber and can be held at a voltage which is adjustable from 0-40 V. In this way, the flight tube voltage can be adjusted to discriminate against low energy electrons and bring the desired part of the spectrum into the region of best resolution.

After photoelectrons are collected by the MCP detector, signal pulses are sent through a 100x preamplifier before being read by a multi channel scalar (MCS). The MCS is triggered by a photodiode signal originating from the 800 nm laser beam before it enters the pulsed valve chamber. The signal pulses are then collected in 5 ns bins after the arrival of the trigger pulse. Typical photoelectron spectra record 250,000 total electron counts in 30,000 laser pulses (1 data collection pass per laser pulse), with peak heights ranging from 500-10,000 counts. With a laser repetition rate of 1 kHz, a 30,000 pass scan takes about 30 seconds. For pump-probe spectra, where transient signals are much smaller, 100,000 pass scans are typically used.

2.4.3.2 Energy Calibration

For proper energy scaling of the raw time-of-flight data, the magnetic bottle spectrometer must be calibrated using known photon energies and samples with well known binding energies. To accomplish this, the harmonics from the Ti:Sapphire laser are used to produce photoionization spectra. When light from the zeroth order diffraction of the grating, the specular reflection, is incident upon a sample of helium gas, the photoelectron spectrum in Fig. 2.12 is obtained. The first harmonic to ionize He is the 17th (26.35 eV), and each higher harmonic ionizes He as well, giving a harmonic spectrum. Up to the 37th harmonic the spectrum is clearly resolved.

By compiling the He data for the various harmonics, a calibration of the magnetic bottle

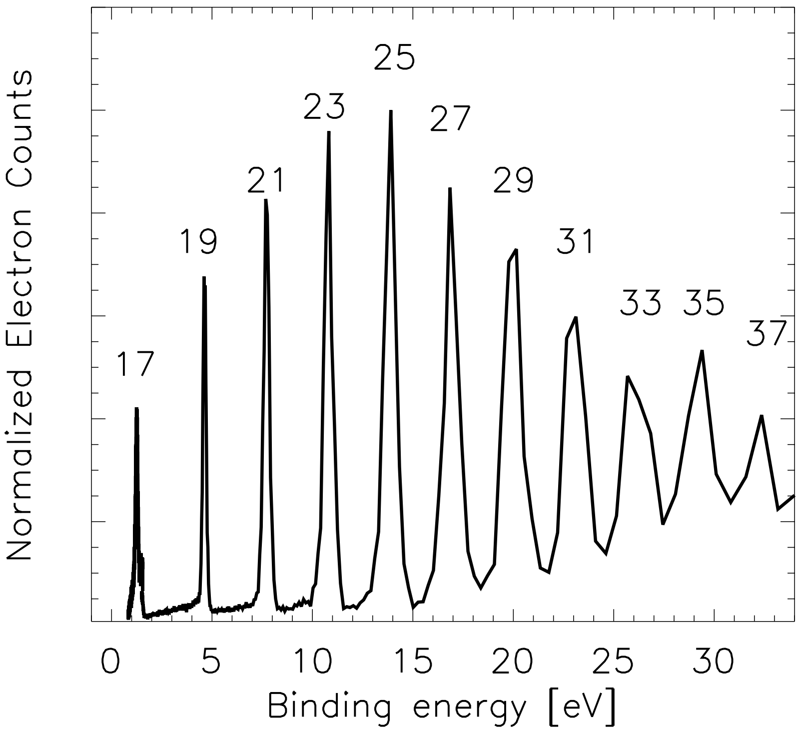

Figure 2.12: Photoelectron spectrum due to all harmonics simultaneously incident on a sample of He gas. The first harmonic energetic enough to ionize He is the 17th ($E_{h\nu}$=26.4 eV). Each subsequent harmonic is seen as another main ionization peak at increasingly higher energies. Note the decrease in resolution for the higher electron kinetic energies.

spectrometer over the full kinetic energy range is made. A plot of the known photoelectron energy, $E_{pe} = E_{h\nu} - I_p$ (where E_{pe} is photoelectron energy, $E_{h\nu}$ is the photon energy, and I_p is the ionization potential of the sample), vs. time-of-flight of the electrons, t, is expected to follow the equation:

$$E_{pe} = \frac{1}{2} m_e \left(\frac{d}{t}\right)^2, \tag{2.4}$$

where m_e is the mass of the electron, and d is the distance traveled by the electron. To fit the acquired data to a proper t^{-2} curve, both a time (t_0) and energy offset (E_0)are introduced, and equation 7.1 becomes:

$$E_{pe} = E_0 + \frac{1}{2} m_e \left(\frac{d}{(t + t_0)}\right)^2. \tag{2.5}$$

A plot of the photoelectron energies (determined by the known energy of the harmonic minus the ionization energy of Helium) vs. the measured time of flight is given in Fig. 2.13. By allowing d, t_0, and E_0 from equation 7.2 to be variables, a nearly perfect fit to the data is obtained (shown as the dotted line in Fig. 2.13, giving values of $d = 1.38(\pm 0.04)$ m, $t_0 = -0.03(\pm 0.01)\mu$s, and $E_0 = 0.16(\pm 0.15)$ eV). The flight tube distance agrees well with the physical dimensions of the system, and the t_0 offset is due to the inherent delay between the arrival of the laser pulse at the interaction region and the trigger signal derived from a photodiode. The energy offset is nearly zero within the uncertainty. However, with the creation of a large amount of ions so close to metal surfaces (i.e., the nozzle, the permanent magnet housing, and the cone), it is possible that small contact potentials exist in the interaction region. The surfaces close to the interaction region are therefore coated with a fine graphite layer to minimize charging effects.

Low energy (below 3 eV) photoelectron peaks are even more sensitive to this type of calibration, and a separate fit for low energy peaks was accomplished using the spectrum in Fig. 2.11. Again, a fit to equation 7.2 using the known energy of the laser and binding energies of the v=0, 1, and 2 levels of NO, along with the recorded time of flight positions of these peaks was accomplished. Here, the flight tube distance remained fixed and only the two parameters, t_0 and E_0, were varied to obtain the dotted line curve in Fig. 2.14. The values of t_0 and E_0 for

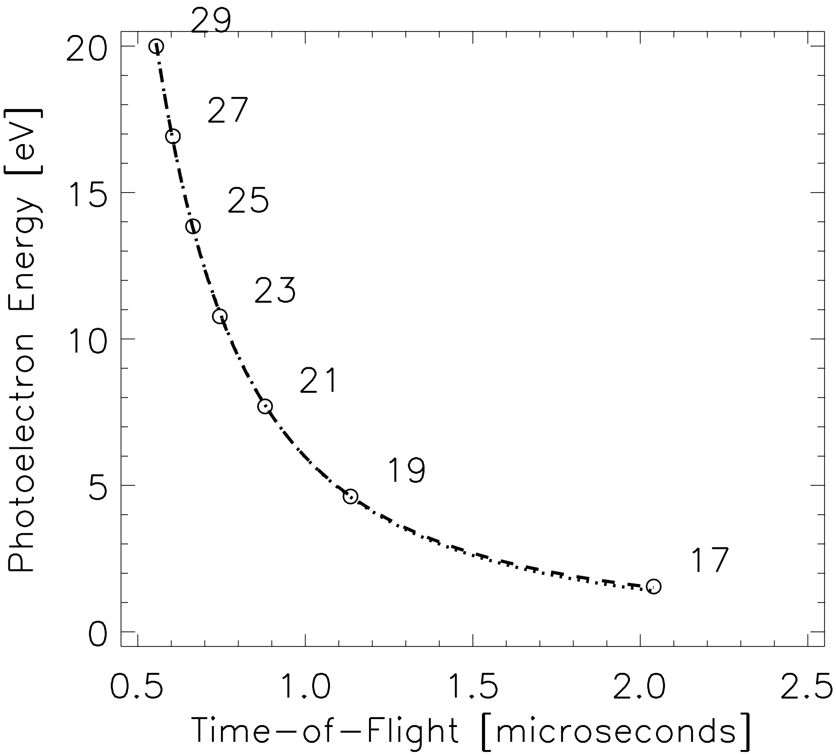

Figure 2.13: An energy calibration curve taken from the time of flight peak positions of Fig. 2.12 and the known photoelectron energies. The dotted line is a fit to the data from equation 7.1.

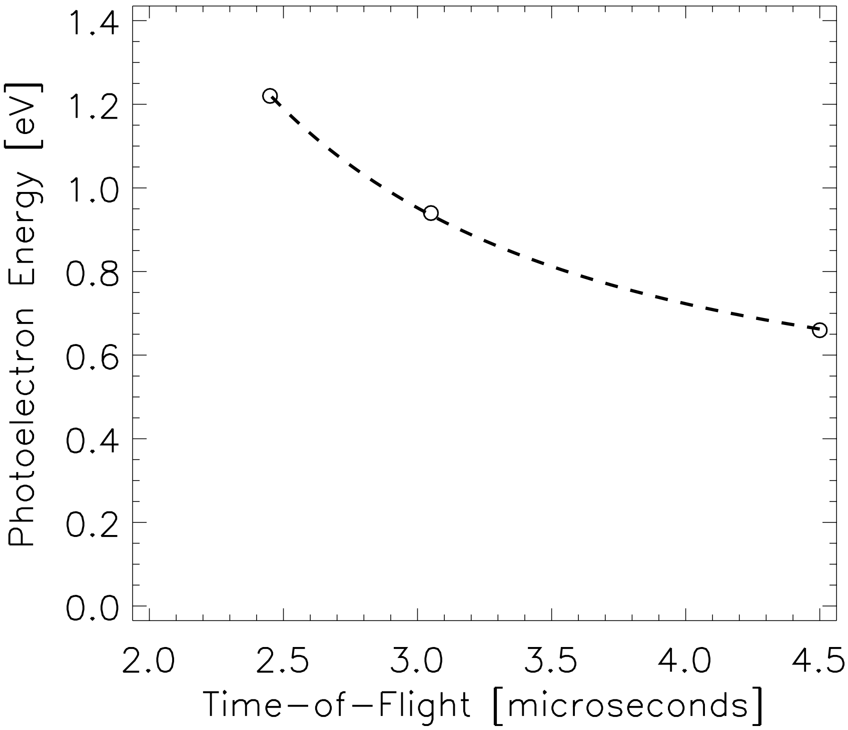

Figure 2.14: An energy calibration curve for very low photoelectron energy peaks (below 2 eV) taken from the time of flight peak positions of Fig. 2.11 and the known photoelectron energies. The dotted line is a fit to the data from equation 7.2.

this data fit were found to be -0.12 $(\pm 0.01)\mu$s and 0.44($\pm$0.01), respectively. The value of t_0 agrees quite well, while the E_0 is slightly larger. Low photoelectron peaks are expected to be more sensitive to small energy offsets and thus the fit to the NO data could give a somewhat different value of E_0. In general, the first calibration scale is used when reporting photoelectron spectra, unless very low energy photoelectron (or long time-of-flight) peaks exist.

2.5 An instrument for ultrafast photoelectron spectroscopy of solids: IBM T.J. Watson Research Center

As a recipient of an Optical Science and Engineering Program (OSEP) fellowship at CU, I had the opportunity to do an internship for 3 months with Dr. Richard Haight at the IBM T.J. Watson Research Center in Yorktown Heights, NY. While there, I was able to work with a very similar harmonic generation source, but coupled to a low-pressure vacuum chamber built for photoelectron spectroscopic studies of surfaces. An outline of the experimental apparatus is shown in Fig. 2.15, adapted from ref. [4]. Briefly, a commercial Ti:Sapphire laser system (Coherent) consists of a 532 nm Nd:YAG pump laser, a Ti:Sapphire oscillator, a pulse stretcher and regenerative amplifier (pumped by a 527 nm Nd:YLF laser), and a pulse compressor. My goal for the internship was to first build a double pass amplifier similar to the one in the Spitfire (see Fig. 2.1) for the purpose of creating higher order harmonics for surface core-level photoelectron spectroscopy and eventually time-resolved studies. The optimal double-pass amplifier configuration is shown in Fig. 2.15. The beam is taken out of the stretcher and focused into a 2nd Ti:Sapphire crystal which is pumped by the 527 nm output of another Nd:YLF laser. The beam is refocused for a second pass through the Ti:Sapphire crystal, and the final output sent into the compressor. Without the double pass amplifier, the final output of the laser system was $\sim$400 mW average power at a 500 Hz repetition rate with a pulse width of 75 fs. With the addition of the double pass amplifier, the final output power is increased to 750 mW, or 1.5 mJ/pulse at 500 Hz.

The final output beam is split with a 90/10 beamsplitter (BS) and the 90% transmitted

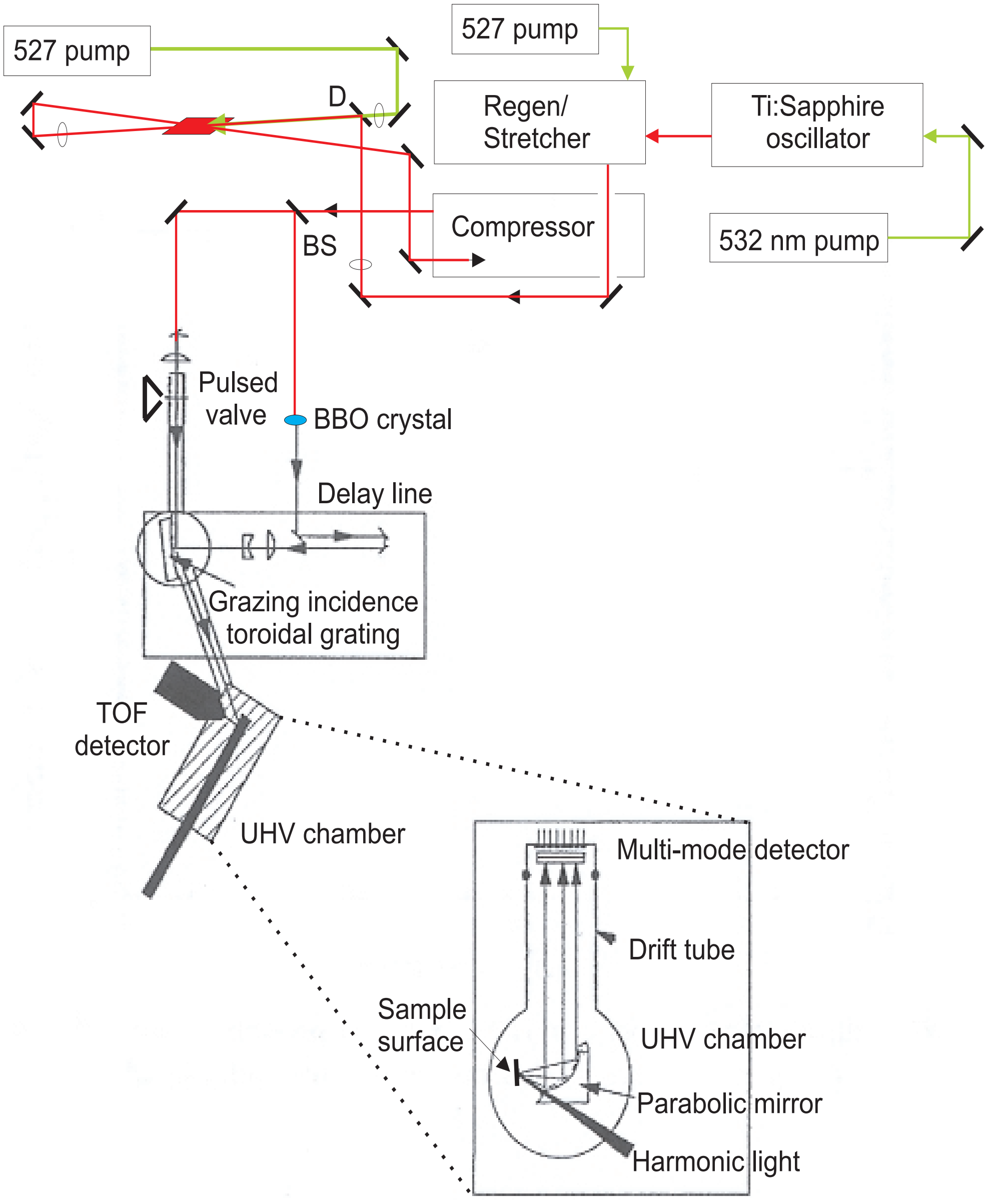

Figure 2.15: A schematic of the instrumental apparatus used during my internship at IBM T.J. Watson Research Center, adapted from ref. [4]. The doubly amplified Ti:Sapphire laser is focused with a 40 cm lens into a pulsed jet of neon gas where high-order harmonics are created. The harmonics are frequency separated with a grazing incidence toroidal grating and focused onto the sample surface after passing through a small pinhole before the UHV chamber. Photoelectrons created from the surface are directed into a TOF drift tube with a parabolic mirror and detected with a multi-mode detector.

beam is focused into a commercial pulsed gas jet (with Ar or Ne) operating at 500 Hz. Before the addition of the linear double-pass amplifier, only harmonics up to the 31st were available, and with the new 1.5 mJ output, up to the 65th harmonic was observed in Ne. The generated harmonics are frequency separated with a grazing-incidence toroidal grating, and focused onto a solid sample after passing through a 2 mm pinhole before the UHV chamber. The UHV chamber consists of a sample manipulator, with the ability to change samples and deposit thin films in vacuum, a voltage-biased parabolic mirror to direct and collimate the generated photoelectrons, a drift tube for energy separation of the electrons and a multi-mode detector. The sample was biased at -6 V to repel electrons towards the mirror, and the voltage on the parabolic mirror was held at a positive voltage of $\sim$30 V to guide the ejected photoelectrons into the drift tube.

Three types of samples were used. First, a cleaved GaAs (111) surface was used to calibrate the harmonic energies by ejecting core electrons from surface Ga and As atoms. Second, a Si sample was used as the substrate and Cr metal was deposited on this surface for measurement of the Cr core levels. Cr metal was heated in a crucible in vacuum and the amount of material deposited on the Si surface was measured using a quartz crystal microbalance. Lastly, I attempted to deposit $Cr(CO)_6$, a gaseous compound, on a Si surface. The Si surface is cooled with liquid N_2 to cause the molecules to condense on the surface. Then, when the sample is brought to room temperature, the Cr should remain on the surface and the CO molecules will evaporate off. This last scheme for depositing Cr is much cleaner and better for use in photomask repair, as is discussed in chapter 1.

Chapter 3

Characterization of high-order harmonics and static photoelectron spectroscopy

3.1 Introduction

The ability to reproduce and understand known photoelectron spectra with the harmonics is an essential step leading to their use for time-resolved spectroscopy. Energy bandwidths of the harmonics, issues of chirp, data collection efficiency and harmonic intensity are all parameters determined by photoelectron spectroscopy and provide necessary knowledge for interpretation of time-resolved spectra. This instrument was designed not as a high-resolution photoelectron spectrometer, nor to push the limits of high-harmonic generation, but instead to combine the ultrafast nature and energy range of the harmonics with photoelectron spectroscopy of moderate resolution to give a novel apparatus for the study of ultrafast chemical dynamics.

3.2 Harmonic generation

Before attempting pump-probe experiments, it is necessary to characterize the harmonic generation source and the photoelectron spectrometer. Two harmonic spectra are shown in Figure 3.1, the first with neon as the non-linear media and the second with argon. These spectra were taken by irradiating the Pt electron multiplier with the harmonic beam while rotating the toroidal grating (the concave grating remaining at 0th order) at a constant speed using a stepper-motor device coupled to the rotation stage on which the grating is mounted. The angle of reflection of the grating is related to the photon energy by the well known grating equation:

$$E_{h\nu} = \frac{mhc}{d(sin\Theta_i + sin\Theta_d)}, \tag{3.1}$$

where m is the integer number describing the order of diffraction (in this case $m = 1$), d is the groove spacing, and Θ_i and Θ_d are the incidence and diffraction angles, respectively (with respect to the grating normal) [33]. In this way the rotation of the grating can be calibrated to the specific harmonic energy. The harmonic spectrum generated in neon shows a sharp rise in intensity for the first few harmonics followed by a plateau over a large range of harmonics, and again a sharp cutoff in the harmonic intensity around 100 eV. The harmonic intensities depend on a number of factors, including the intensity of the laser focus, the pulse duration of the driving laser, and the position of the focus in the gas jet. For both spectra in Fig. 3.1, the laser intensity at the focus (5 $\times 10^{14}$ W/cm^2) and the pulse duration (80 fs) are the same, and the focus is slightly before the jet (2-3 mm). For the higher harmonics ($\sim$41st and above), moving the focus towards the center of the jet gives a slightly better harmonic signal. The harmonic plateau and sharp cutoff in intensity in Fig. 3.1 are common features seen in harmonic generation and discussed in detail in the literature [37, 21, 38, 25]. The smaller peaks between the lower harmonics in the neon spectrum are 2nd order diffraction of the higher harmonics from the grating.

The relative intensities between the two spectra in Fig. 3.1 are derived from the electron multiplier voltage, which was +2.7 kV for the argon spectrum and +3.3 kV for the neon spectrum. Taking the gain vs. voltage of the detector into account (i.e., the difference in gain with voltage applied to the detector) , and assuming the cross-section for photoionization of the Pt metal to be nearly constant over the range of harmonics, generating harmonics in argon yields on average an order of magnitude greater photon flux than when using neon. From cross sections of Xe 5p photoelectron lines [36] the photon flux of the 17th harmonic (26.5 eV photon energy) is calculated to be 3×10^6 photons/pulse. From known cross-sections of He satellite lines [39] (leaving the He$^+$ in an excited state), the photon flux of the 61st harmonic (95 eV

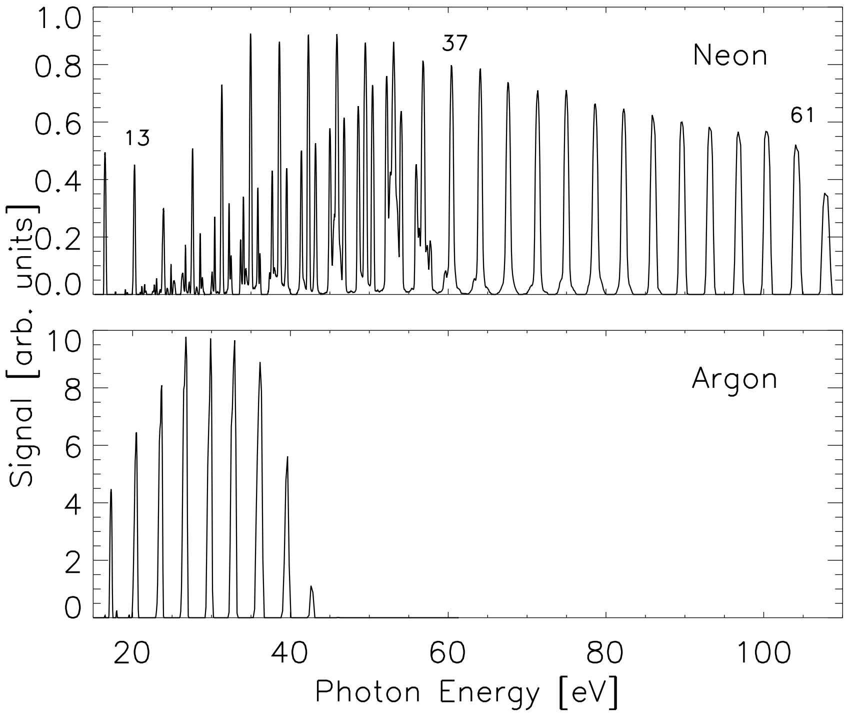

Figure 3.1: A spectrum of the harmonics of 800 nm created in a gas jet of neon (top) and argon (bottom). Detection of the harmonics was accomplished by irradiating a piece of Pt metal with the harmonic beam and detecting the ejected photoelectrons with an electron multiplier as the grating was rotated at a steady rate. Small shoulders on the low order peaks in the top panel are the 2nd order diffraction of the high harmonics reflected from the grating. Harmonics 13-65 are detected in neon, and 11-27 are detected in argon. Detector settings were 3.3 kV across the electron multiplier for the neon spectrum and 2.7 kV for the argon spectrum.

photon energy) is estimated to be 1×10^5 photons/pulse. Therefore, argon is more efficient for producing the lower harmonics, which are used for valence-level photoelectron spectroscopy, and neon, while less efficient, yields higher harmonics with energies well suited to core-level photoelectron spectroscopy.

Although this instrument was not built for the study of the inherent process of high harmonic generation, some initial diagnostic studies were done. In the early literature, the most prominent systematic experiments for harmonic generation sources are to measure the intensity of the generated light as a function of driving laser intensity and as a function of the position of the laser focus in the gas jet [37, 40, 41, 42, 43]. With a series of neutral density filters, the intensity of the driving laser beam was varied while monitoring the intensity of the 9th harmonic with the Pt-electron multiplier, giving the plot in Fig. 3.2. The harmonic intensity seems to follow one positive slope from 5-7 $\times10^{14}$ W/cm^2, and a shallower positive slope from 7-10 $\times10^{14}$ W/cm^2. Lisio, et al [40] report a similar effect which they attribute to the the harmonics first being generated in a perturbative regime (dotted line in Fig. 3.2), until saturation (or ionization) of the non-linear medium (argon) occurs due to the increasing laser intensity, causing a different trend (dashed line). While the numerical value of the slope for the two trends may not agree with ref. [40], experimental differences could account for these discrepancies.

Using the output intensity of the 9th harmonic of 800 nm (read by the Pt-electron multiplier), the position of the laser focus was translated between ~3 cm before the center of the jet to ~2 cm after the gas jet, which is shown in Fig. 3.3. The structured nature of the signal as a function of position in the gas jet is related to phase-matching of the generated harmonic with respect to the driving laser pulse [44], or more specifically the coherence length (L$_{coh}$) over which the harmonic light is generated. Salieres, et al [43] shows a strong dependence of the spatial characteristics of generated harmonics as a function of the position of the focus in the gas jet. While we were not able to measure the spatial profile of the harmonics, a change in the spatial profile of the harmonic light could account for changes in the harmonic intensity on

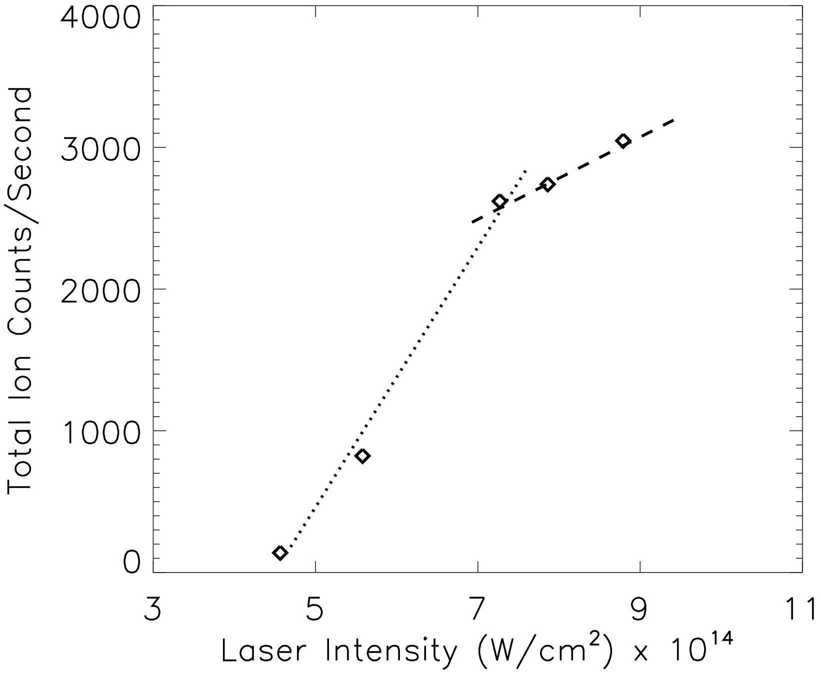

Figure 3.2: The intensity of the 9th harmonic generated in Ar as a function of the driving laser intensity in W/cm^2. Two trends are observed, attributed to the increase of harmonic generation in a perturbative regime (dotted line) and then change in slope due to the laser intensity causing saturation (or ionization) of the non-linear medium at $\sim$7.1 $\times 10^{14} W/cm^2$ (dashed line).

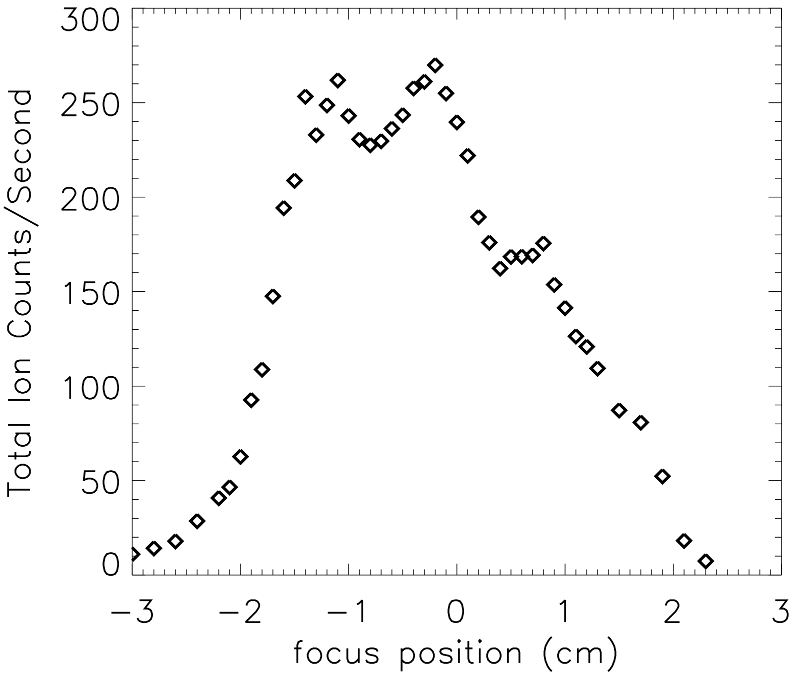

Figure 3.3: The intensity of the 9th harmonic generated in Ar as a function of the position of the driving laser focus in the gas jet. ”Zero” on the x scale designates the center of the gas jet. The lens used to focus the 9 mm diameter beam has a 40 cm focal length.

the detector.

3.3 Photoelectron Spectroscopy with soft x-ray harmonics

When both gratings are rotated to the 0th order, all the harmonics together are used for photoionization of the sample. This is the case in Fig. 3.4(a), where all the harmonics (generated in Ne) are incident on a sample of He (the same as Fig 2.12, chapter 2). The first harmonic to ionize the He 1s electron is the 17th (26.5 eV photon energy), and each successive harmonic ionizes He as well. By rotating the grating away from the specular reflection, single harmonics can be selected. Fig. 3.4(b) shows the photoelectron spectrum that results from a single harmonic incident on He, in this case the 61st. Not only do we observe the main photoionization peak, but also the first and second satellite peaks. This illustrates the feasibility for use of the high harmonics to observe photoelectron features with small cross sections (10^{-20} -10^{-22} cm^2 [39]). Since the binding energy and the cross sections of the He main and satellite peaks are well known, we are able to calculate the photon flux present in a single harmonic (chapter 2).

Figure 3.5(a) illustrates the simple photoelectron spectrum of Xe gas taken with the 11th harmonic of 800 nm (17 eV photon energy). The two peaks result from ionization of the 5p$_j$ electrons, with a spin-orbit splitting between the final Xe$^+$ j =$\frac{3}{2}$ and $\frac{1}{2}$ levels of 1.4 eV. Figure 3.5(b) is the photoelectron spectrum of Xe taken with the 47th harmonic (73 eV photon energy), with a final Xe$^+$ core 4d$_j$ level splitting (j=$\frac{5}{2}, \frac{3}{2}$) of 2 eV [45](shown on a log scale). Once the incident photon energy is high enough to eject core electrons, a series of auger electrons also appear, as well as the electrons ejected from the valence levels, which have very high photoelectron energies. Taking the relative photoelectron energy scales in (a) and (b) of Figure 3.5 into account, the core level peaks are broader than the valence level peaks, which is a result of the energy bandwidth of the harmonic used to ionize Xe. The 11th and 47th harmonics have energy bandwidths of 0.11 eV and 0.44 eV, respectively. The energy bandwidths of the harmonics are discussed in chapter 4.

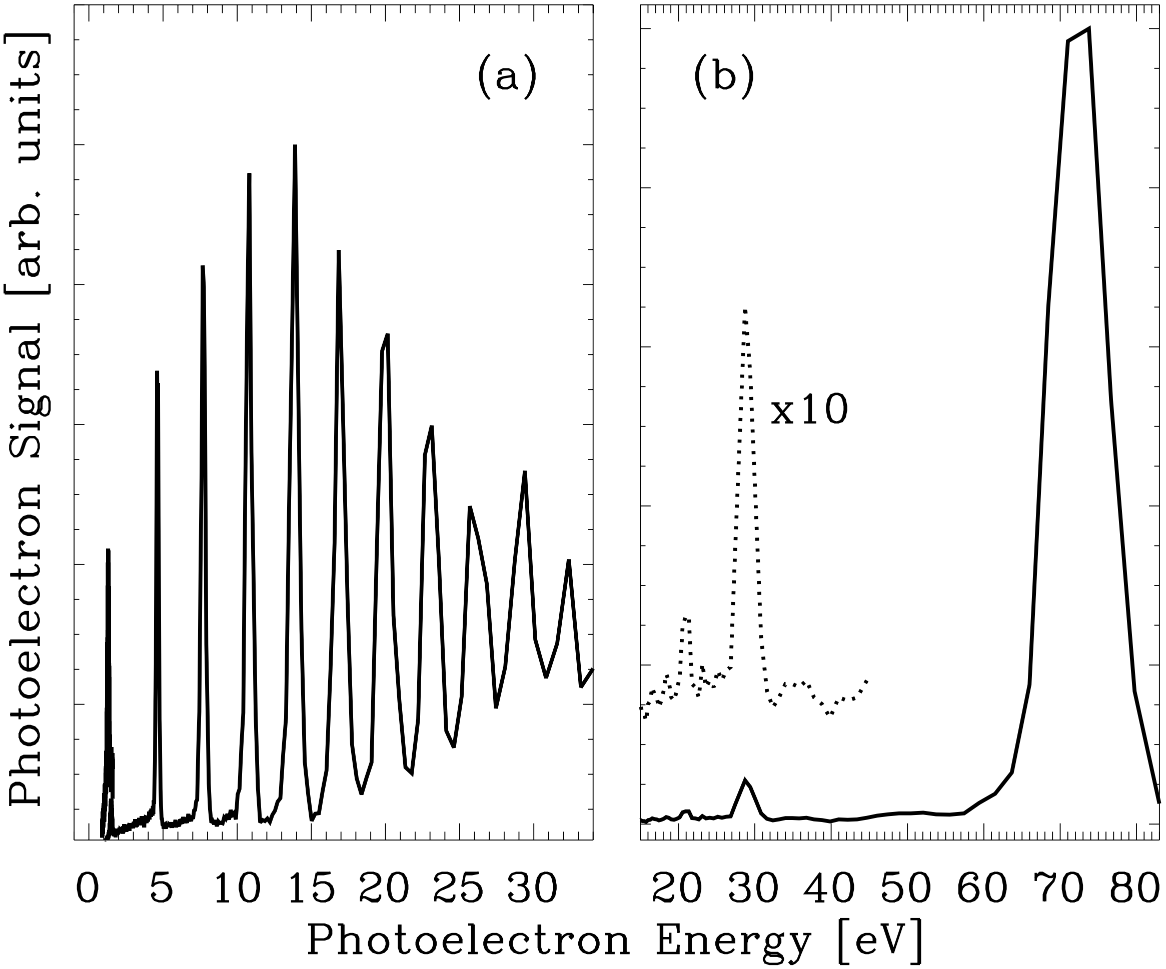

Figure 3.4: (a) Photoelectron spectrum due to all harmonics simultaneously incident on a sample of He gas. The first harmonic energetic enough to ionize He is the 17th ($E_{h\nu}$=26.4 eV). Each subsequent harmonic is seen as another main ionization peak at increasingly higher energies. (b) A single harmonic (61st, $E_{h\nu}$=95 eV), selected by the grazing incidence grating, incident on a sample of He gas. Not only is the main ionization peak seen, but also the 1st and 2nd satellite peaks.

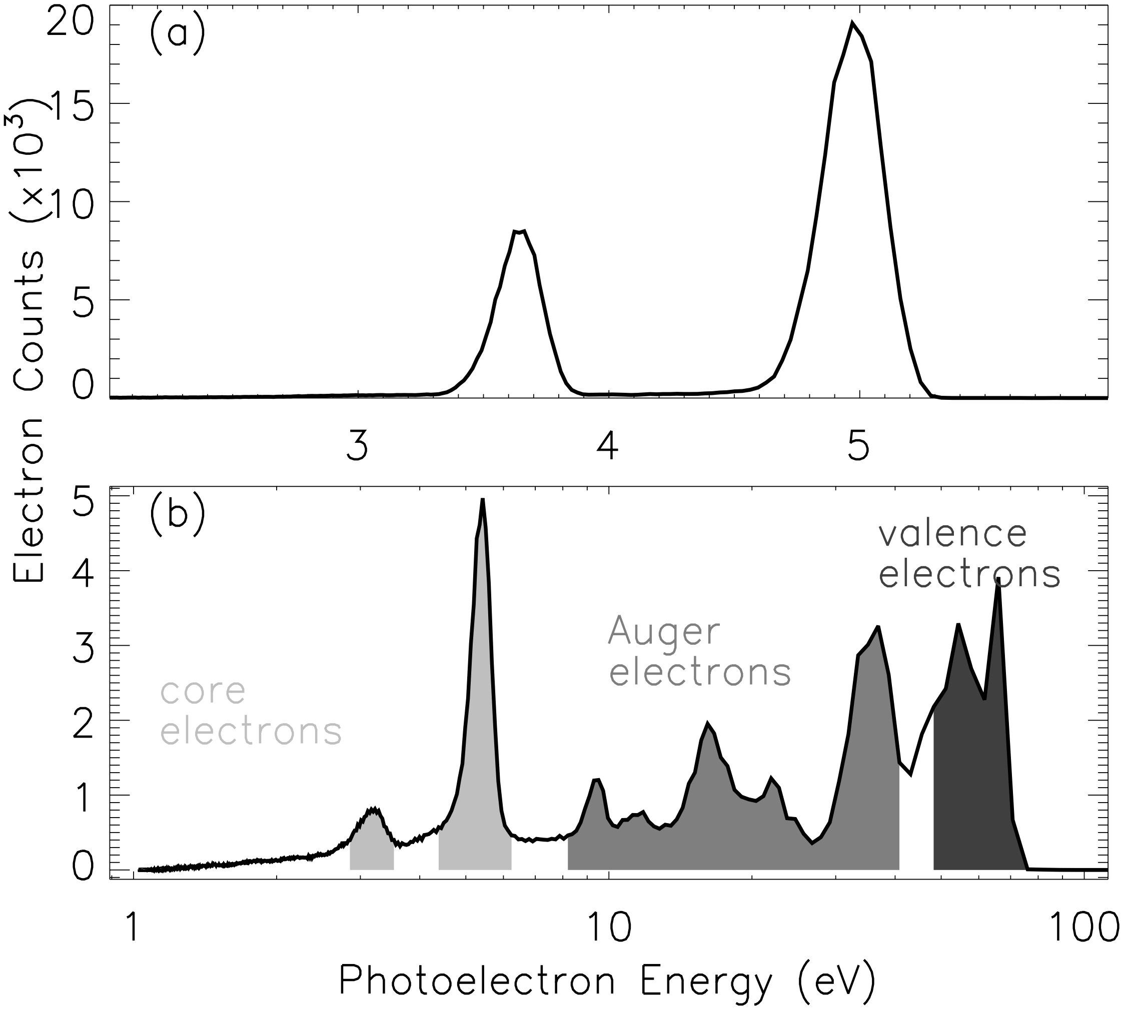

Figure 3.5: (a) The valence level photoelectron spectrum of Xe taken with the 11th harmonic (17.5 eV). (b) The photoelectron spectrum including 4d core levels of Xe taken with the 47th harmonic (73 eV). Resolution of the system is best at low photoelectron energies.

Still using Xe as the target gas, Fig. 3.6 demonstrates the tunability of the harmonic source. By tuning the fundamental 800 nm laser, we are able in effect to tune the harmonic energy. Figure 3.6 shows two spectra of Xe with the 43rd harmonic, the bottom with the fundamental laser tuned to 800 nm, and the top with the laser tuned to 791 nm. The 43rd harmonic of 800 nm is slightly below the 4d ionization threshold of Xe, and only the valence level electrons are observed. Upon tuning to 791 nm, the 43rd harmonic is slightly more energetic, and a Rydberg resonance leading up to the ionization threshold is reached. When the core electron is excited to this high Rydberg state, a series of Auger electrons results (shown as the shaded area in Fig. 3.6) due to the electron hole left in the 4d core. This added versatility of the harmonic source is important for time-resolved experiments as well, as cross-sections and accessibility of electronic states can be manipulated by adjusting the energy of the probe.

The valence and core level photoelectron spectra of Br_2 are shown in Figure 7(a) and (b). Three peaks are seen in Fig 7(a) when the 11th harmonic is incident on Br_2, corresponding to final electronic states $X(^2\Pi_g)$, $A(^2\Pi_u)$ and $B(^2\Sigma_g)$ of Br_2^+ [5, 46]. The X and A state are both spin-orbit coupled, giving a doublet peak, although the A state splitting is small compared to the energy bandwidth of the harmonic and appears as a broad peak. In the right hand panel, the spin-orbit split $4d_j$ levels of the final Br_2^+ state are observed upon illumination by the 53rd harmonic (82 eV) [2].

Similarly, the valence and core level photoelectron spectra of a more complex molecule, Al_2Br_6, is shown in Fig. 3.8(a) and (b). Al_2Br_6 is actually a dimer, made up of two $AlBr_3$ monomers and linked by two bridging bromine atoms, leaving four terminal bromine atoms [47]. Surprisingly, previous photoelectron spectra from the literature are scarce for Al_2Br_6, and the valence level spectrum obtained here differs somewhat from that reported in the literature. Reference [47] divides the spectrum of Al_2Br_6 into four sections: band A, from 10.8-12.7 eV, resulting from ionization from non-bonding orbitals of the terminal Br atoms, band B, from 13-14 eV, resulting from ionization from Al3p-Br4p bonding orbitals, band C, from 14-15 eV, resulting from ionization from the bridging Br atom lone pair orbitals, and band D, from 16-

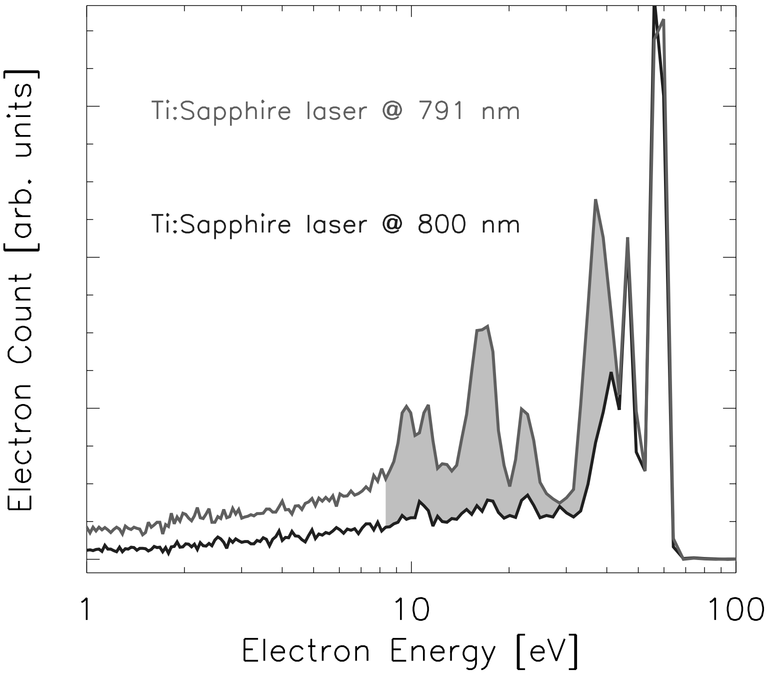

Figure 3.6: Photoelectron spectra in Xe with the 43rd harmonic, demonstrating the ability to tune the harmonic to an atomic Rydberg resonance. The bottom spectrum is the 43rd harmonic of 800 nm, while the top spectrum is the 43rd harmonic of 791 nm. By tuning the fundamental beam, the harmonic is tuned into a Rydberg level leading up to the 4d ionization threshold. The hole left by the excited electron causes an onset of Auger electrons (shaded area).

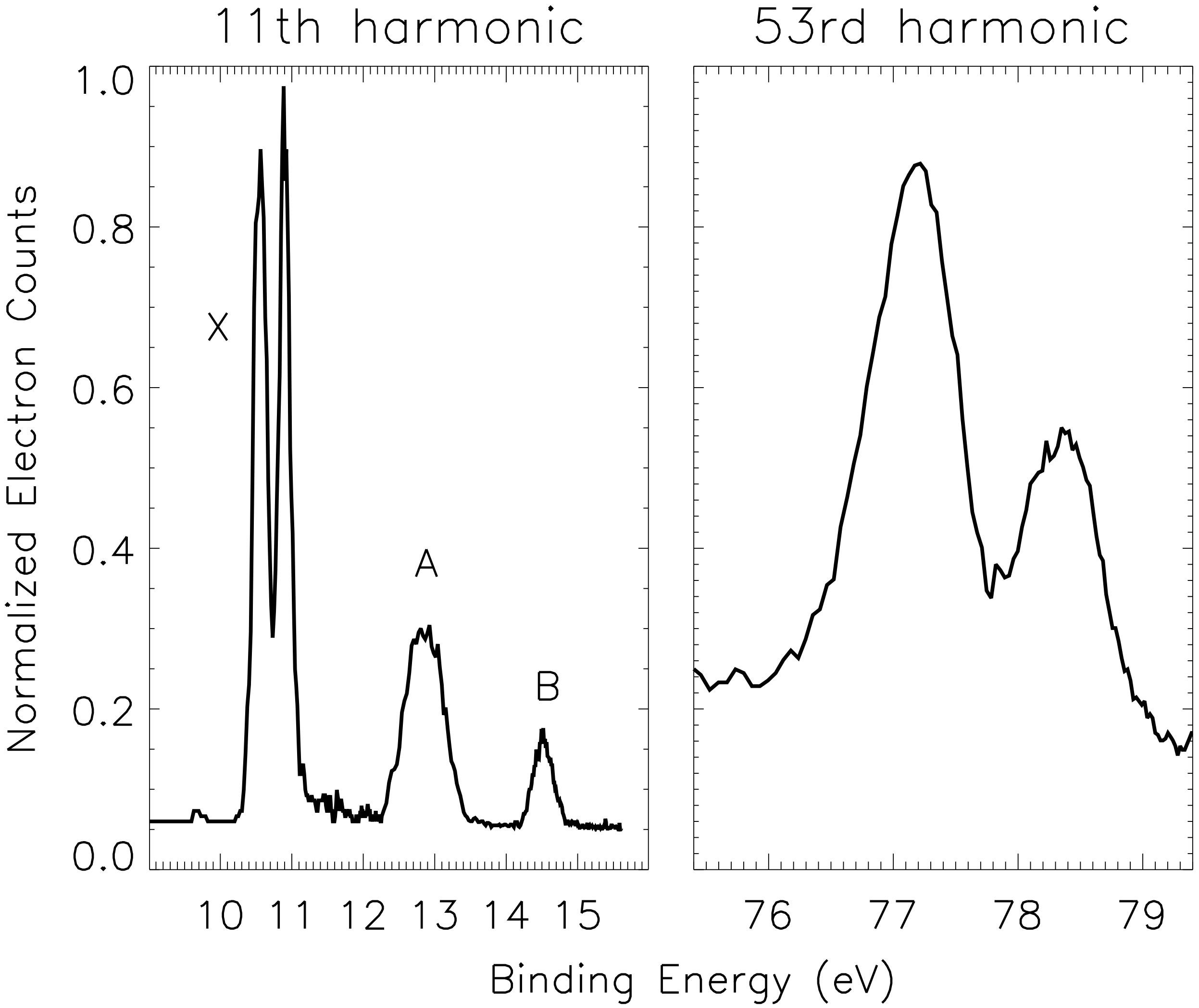

Figure 3.7: (a) The valence level photoelectron spectrum of Br_2 taken with the 17th harmonic (26 eV), showing the X, A and B final states of Br_2^+. (b) A section of the photoelectron spectrum of Br_2 taken with the 49th harmonic (76.5 eV), showing the $3d_j$ core levels of Br_2^+.

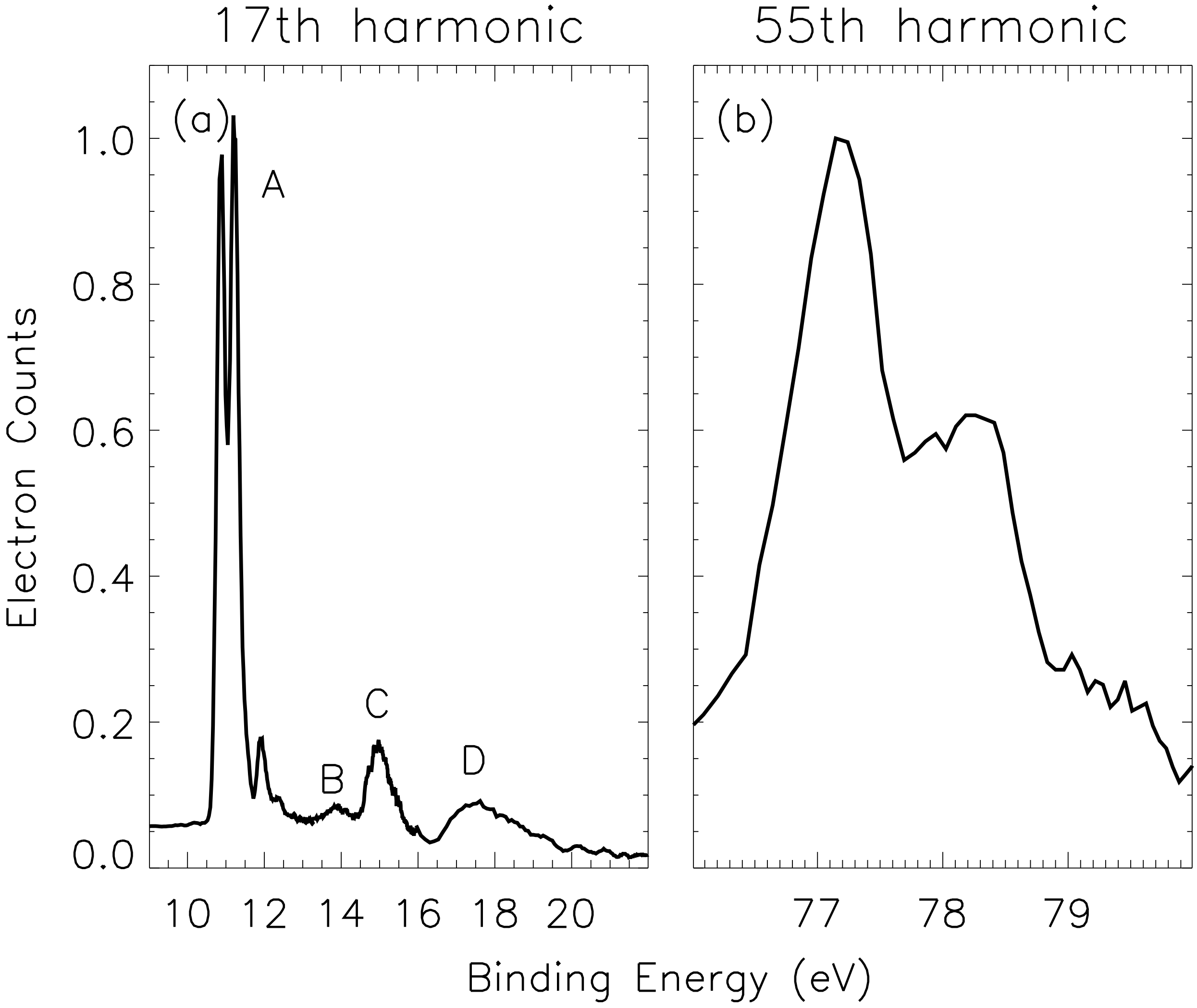

Figure 3.8: (a) The valence level photoelectron spectrum of Al_2Br_6 taken with the 19th harmonic. (b) The core level photoelectron spectrum of Al_2Br_6 with the 55th harmonic showing the bromine core levels. Al core levels were not observed.

17 eV, resulting from ionization from the Al3s-Br4p orbitals. While each of these regions is observed in our photoelectron spectrum, the intensity ratios between the peaks is considerably different that in Ref. [47]. A HeI source was used in Ref. [47] to obtain the spectrum, which produces radiation at 584 Å, or 21.2 eV, while the 17th harmonic has a photon energy of 26 eV. While differences in ionization cross-sections could account for intensity variations between the two spectra, it is not expected to have a dramatic effect. From a simplistic picture, the low binding energy band does indeed resemble that from Br_2, supporting the statement that they originate from the terminal Br atoms. A more thorough theoretical treatment of this molecule is needed for a conclusive interpretation of the spectrum.

Figure 3.8(b) shows the core level photoelectron spectrum of Al_2Br_6 using the 55th harmonic. The observed bromine core levels are very similar to the Br_2^+ core level spectrum in Fig. 7(b). The low binding energy peak is nearly identical, while the high binding energy peak appears broader by about 20% and slightly shifted ($\sim$ 0.2 eV) to lower binding energy. This is consistent with the conclusions of Ref. [2], stating that lower electronegative substitutents (Al) produce a lower binding energy for the Br^+ 3d core levels. Some broadening might also be expected due to the presence of both terminal and bridging Br atoms. The feature at higher binding energy (79.5 eV) could be evidence of the observation of Al 2d core levels, expected to be $\sim$2 eV higher than the Br core levels, with a splitting of only 0.4 eV. The intensity ratio is also roughly consistent with the ratio of Br atoms to Al atoms (3:1).

For reference, photoelectron spectra of other gas phase molecules taken with the harmonics are shown in Figs. 3.9, 3.10, and 3.11, which are spectra of I_2, CH_2I_2, and $GeBr_4$, respectively. Descriptions and references (if available) are given in the figure captions.

3.4 Photoelectron spectroscopy of solid samples

As mentioned in chapter 2, I also had the opportunity to use harmonics from an 800 nm laser to obtain photoelectron spectra of solid samples. To calibrate the high-harmonics generated, a cleaved GaAs (100) surface was used as the sample. The 3d core levels of Ga

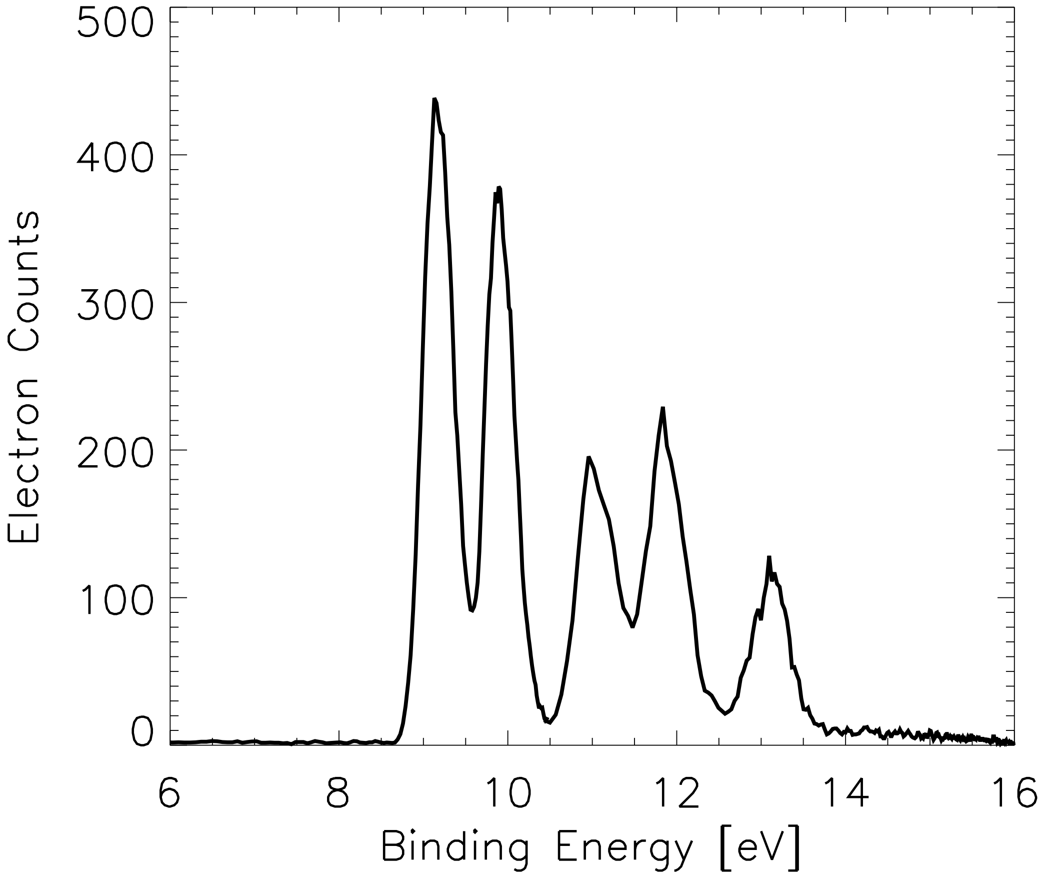

Figure 3.9: The photoelectron spectrum of I_2 taken with the 17th harmonic of 800 nm. The I_2 spectrum has a similar structure to Br_2, except that the spin orbit splittings in the ion are more pronounced. The $^2\Pi_g$ state at 9.3 and 10 eV binding energies, the $^2\Pi_u$ state at 11 and 11.8 eV, and the $^2\Sigma_g^+$ state at 13 eV of the I_2^+ ion are observed [5]

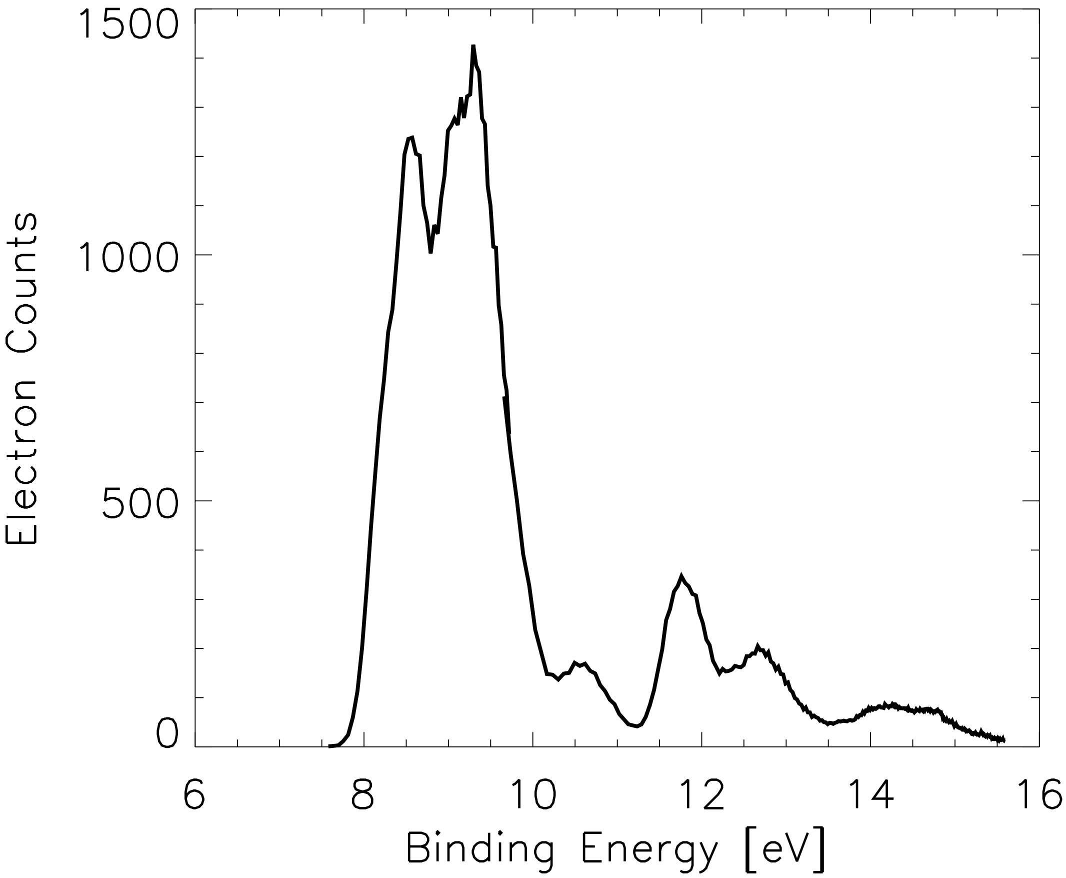

Figure 3.10: The photoelectron spectrum of CH_2I_2 with the 17th harmonic of 800 nm.

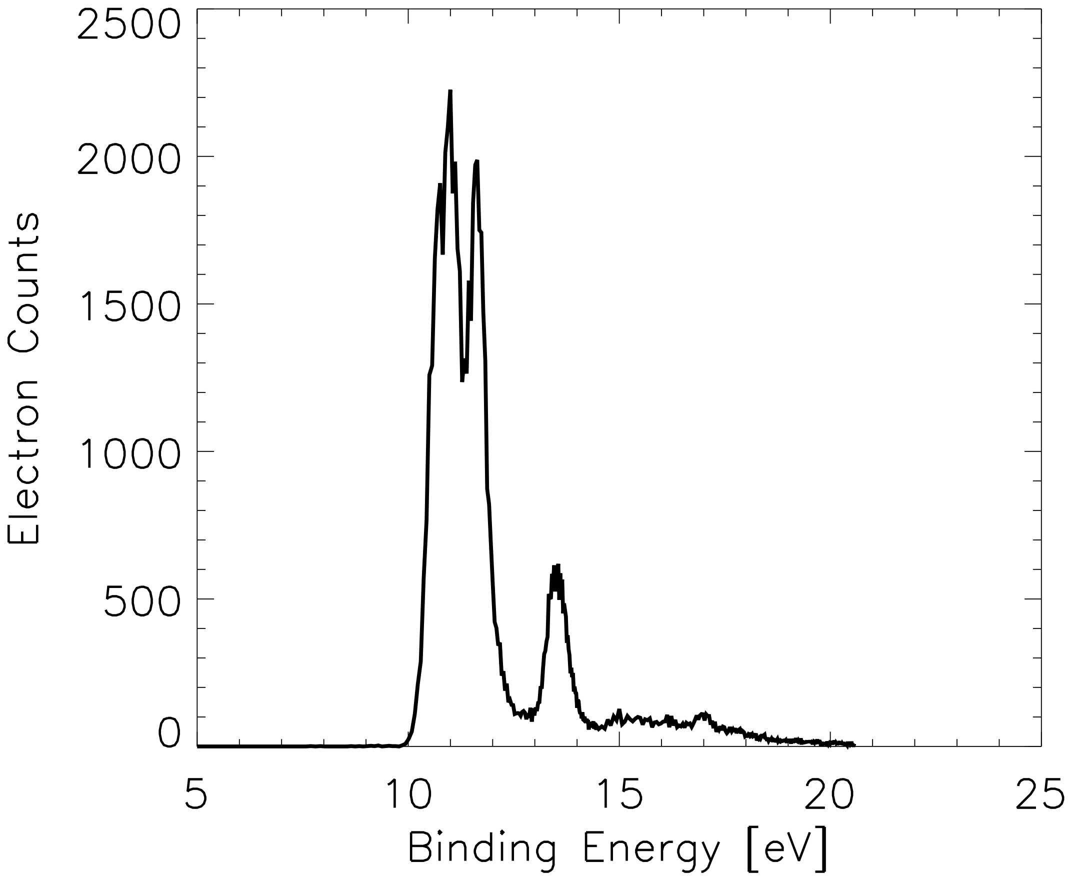

Figure 3.11: The photoelectron spectrum of $GeBr_4$ with the 17th harmonic of 800 nm.

and As are 19 and 41 eV, respectively [48]. Spectra taken with various harmonics are shown in figure 3.12, where photon energies of 42 V, 63.5 eV, 79 eV and 98 eV correspond to harmonics 27, 41, 51 and 63 of 800 nm. As can be seen from the figure, the 27th harmonic does not have sufficient energy to ionize the 3d core levels of As, but only Ga. The 41st harmonic is just above the 3d ionization threshold for As, so the collection effeciency is low for the low energy photoelectrons. The spectrum with the 51st harmonic shows the strongest peaks for both Ga and As. The photon flux of the 63rd harmonic is considerably lower than for the 51st, when comparing the spectra, due to the 63rd harmonic being near the cutoff region for harmonic generation.

The next step was to observe a photoelectron signature of chromium metal on a silicon surface. Fig. 3.13 shows photoelectron spectra of a thin layer of Cr metal ($\sim$70 Å) on a Si (100) surface. The Cr core level signature (3p, binding energy=41.2 eV [49]), while weaker than the Ga and As 3d levels, can clearly be seen upon ionization with the 47th, 55th and 59th harmonics. Though photoelectron spectra were attempted after depositing Cr on a Si surface by introducing $Cr(CO)_6$ to a liquid N_2 cooled surface, the results were inconclusive and more experiments need to be done (i.e., time ran out!).

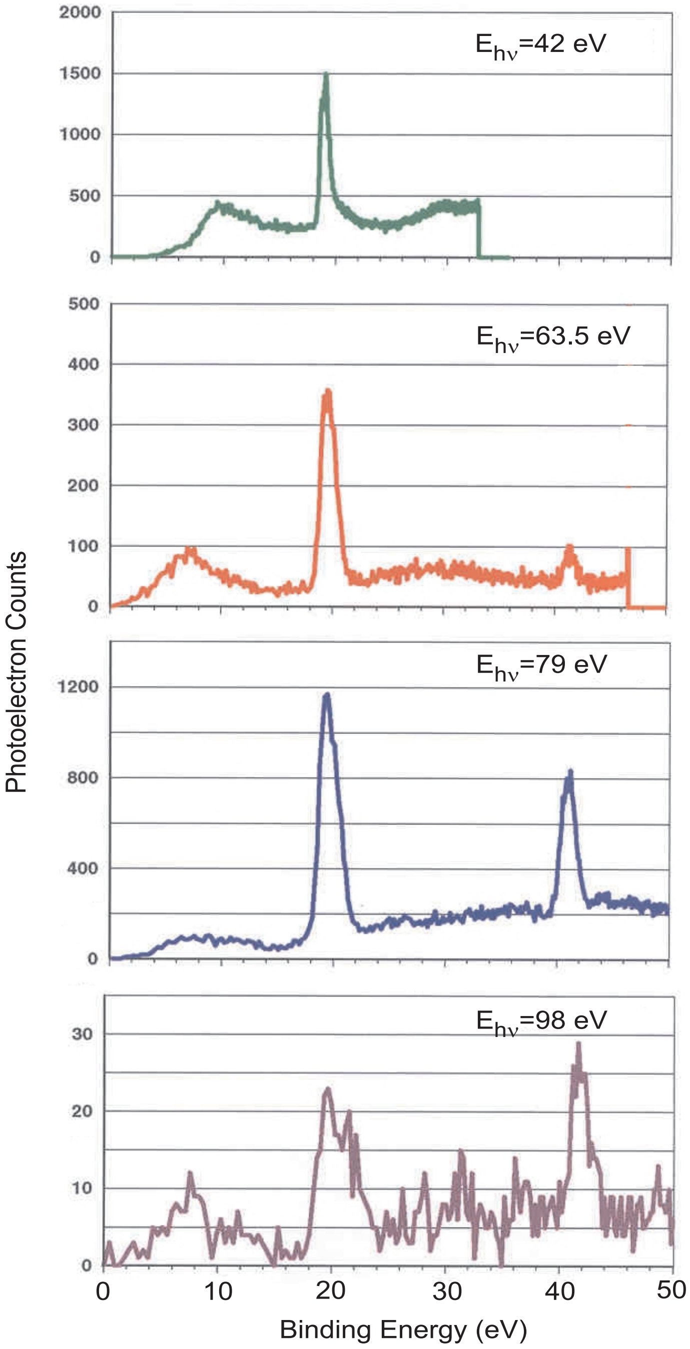

Figure 3.12: Photoelectron spectra of a GaAs (100) surface taken with harmonics 27, 41, 51 and 63 (top to bottom) of an 800 nm Ti:Sapphire laser. The 3d core levels of Ga and As are observed at 19 and 41 eV binding energies, respectively.

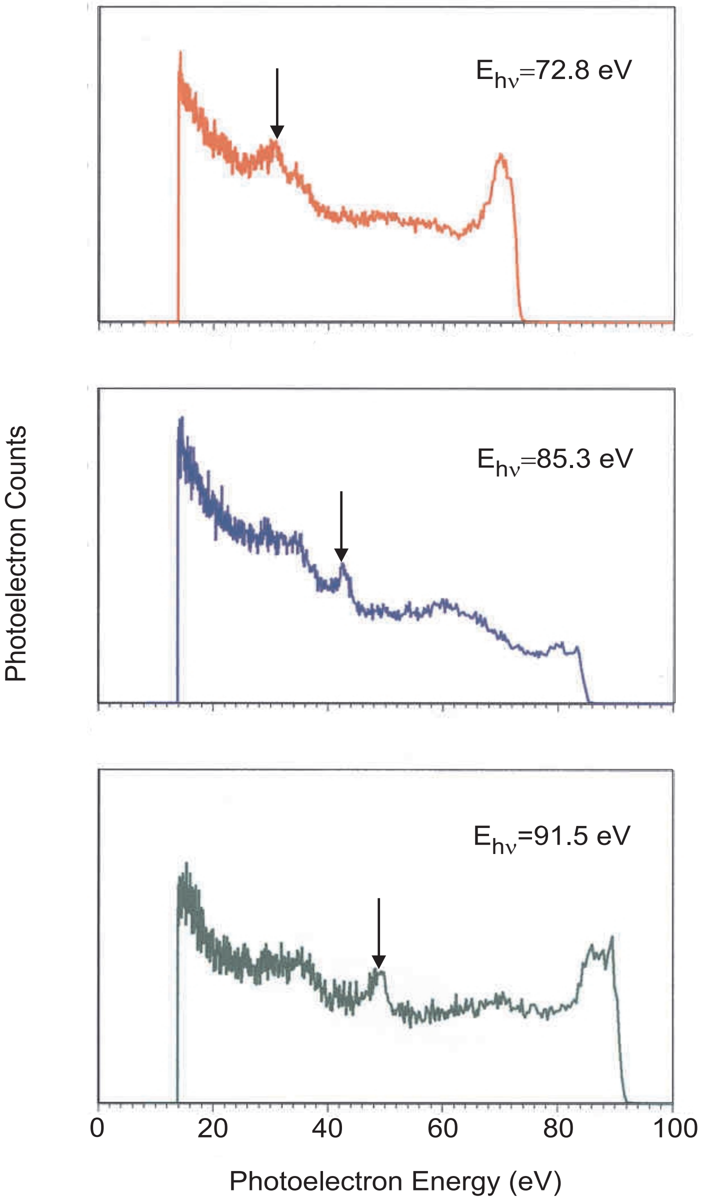

Figure 3.13: Photoelectron spectra of chromium metal on a Si(100) surface. The 3p core level is observed at 41 eV binding energy for three different harmonics (47, 55 and 59 from top to bottom).

Chapter 4

Energy bandwidths of the harmonics

The energy bandwidths of the generated harmonic light will ultimately determine the resolution of the photoelectron spectra obtained, as discussed in chapter 2. High resolution cannot be expected with an ultrafast source, due to the short pulse length and consequent large frequency bandwidth of the laser. However, moderate resolution is needed to observe not only energy splittings in static photoelectron spectra of atoms and molecules, but also to resolve chemical shifts when using the harmonics for pump probe spectroscopy. Therefore, a systematic study of the bandwidths of the harmonics generated in neon was accomplished, as is described here.

The energy widths of low energy photoelectron peaks (below 3 eV) result from the energy width of the harmonic used to ionize the sample. This is demonstrated in Fig. 4.1, where the same spectrum of NO gas taken with a narrowband Nd:YAG laser (10.5 eV) and with the 7th harmonic of the Ti:Saphhire laser (10.85 eV) are overlaid. The dotted line in this figure is the same as in Fig. 2.11, showing the inherent resolution of the magnetic bottle spectrometer. The solid line, resulting from ionization with the 7th harmonic of the Ti:Sapphire laser, demonstrates the broadening of the photoelectron peaks due to the energy bandwidth of the 7th harmonic.

The $\Delta E_{pe}/E_{pe}$ for any magnetic bottle system is approximately a constant number with E_{pe} [35], therefore limiting the useful energy range over which bandwidth information of the light source can be obtained. For example, for a $\Delta E_{pe}/E_{pe}$ of 5% there is already a spec-

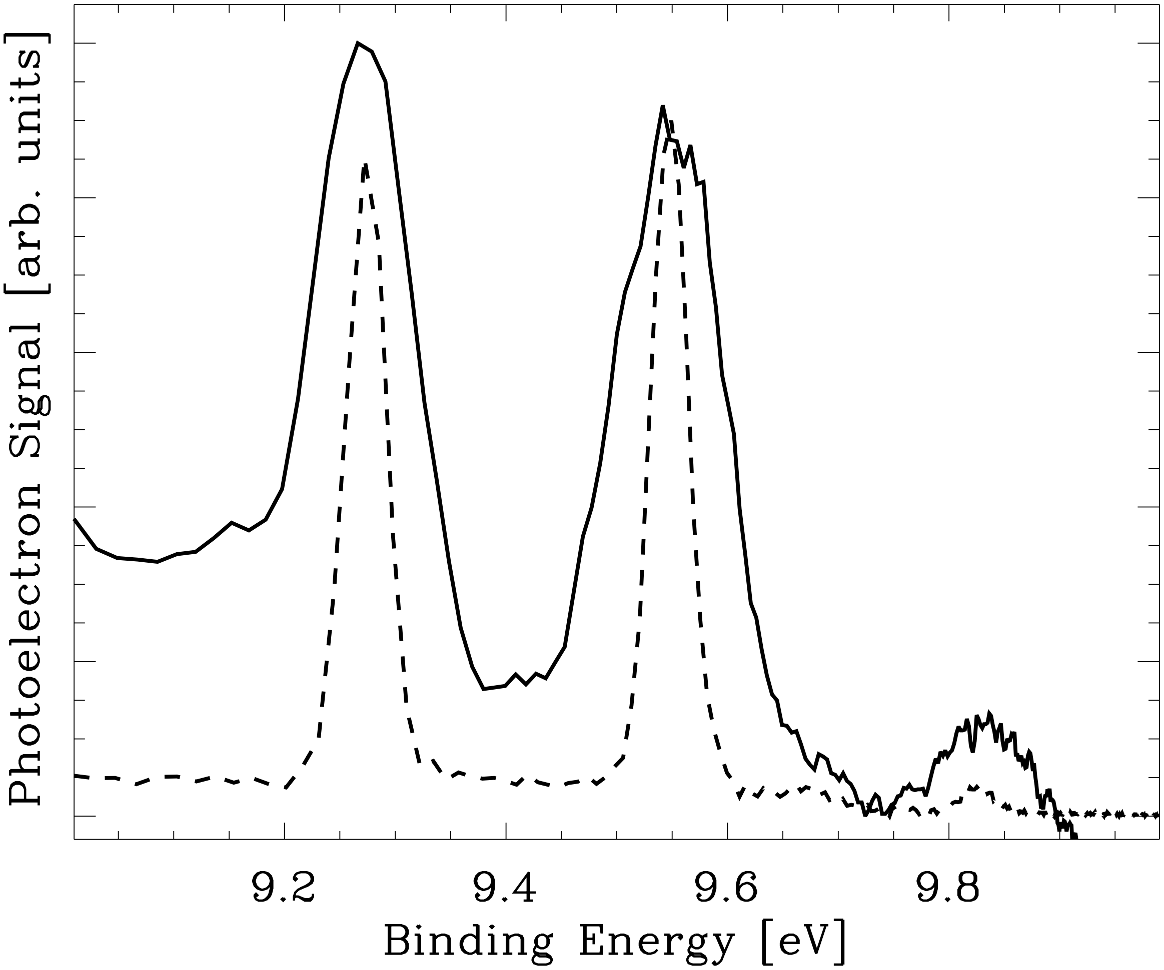

Figure 4.1: Photoelectron spectrum of NO gas taken with the 9th harmonic of a long pulse, narrowband Nd:YAG laser, $E_{h\nu}$=10.496 eV (dashed line). Here the inherent resolution of the magnetic bottle spectrometer is seen in the peak widths. The vibrational progression of the NO$^+$ ground state gives rise to the three peaks separated by $\approx$0.28 eV. The solid line shows the same vibrational progression, but acquired with the 7th harmonic (centered at $E_{h\nu}$=10.91 eV) of the fs Ti:Sapphire laser. The broadening of the peaks is due to the energy bandwidth of the 7th harmonic. The height discrepancy in the highest binding energy peak between the Nd:YAG laser and the 7th harmonic of the Ti:Sapphire laser is due to the efficiency of the photoelectron spectrometer at different photoelectron energies. Though these peaks have the same binding energy, the dashed line peak at 9.8 eV corresponds to very low photoelectron energy, where the collection efficiency is quite low.

trometer broadening of 0.25 eV at a photoelectron energy of 5 eV. Therefore, for photoelectron peaks at energies beyond 5 eV, a broadening due to the energy bandwidth of the photon source that is less than 0.25 eV is masked by the spectrometer resolution. This means that unambiguous bandwidth information can only be extracted from low kinetic-energy photoelectron peaks. In this work two methods are therefore utilized. Specific atomic or molecular transitions that fortuitously yield low energy electrons for certain harmonics are studied in one series of measurements and the retarding grids are used to lower the electron energies in the other.

To obtain bandwidth measurements of the harmonics, photoelectron spectra of several atomic and molecular gases were taken, using either the specular reflection of the gratings or individual harmonics. From these photoelectron spectra, we measured photoelectron peaks resulting from ionization of a number of different harmonics. First, by using several different target gases, it is possible to obtain low energy photoelectron peaks directly resulting from ionization with a range of harmonics. Each atom or molecule has a characteristic ionization potential and precise core-level binding energies.

In addition to Xe (see Fig. 3.5, chapter 3), photoelectron spectra of Ne, Ar, and Kr were also taken. Similar to Xe, the main ionization peaks of these other rare gases exhibit a doublet structure due to the spin-orbit splitting of the ionic ground state. This splitting is too small in the cases of Ne and Ar to be fully resolved and the corresponding peaks were not used for bandwidth measurements. Ionization of rare gases from ns levels, on the other hand, does not suffer from spin orbit splitting, but the cross sections are generally small. This ionization process was only observed in the case of Ne.

Photoelectron spectroscopy of molecular gases with the harmonics is also possible, and several peaks from N_2 and NO were measured. The peaks from NO, shown as the solid line in Fig. 4.1, are especially important, since they represent the same vibrational progression that was obtained with the narrow band Nd:YAG laser, except using the 7th harmonic of the Ti:Sapphire laser. Comparison of the two spectra in Fig. 4.1 clearly shows the broadening of the photoelectron peaks due to the bandwidth of the 7th harmonic.

Using all the data discussed above from He, Kr, Xe, N_2, and NO, we measured the full-width at half maximum of several photoelectron peaks with energies ranging from 1-20 eV. In Fig. 4.2, a plot of $\Delta E_{pe}/E_{pe}$ vs. photoelectron energy, E_{pe}, is shown. From this figure two different trends in measured bandwidth can be seen. The high kinetic energy photoelectron peaks converge to a value around 5% which is due to the spectrometer resolution, and the peaks below $\approx$ 4 eV photoelectron kinetic energy show a steep rise, where the bandwidth is primarily due to the energy width of the harmonic light used to eject that electron. We then take the points below 4 eV in Fig. 4.2 and, after deconvolution with the spectrometer width, plot ΔE_{pe} (now equal to $\Delta E_{h\nu}$) as a function of photon energy, $E_{h\nu}$, in Fig. 4.3(a). All the points in Fig. 4.3(a) were taken without the use of the retarding grids.

A more complete study was done, however, by utilizing the retarding grids in the magnetic bottle system. In this way, a particular transition (for example, the main ionization peak of He) can be selected, and the electron kinetic energy is shifted into the region where the bandwidth of the laser dominates the spectrometer width for each harmonic (under 3 eV photoelectron kinetic energy after deceleration) . Fig. 4.3b shows $\Delta E_{h\nu}$ vs. $E_{h\nu}$ for the measured bandwidths of all harmonics from the 9th to the 55th using the main ionization line in He and the Xe $\rightarrow$ Xe$^{+}(5p_{3/2})$ and Xe $\rightarrow$ Xe$^{+}(4d_{5/2})$ transitions. It can be seen from comparison of the two plots in Fig. 4.3 that the general trend is very similar, which gives confirmation that any broadening effect of the retarding grids can be ruled out. A list of the average $\Delta E_{h\nu}$ values for harmonics 9-55 is given in Table 4.

In Fig. 4.2, the natural widths of the Xe 4d core level peaks are taken into account. Core level ionization results in an ionic core hole state that decays very rapidly via Auger processes. Hence, core level photoelectron peaks may exhibit a significant natural linewidth. The width of the Xe 4d levels has been the subject of several previous investigations, which report widths between 0.10 and 0.12 eV [50, 51]. The measured widths of the Xe 4d peaks in Fig. 4.3 and Table 4 are corrected for both the spectrometer broadening and the natural linewidth.

Another source of chirp and thus temporal broadening of the high harmonics stems from

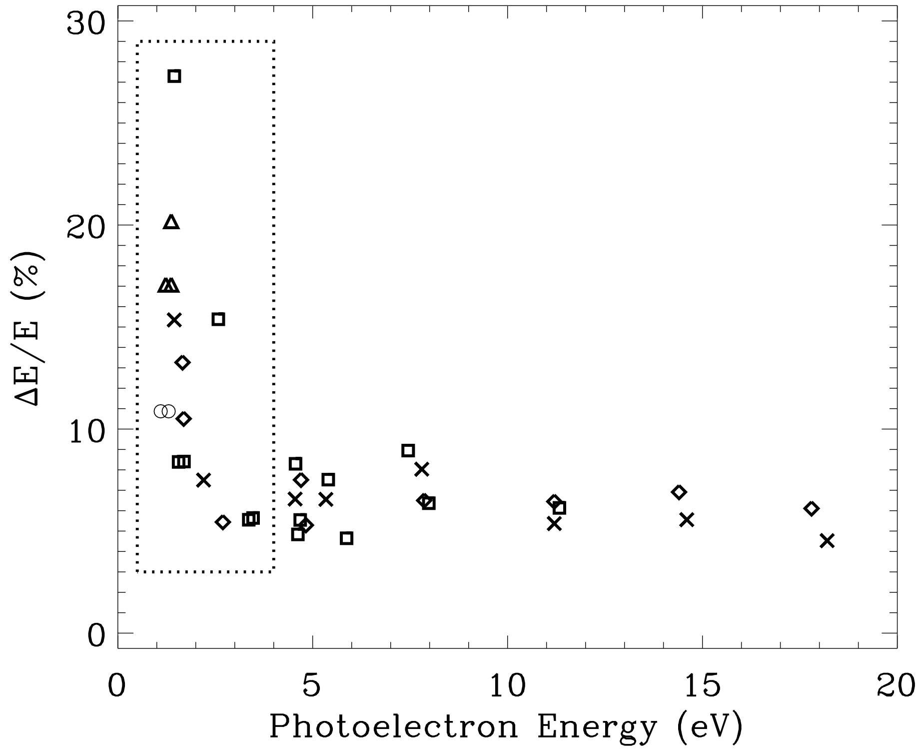

Figure 4.2: The relative energy width of photoelectron peaks from several different gases vs. their respective photoelectron energies. The higher energy photoelectron peaks converge to a relative width of 4-5%. For photoelectron peaks below ≈4 eV a new trend can be seen, where the ΔE of the peaks is due to the energy bandwidth of the harmonics. Target gas is He (◇), Ne (×), Xe (□), N_2 (△), and NO (◯).

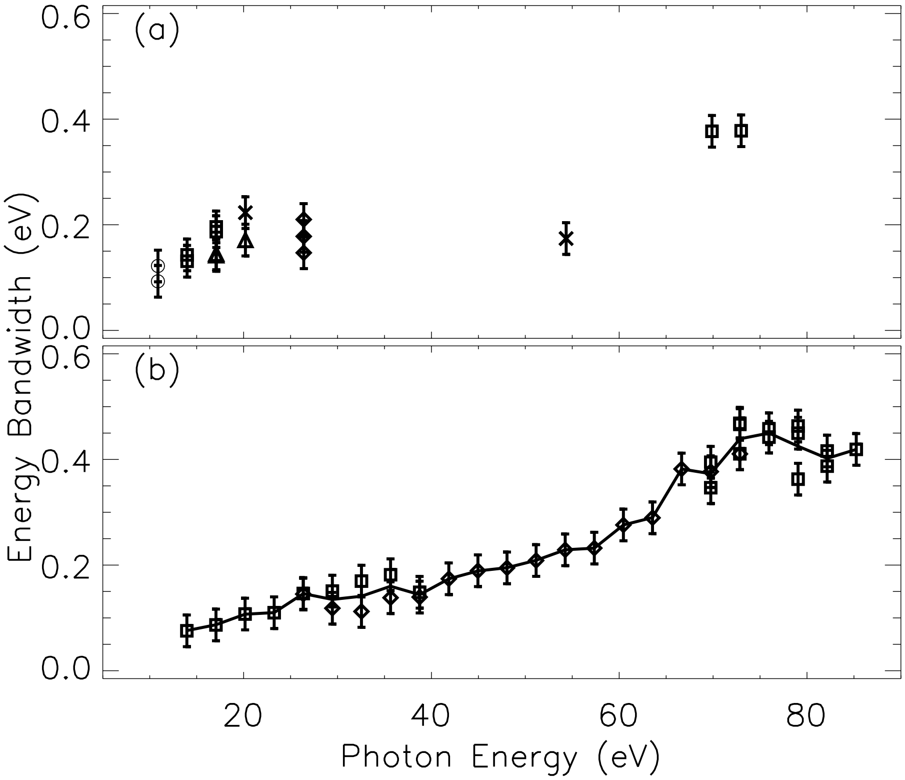

Figure 4.3: (a) The absolute energy width of the harmonics derived from low energy photoelectron peaks (below 3 eV) are plotted as a function of the photon energy, or the harmonic used to ionize the electron from which the peak arises. The retarding grids in the electron flight tube were not used for this data set. (b) A more complete data set using the retarding grids to measure the bandwidths of all the harmonics from the 9th to the 55th. Comparison of (a) and (b) shows that no artificial broadening exists when utilizing the retarding grids. Target gases are He (◇), Ne (×), Xe (□), N_2 (△), and NO (◯), and the solid line is the average for each harmonic.

Harmonic	ΔE (eV)	Harmonic	ΔE (eV)
7	0.11	33	0.21
9	0.08	35	0.23
11	0.09	37	0.22
13	0.10	39	0.28
15	0.11	41	0.29
17	0.15	43	0.38
19	0.14	45	0.37
21	0.14	47	0.44
23	0.16	49	0.45
25	0.14	51	0.43
27	0.17	53	0.40
29	0.19	55	0.42
31	0.20		

Table 4.1: Energy bandwidths for harmonics 7-55 generated in neon

the harmonic generation process itself. It has been reported that an unchirped driving pulse produces negatively chirped harmonics and that the best high harmonic generation is achieved if the driving pulse is slightly positively chirped [52]. We have investigated the effect of a chirped fundamental pulse on the high harmonic photoelectron spectra for both positive and negative chirps of up to 0.3 nm/fs. While for small positive chirps of ≈0.1 nm/fs the harmonic generation efficiency is slightly improved compared to an unchirped driving pulse, the efficiency drops off strongly for more positively and for negatively chirped pulses. The measured bandwidths, however, remain constant except for large negative chirps where a broadening of about a factor of 1.5 was observed. A demonstration of this is seen in Fig. 4.4, where photoelectron spectra of NO with both the 7th and the 9th harmonic are shown. Very little broadening in the photoelectron spectra can be seen between spectra with an unchirped, negatively chirped or positively chirped pulse, in contrast to the results from ref. [52] where chirping the 10 fs driving pulse gave either discreet harmonics (negative chirp) or a continuum (positive chirp). Though no broadening effects are observed, small energy shifts in the spectrum indicate the center wavelength of the harmonic is effected as the fundamental laser chirp is varied. This could be due to a change in the wavelength of the fundamental laser.

In one experiment with similar conditions to the system here, a narrow slit monochromator is used to scan through the 27th harmonic of a 140 fs Cr:LiSAF laser. The energy bandwidth of the 27th harmonic is found to be $\approx$0.12 eV [53]. This agrees well with the result from this work (0.17 eV for the 27th harmonic), because a slightly larger energy bandwidth is expected here corresponding to our shorter pulse length. In another experiment, the 7th and 9th harmonics of a 100 fs Ti:Sapphire laser are measured to have a FWHM of $\approx$0.1 eV [40], also consistent with the measurements here. Measured bandwidths of harmonics generated by picosecond lasers, such as in Ref. [54], are quite narrow and cannot be compared directly to the results found here. Though other harmonic spectra are reported throughout the literature [20, 21, 41, 55], bandwidth measurements are not discussed and are not easily derived from the figures.

The general trend seen in Fig. 4.3 is a gradually increasing bandwidth from the 7th harmonic to the 45th harmonic, from 0.11($\pm$0.03) eV to 0.37($\pm$0.03) eV. The higher harmonics, from the 47th-55th, seem to reach a plateau centered around 0.43 eV. Theoretical treatments of spectral width vs. harmonic number do exist for driving laser pulses $\leq$30 fs [25, 26]. Comparison of the results reported here and these theoretical predictions is difficult for several reasons. First, for longer driving laser pulses, theory becomes increasingly difficult as more optical cycles must be treated numerically. Second, for very short pulses, saturation due to ionization of the non-linear gas medium is not reached, since the response time of the atoms is slow compared to the temporal envelope of the pulse. In the case of longer pulses, however, saturation is reached somewhere after the peak of the pulse on the falling edge. Nevertheless, we believe it is beneficial to mention the results of theoretical calculations and draw comparisons where it is appropriate.

According to calculations in the single atom picture of harmonic generation from short pulses, the phase structure of the generated harmonics plays a significant role [25]. A simple quadratic phase structure gives rise to linear chirp in the pulse, and no broadening of the spec-

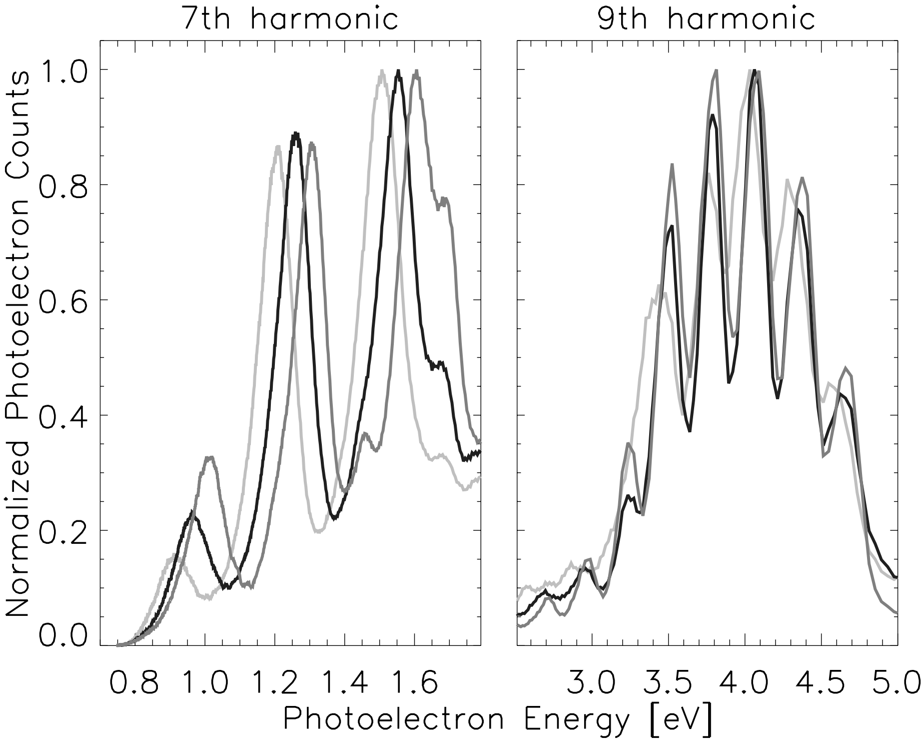

Figure 4.4: The photoelectron spectrum of NO gas with the 7th harmonic (left) and 9th harmonic (right), showing the vibrational progression of the NO^+ ground state. The black spectrum represents the 70 fs unchirped pulse, while the light gray spectrum is taken with a positively chirped driving pulse and the dark gray spectrum is taken with a negatively chirped pulse.

trum within the pulse occurs. On the other hand, a complex phase structure with higher order terms leads to non-linear chirp and thus broadening of the spectrum through the introduction of new spectral components. The phase of the generated harmonics is said to be dependent on the intensity variation of the driving pulse, which changes dramatically during harmonic generation for a very short pulse. In this single atom picture, the lower and mid range harmonics have a complex phase structure, due to the fact that these harmonics are created over a larger number of optical cycles, with contributions from the rising edge, the peak, and the falling edge of the pulse. The higher harmonics near the cutoff, however, are created over the few optical cycles near the peak of the pulse, giving rise to a simple quadratic phase structure. This leads to a calculated harmonic spectrum with broad, unresolved lower harmonics and well resolved harmonics near the cutoff.

However, when the macroscopic conditions of harmonic generation are considered in addition to the single atom response, the results can be much different. In ref. [26], several aspects of the bulk medium are considered, such as phase matching and the focus position of the laser with respect to the gas jet. They give a two trajectory picture of harmonic generation, where the ionized electron can return to the ion on a short or long trajectory. These two trajectories can interfere with each other, or one can dominate depending on the conditions of harmonic generation. If the jet is located after the focus, the short return time is dominant, which results in a weak intensity dependence of the phase. This gives rise to a well-resolved spectrum with decreasing widths for decreasing harmonics orders. If the jet is at the focus, the calculated spectrum shows the opposite trend.

The argument that the high harmonics near the cutoff are created only near the peak of the driving pulse is expected to remain true for 70 fs pulses. Therefore, it could be argued that the plateau seen in Fig. 4.3(b) is due to this effect, namely that the harmonics in the cutoff region exhibit only a constant linear chirp and no further broadening is seen. It may seem that the two trajectory picture could account for the fact that we see a decreasing bandwidth with decreasing harmonic number but we do not observe any difference in the bandwidths of the high harmonics when the position of the jet with respect to the focus is changed. We therefore conclude that a theoretical study based on the particular parameters of this experiment is needed to fully explain the observed bandwidth trends.

Chapter 5

Photoelectron spectroscopy of the excited $^3\Pi_{0+u}$ B state of Br$_2$

5.1 Introduction

Photoelectron spectroscopy of molecular excited states has been a topic of interest in many research groups, largely since the introduction of pulsed lasers [56]. The pulsed laser allows for a technique termed Resonance Enhanced Multi-Photon Ionization, or REMPI. In REMPI, one or more photons are used to excite a molecule to an intermediate state, and several additional photons (either of the same wavelength or a new wavelength) are used to ionize the molecule, as is demonstrated in Fig. 5.1. In this example, the photoelectron spectrum observed is due to the Franck-Condon overlap (overlap of the vibrational wavefunctions) between the excited neutral state and the ground ionic state. Specifically, the REMPI technique has been used to study processes such as one-photon forbidden transitions (O_2), super-excited states (NO), small van der Waals complexes (NO-Ar), and structural isomers and IVR (internal vibrational relaxation) of several organic molecules [57].

While REMPI has been largely successful, some difficulty exists using a multi-photon ionization step, similar to the discussion in chapter 1. First of all, it is possible to inadvertently overlap a second resonance during the ionization step (such as a Rydberg state), in which case the photoelectron spectrum observed is due to the overlap of this second resonantly excited state and the ion state [58]. Secondly, the total energy of the probe is still limited by the number photons available, where the probability of adding an additional photon decreases as ρ^n, where ρ is the density of photons and n is the number of photons.

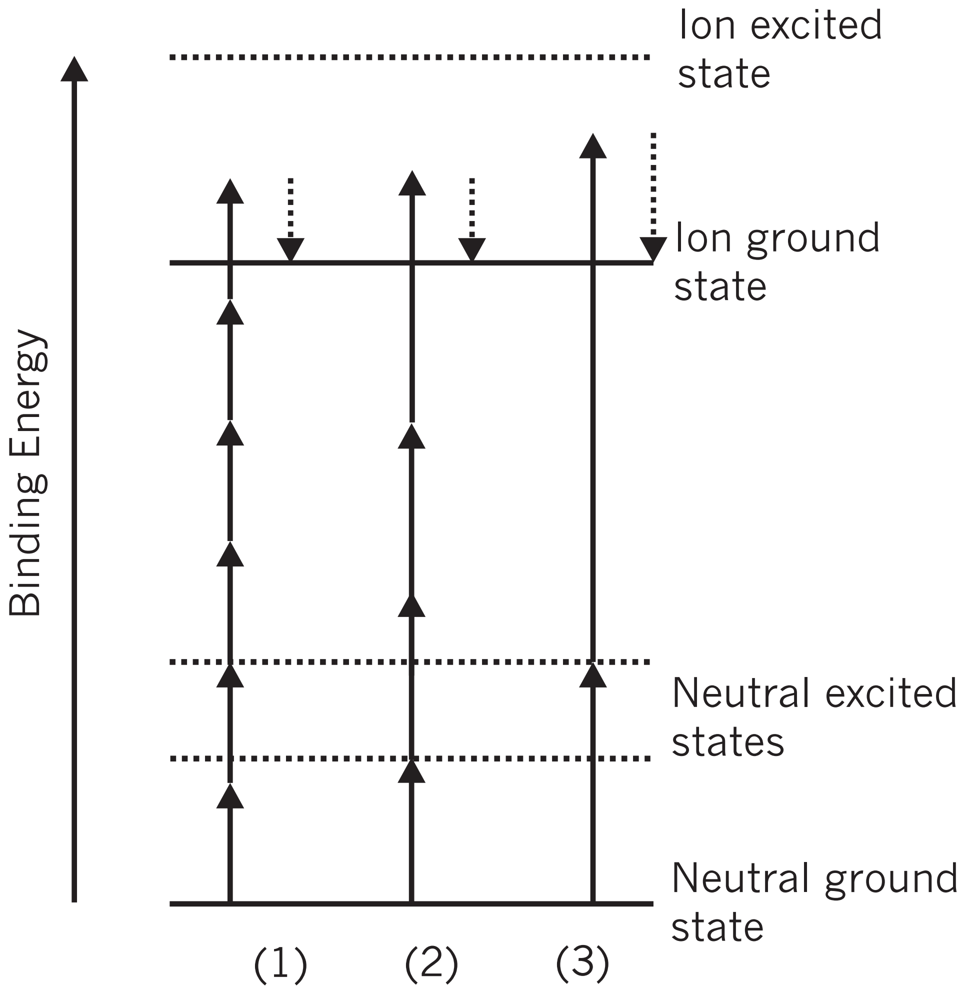

Figure 5.1: A schematic of resonantly-enhanced excited state photoelectron spectroscopy of a generic molecule. Process (1): A single frequency photon used to resonantly excite an intermediate state and ionize it with a multi-photon probe. Process (2): A two-color REMPI process where one photon resonantly excites the molecule and a photon of a different wavelength is used to multi-photon ionize the molecule. Process (3): A two-color excitation-ionization scheme where one visible photon is used to resonantly excite an intermediate state and a VUV photon is used for single photon ionization. The dotted arrows represent the photoelectrons ejected from the three different processes.

A two-color, two-photon excitation-ionization scheme has also been demonstrated in the literature as a supplement to the information already available using the REMPI technique [59] (also shown in Fig. 5.1). Here, a single photon ionization step eliminates unwanted resonances and simplifies the photoelectron spectrum. Four-wave mixing is used to create VUV light (around 8 eV photon energy) to extend the range of molecules studied. Using a tunable laser source for the excitation step also increases the amount of information available, as different vibrational states can be selected in the intermediate excited state. In particular, the excited state photoelectron spectra of NO and pyrazine are discussed in ref. [59].

The introduction of an XUV photon source to the field of excited state photoelectron spectroscopy has still further reaching applications. Again, multiple ion states are accessible with an XUV source, unlike multi-photon and VUV ionization steps, and both electronic and vibrational transitions can be probed between excited neutral states and ion states. Excited state photoelectron spectroscopy, specifically with an XUV light source, provides a link between the molecular orbital picture of a simple molecule and the electronic transitions observed in an experiment. The most important implication lies in the possibility of core-level photoelectron spectroscopy of molecules. While vibrational overlap and forbidden electronic transitions have been studied for some molecular systems, how a core-level electron distribution changes in an excited molecule is not well understood. Here we show the first attempts at experiments aiming to understand the valence level photoelectron spectrum of an excited bound state of Br_2, with the hope that this excitation-ionization scheme can be extended to core level spectroscopy in the near future.

5.2 Excitation scheme

The two-photon scheme used to excite and probe the B state of Br_2 is shown along with the potential energy curves of Br_2/Br_2^+ in Fig. 5.2. A pulsed green laser (doubled Nd:YLF @ 527 nm, $\geq$ 100 ns, 600 mW) is used to promote a population of Br_2 molecules into the B excited state. Approximately 50 ns later, the high-harmonic beam (17th) is then used to ionize the

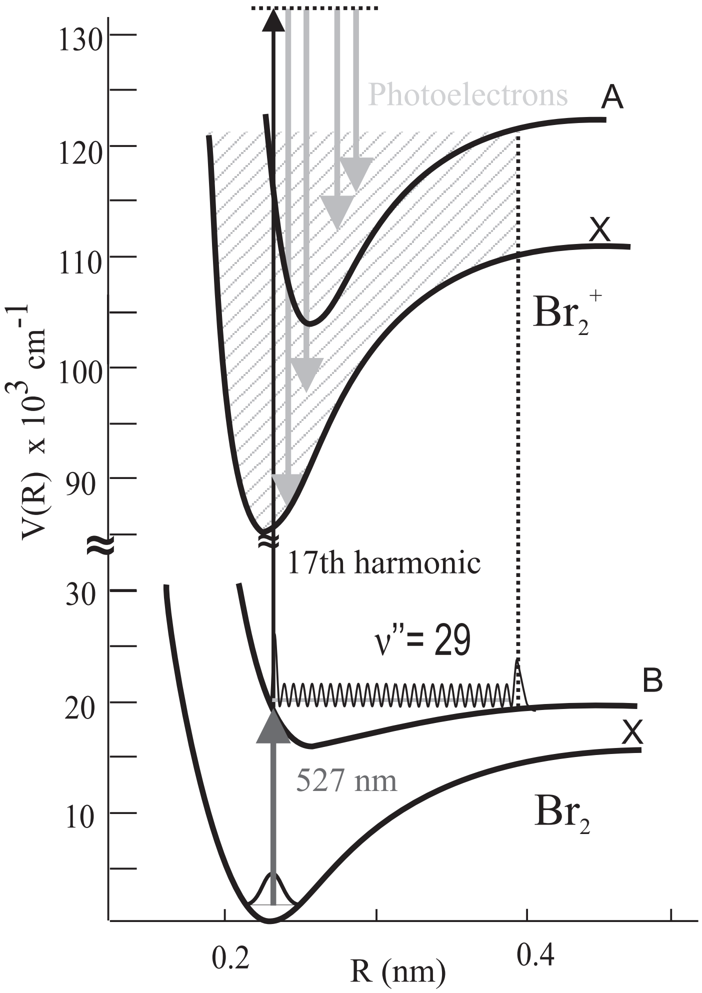

Figure 5.2: Potential energy curves for Br_2 and Br_2^+. Only the X and B states of the neutral and the X and A states of the ion are shown for simplicity. The 527 nm excitation laser pumps the netural into the $^3\Pi_{0+u}$ excited B state, and the 17th harmonic photoionizes the excited molecules. The v" = 26 vibrational level reached by the 527 nm photon is shown, creating a large region of Franck-Condon overlap in the Br_2^+ ion electronic states. The shading represents the accessible region of the X^+ and A^+ ion states with the probe photon. The intensities and energies of the photoelectrons will then be determined by the Frank-Condon overlap.

sample, creating photoelectrons from both the excited Br_2 molecules and the molecules left in the X ground state. The lifetime of the Br_2 B state at 527 nm is ~ 1 μs [60], therefore probing at a 50 ns delay with a $\geq$100 ns pulse should sample the excited state before complete predissociation. In this experiment, the intensities (and energies) of the photoelectrons generated from ionizing the excited state are determined by the maximum wavefunction overlap between the excited state and final ion state vibrational levels.

A calculation of the vibrational energy levels in the B state reveals that the narrowband Nd:YAG laser excites primarily the v' = 26 vibrational level of the B state (including the zero point energy of the ground X state). This calculation is given in equation 5.1.

$$E_{v"=0} + E_{h\nu} = T_e(X \Rightarrow B) - \Big(\omega_e(v' + 1/2) + \omega_e x_e(v' + 1/2)^2\Big) \tag{5.1}$$

In this equation, $E_{v"=0}$ denotes the energy of the zero vibrational level of the ground X state, $E_{h\nu}$ is the photon energy of 527 nm, $T_e(X \Rightarrow B)$ is the transition energy from v"=0 of the X state to v'=0 of the B state, and ω_e and $\omega_e x_e$ are the vibrational constants of the B state given in ref. [61]. Thus far we have ignored the Boltzmann distribution [1] of the ground X state of Br_2 at room temperature. The weights of the v" states in the X state of Br_2 calculated by the Boltzmann distribution (n_i/N, where n_i is the population of the ith energy level and N is the total population) are:

- v" = 0, weight = 0.54
- v" = 1, weight = 0.24
- v" = 2, weight = 0.11
- v" = 3, weight = 0.05
- v" = 4, weight = 0.02
- v" = 5, weight = 0.01.

Therefore, while the majority of the signal originates from v" = 0, v" = 1 and 2 cannot be discounted. The vibrational levels obtained in the B state originating from v" = 1 and 2 would then be v' = 33 and 39, respectively. Determining the vibrational level reached in the excited B state is important, since this will ultimately determine the extent of Franck-Condon overlap with the Br_2^+ ion states, and the energies of the ejected photoelectrons.

In a simple molecular orbital picture, the electron configurations (estimated) for the neutral and excited states of Br_2 and Br_2^+ are given in Fig. 5.3. From the ground neutral state, it is easy to reach the electron configuration of the ground and first two excited states of the ion, simply by removing an electron from the appropriate orbital. However, when starting from the electron configuration of the excited B state of the neutral, transitions into the ion configurations must involve the movement of 2 electrons, with the exception of the $B \Rightarrow X^+$ transition. This is the goal of excited state photoelectron spectroscopy, to link the understanding of a simple molecular orbital picture to the experimental observations of electronic transitions beyond ground state ionization spectroscopy.

5.3 Photoelectron spectra

The valence level photoelectron spectrum of Br_2 taken with the 17th harmonic of 800 nm is shown again in Figure 5.4. The three final electronic states of the molecular ion accessible with this photon energy are observed (labeled X, A and B). The solid lines in Fig. 5.4 indicate the known binding energies of the Br^+ atomic states [46]. In Fig. 5.5, the photoelectron spectrum of Br_2 with the introduction of the 527 nm excitation laser along with the 17th harmonic is expanded from the dotted box in Fig. 5.4 . The expansion of the photoelectron spectra is due to a flight tube retarding voltage ($\sim$ - 14 V) used to clearly observe small signals and obtain better energy resolution. The larger peaks labeled $X \Rightarrow X^+$ and $X \Rightarrow A^+$ are due to the ground state absorption of the 17th harmonic leaving the ion in the X and A states (10.5 and 13 eV binding energy, respectively). The new signal in the 527 nm + 17th harmonic spectrum at $\sim$8.5 eV results from the ionization of the Br_2 neutral in the excited B state, leaving the ion in the X

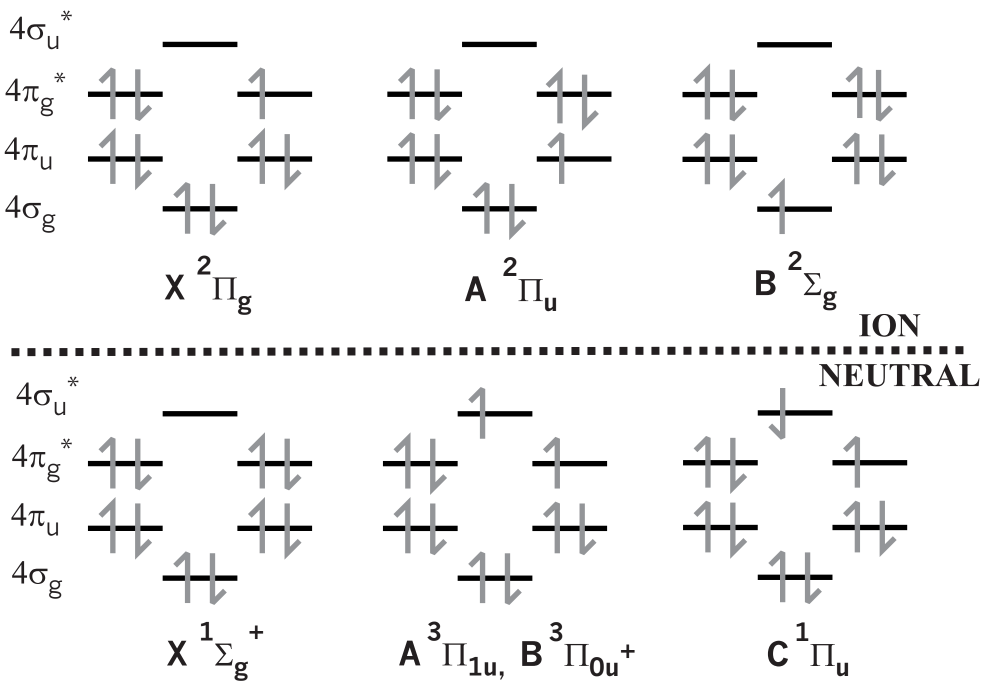

Figure 5.3: A molecular orbital diagram of the ground and excited states of Br_2 and Br_2^+. The four molecular orbital levels shown result from combinations of Br atomic p orbitals (outer valence shell). The B and A states of the neutral have a similar configuration but differ in orbital angular momentum.

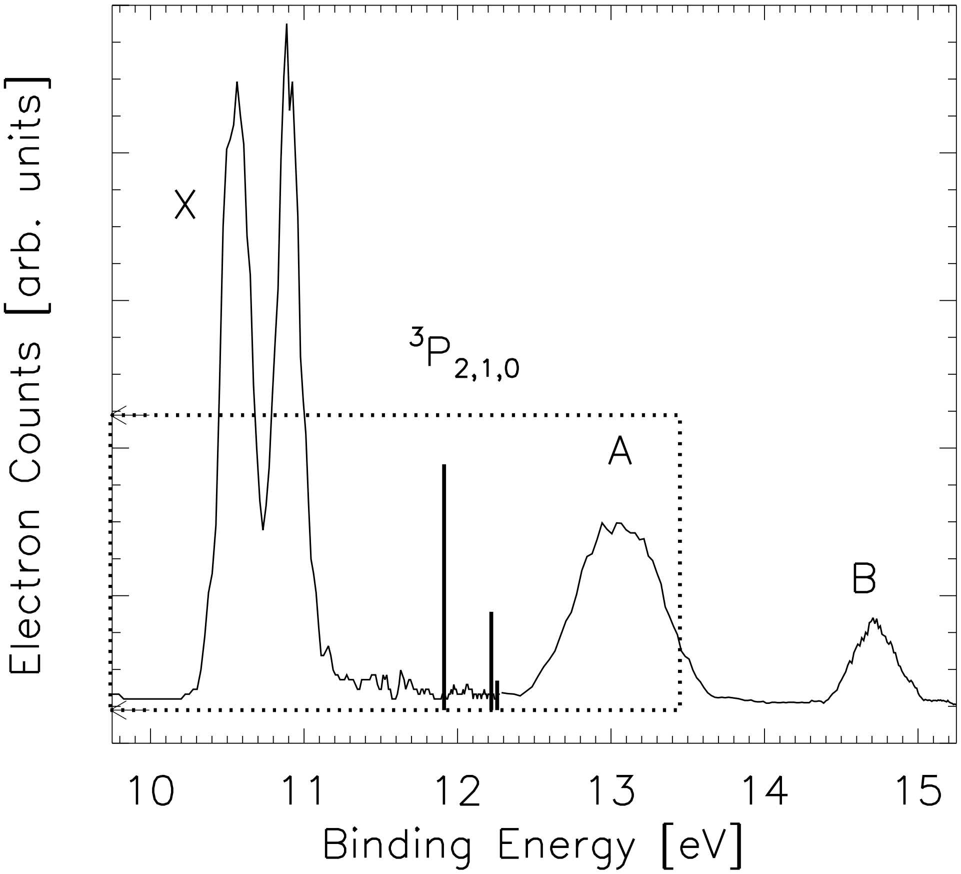

Figure 5.4: The photoelectron spectrum of gaseous Br_2 at 5 $\times 10^{-5}$ Torr taken with the 17th harmonic of 800 nm showing the final X, A and B states of the Br_2^+ ion. Solid black lines denoted $^3P_{2,1,0}$ are the known binding energies of the bare Br atom.

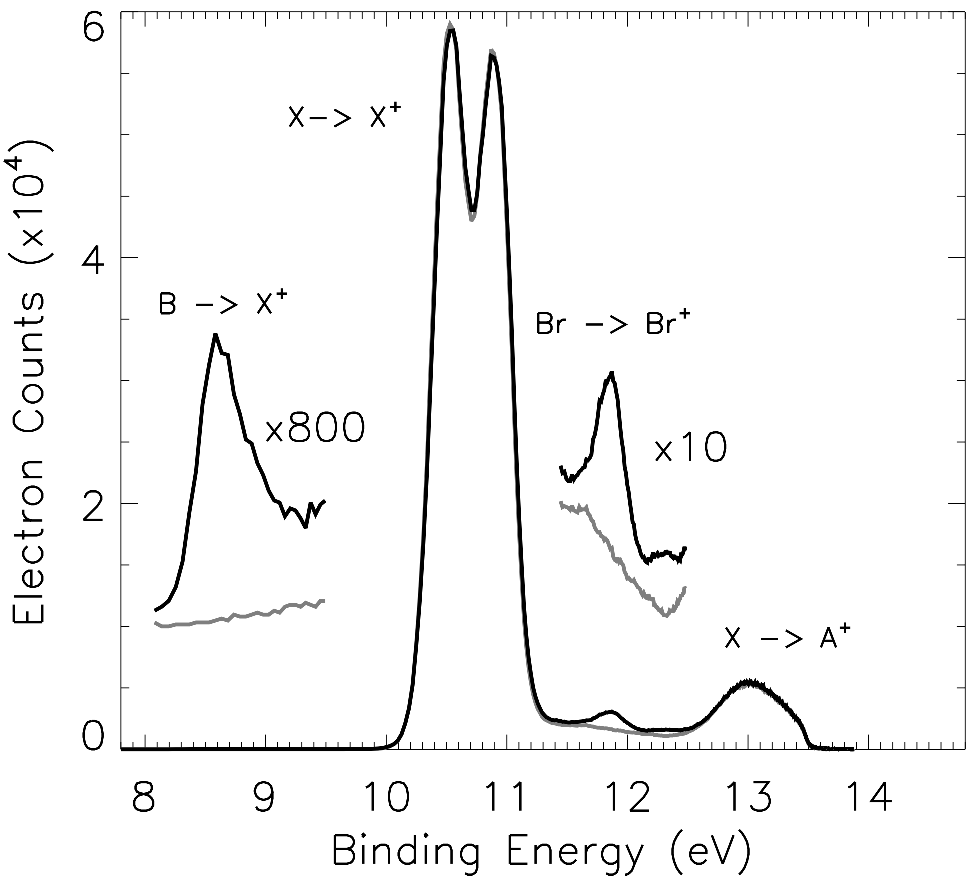

Figure 5.5: The photoelectron spectrum with the 17th harmonic only is shown in gray, while the photoelectron spectrum with the 527 nm + 17th harmonic is shown in black. Regions of small two-photon and atom signals are expanded for clarity.

ground state. The peaks at 11.8 and 12.2 eV are photoelectron signatures of the Br atoms. The B state of Br_2 is known to be predissociative [62], especially when excited to a high vibrational state, so the observation of Br atoms is not surprising. If the B⇒A^+ transition existed, the photoelectron peak would be expected to appear at 10.6 eV, and would be buried under the photoelectron peak from the X⇒X^+ transition. Similarly, the B⇒B^+ transition is expected to appear as a photoelectron peak at 12.3 eV, very close to the smaller Br atomic peak, but should be observable.

Figures 5.6 and 5.7 show the photoelectron spectrum of the B⇒X^+ transition expanded further by incrementally increasing the flight tube voltage. In both spectra, there are several interesting features. First, Fig. 5.6 demonstrates that the signal from the X⇒X^+ transition decreases as the B⇒X^+ signal increases. This is due to the depletion of ground state molecules as a population of the sample is pumped into the excited state. According to the absorption spectrum in appendix A, the cross section for absorption at 527 nm is 1.5×10^{-19} cm^2. Using the photon flux of the 527 nm (1.6×10^{15} photons/pulse, or 0.6 mJ/pulse), the percentage of molecules excited to the B state is $\sim 0.02\%$. A second point is that there is no visible photoelectron peak corresponding to the B⇒B^+ transition. If it were of similar magnitude to the X⇒X^+ photoelectron signal, it should be visible above the background. However, according to molecular orbital diagrams, it would require a 2 electron transition to go from the B neutral state to the B ionic state. One expects such transitions to be very weak.

Lastly, Fig. 5.7 demonstrates that ionization from the B (v'= 26) in the neutral leaves the ion in excited vibrational states of the ground electronic state. If the ground X state of Br_2^+ was left in the v" = 0 vibrational level after a two-photon resonant ionization, the photoelectron peak would be expected to appear at 8.15 eV binding energy (the energy of a 527 nm photon is 2.36 eV, and the 17th harmonic is 26.35 eV). However, in the experiment, the maximum of the B⇒X^+ photoelectron peak appears at 8.5 eV (corresponding to ∼v=8). This indicates that the Br_2^+ (X) state is vibrationally excited, most likely due to the Franck-Condon overlap resulting from the change in geometry from the excited Br_2 to the Br_2^+. Instead of a symmetric

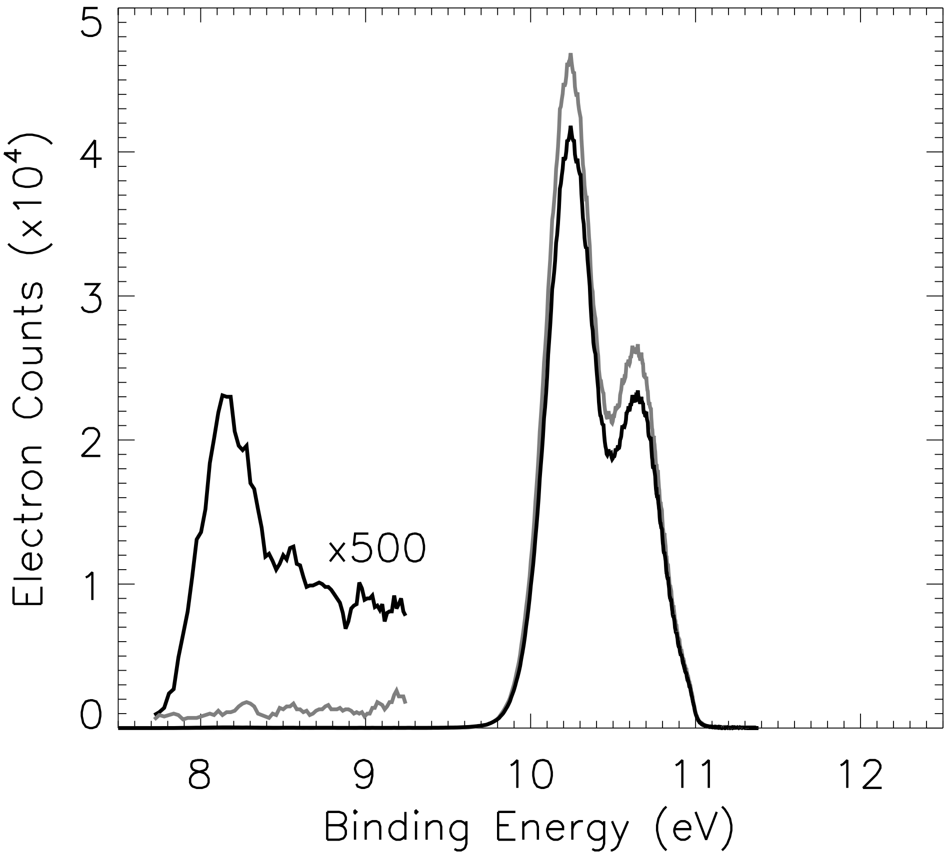

Figure 5.6: An expanded photoelectron spectrum of Br_2 with (black) and without (gray) the 527 nm excitation laser.

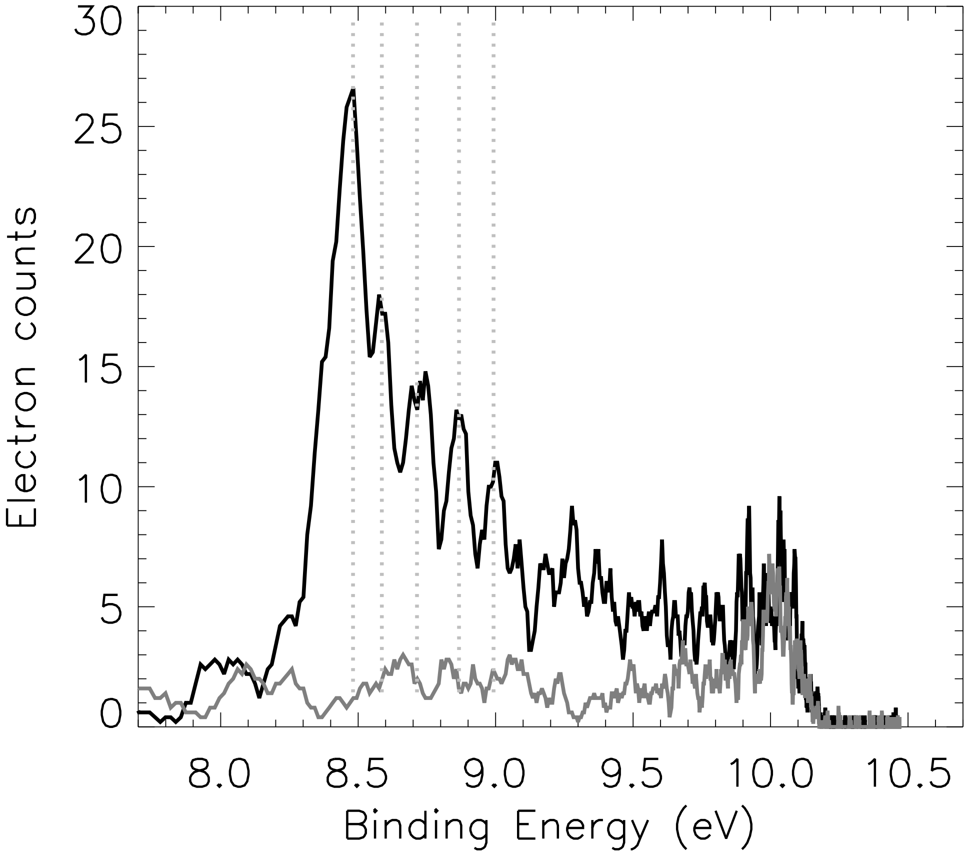

Figure 5.7: A further expanded photoelectron spectrum of the B⇒X^+ transition in Br_2 (gray line=17th harmonic only). The dotted gray lines mark the photoelectron energies of the peak heights.

peak, we also observe a long tail to higher binding energies, indicating even higher vibrational levels are excited (the multiple peak pattern is repeatable). The intensities of the vibrational peaks in Fig. 5.7 are likely due to Franck-Condon overlap between the neutral B state and the ionic X state vibrational levels. There is also the additional spin-orbit splitting of the Br_2^+ (X) state, which is $\sim$0.4 eV. This energy splitting does not agree with the adjacent peak splittings in Fig. 5.7, but it is the difference between the peaks at 8.5 and 8.9 eV, for instance. There is probably some combination of spin-orbit splitting and vibrational Franck-Condon overlap responsible for the pattern of peaks observed.

These are the most recent results presented in this thesis, and the interpretations are still preliminary. A more comprehensive evaluation of the results, including a theoretical Franck-Condon overlap simulation, will be required to fully understand the data. However, this proves to be a successful extension of the well documented REMPI technique, and will allow for the study of gas phase molecules not accessible with lower energy probe lasers. Experiments in the near future will likely include core-level photoelectron spectroscopy of the B state of Br_2, as well as low lying excited states of other simple molecules, such as IBr or I_2.

Chapter 6

Pulse durations of pump and probe beams: Cross-correlation measurements

6.1 Introduction

The alignment of the pump and probe beams, both spatially and temporally, is one of the most important factors for success in the time-resolved experiments. This task becomes especially difficult when the probe beam is in the soft x-ray region of the spectrum. Here I describe the method by which we successfully overlapped and obtained time-resolved photoelectron signals between the UV pump and soft x-ray beams when using the dual grating set-up for separation of the harmonics. Temporal pulse widths for the 400 and 266 nm pump beams as well as a number of harmonics are extracted from the cross-correlation measurements.

6.2 800 nm + 400 nm

The first step involves rotating both gratings to 0th order reflection of 800 nm and overlapping the 400 nm pump beam with the 800 nm beam in the interaction region. When the 400 nm pump beam is incident on a sample of Xe gas (I.P.=12.1 eV [45]), it takes a 4 photon process to ionize the $5p_{\frac{5}{2}}$ electron. When the 800 nm beam is introduced, provided the beams are overlapped spatially and temporally, a photoelectron peak at higher energy from a 4 + 1' ionization process is observed (4 photons 400 nm + 1 photon 800 nm). By maximizing the photoelectron counts in this peak, the overlap is optimized. This is also useful as an in-situ measurement of the cross-correlation between the 800 and 400 nm pulses. By moving the delay stage in 10 μm steps around the peak of the overlap, a series of points are obtained by calculating the area under the time-correlated photoelectron peak and plotting it as a function of pump-probe delay. Figure 6.1 is an example of a typical cross-correlation signal between the 400 nm and 800 nm pulses. The Gaussian fit to the data has a FWHM of 116±3 fs. Given the temporal width of the 800 nm pulse of 80±5 fs with the autocorrelator, the temporal width of the 400 nm pulse is calculated to be 84± 6 fs, assuming Gaussian pulse profiles.

6.3 800 nm + 266 nm

The specularly reflected 800 nm beam can also be overlapped with the 266 nm pump beam with Kr as a target gas. In this case, it takes four photons of 266 nm to ionize krypton (I.P=14.1 eV [45]). The three photon process, however, is very close to the ionization threshold, and when the 800 nm and 266 nm beams overlap spatially and temporally, photoelectron signals with electron kinetic energies corresponding to (3 + 1') (3 photons 266 + 1 photon 800 nm), (3 + 2') and (3 + 3') multiphoton processes are observed. Signals from the (3 + 2') and (3 + 3') multiphoton processes only are used to make the cross-correlation trace given in Fig. 6.2. The (3 + 1') multiphoton signal continues out to long times (pump-probe delays from 200 fs to 10 ps have been measured). This results from a Rydberg wavepacket excitation in Kr, where the three photon process (266 nm) excites a population into the high-lying Rydberg states leading up to the 5p ionization threshold. The 800 nm pulse then comes in at a later time and ionizes the evolving wavepacket, creating a long-lived signal. Some experiments were done to probe this wavepacket signal, which are outlined in Appendix 1. The cross-correlation signal between the 800 nm and 266 nm pulses has a FWHM of 157±4 fs, giving a 266 nm pulse width of 135±6 fs. Some broadening of the pulse is expected in the third harmonic generation, simply due to the group velocity spread of the wavelengths in the pulse as it passes through several lenses and harmonic generation crystals.

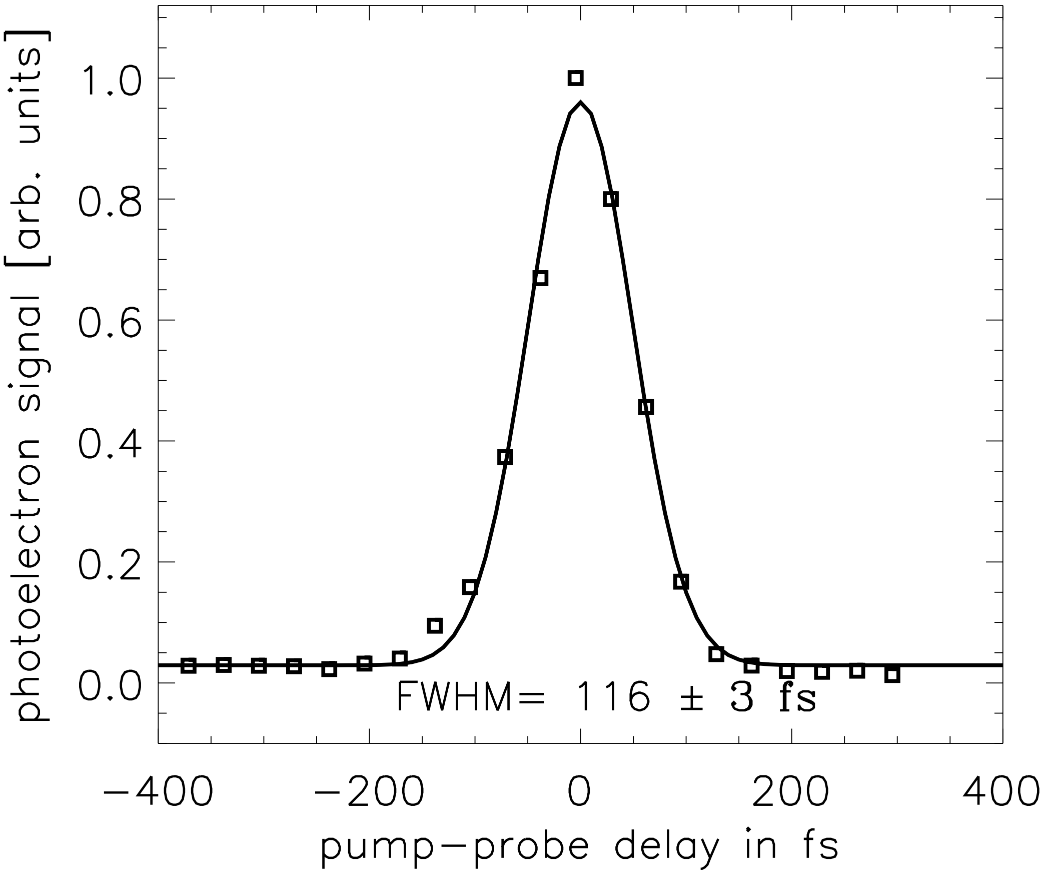

Figure 6.1: A cross-correlation trace of the 800 nm fundamental pulse with the 400 nm pump pulse obtained by a 4 (400 nm photon) + 1' (800 nm photon) multiphoton ionization in Xe.

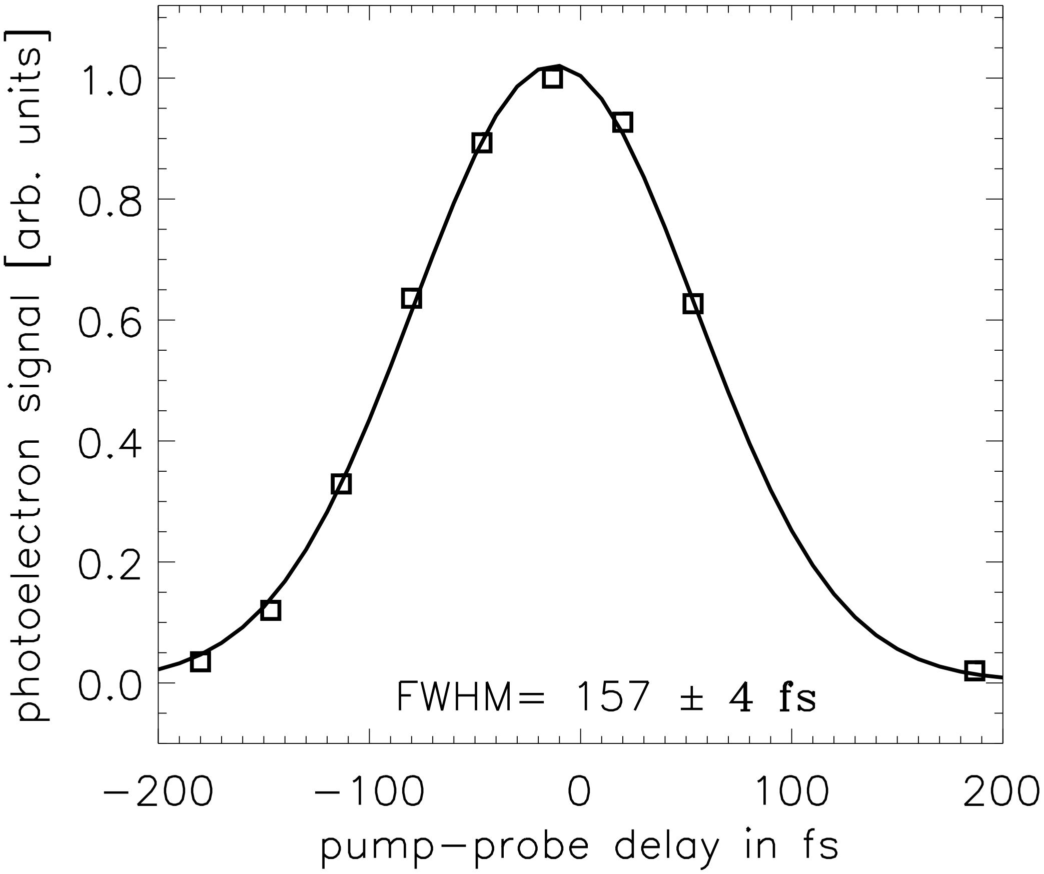

Figure 6.2: A cross-correlation trace of the 800 nm fundamental pulse with the 266 nm pump pulse obtained by a 3 (266 nm photon) + 2' or 3' (800 nm photon) multiphoton ionization in Kr.

6.4 17th harmonic + 800 nm

Once the 800 nm beam is properly aligned, the toroidal grating is rotated to the 17th harmonic, leaving the spherical grating at 0th order. An aperture which is on a translation feedthrough can be moved into the interaction region to ensure that the harmonic beam passes through the same point in space as the 800 nm beam. For the inital attempt at observing a harmonic-visible pump-probe signal, the full 20% of the 800 nm beam that is split off at the beam splitter is used as the pump beam (∼420 mW average power). With Kr as the sample gas, the 17th harmonic and the 800 nm beam are overlapped in the interaction region. When the pulses overlap at t=0, a time correlated signal is observed in the photoelectron spectrum. This signal is an above threshold ionization (ATI) process in which the 17th harmonic first ionizes the Kr sample and the 800 nm pump beam (or dressing beam) adds to or subtracts from the photoelectron energy to create sidebands in the photoelectron spectrum. This ATI process is well documented in the literature [54, 63]. An example of this photoelectron spectrum is shown in Fig. 6.3. With a negative flight tube voltage of ∼10 V, the main ionization peaks at photoelectron energies of 2.75 and 3.51 eV are seen in both the photoelectron spectra with the 17th harmonic only (solid line) and with the 17th harmonic + 800 nm dressing beam (dashed line). When the dashed line spectrum is expanded, three ATI processes are observed; the addition of one and two 800 nm photons and the subtraction of one 800 nm photon. These peaks increase and decrease as the 17th harmonic pulse and the 800 nm pulse are delayed in time with respect to each other and appear strongest at a delay time of t = 0, which is demonstrated in the next section.

6.5 Harmonics + 400 nm

As with the 800 nm beam, cross-correlation signals using Xe as the target gas are observed using the 400 nm pump beam. An example of a photoelectron spectrum with the 17th harmonic and the 400 nm beam overlapped in a sample of Xe is shown in Fig. 6.4(a), while

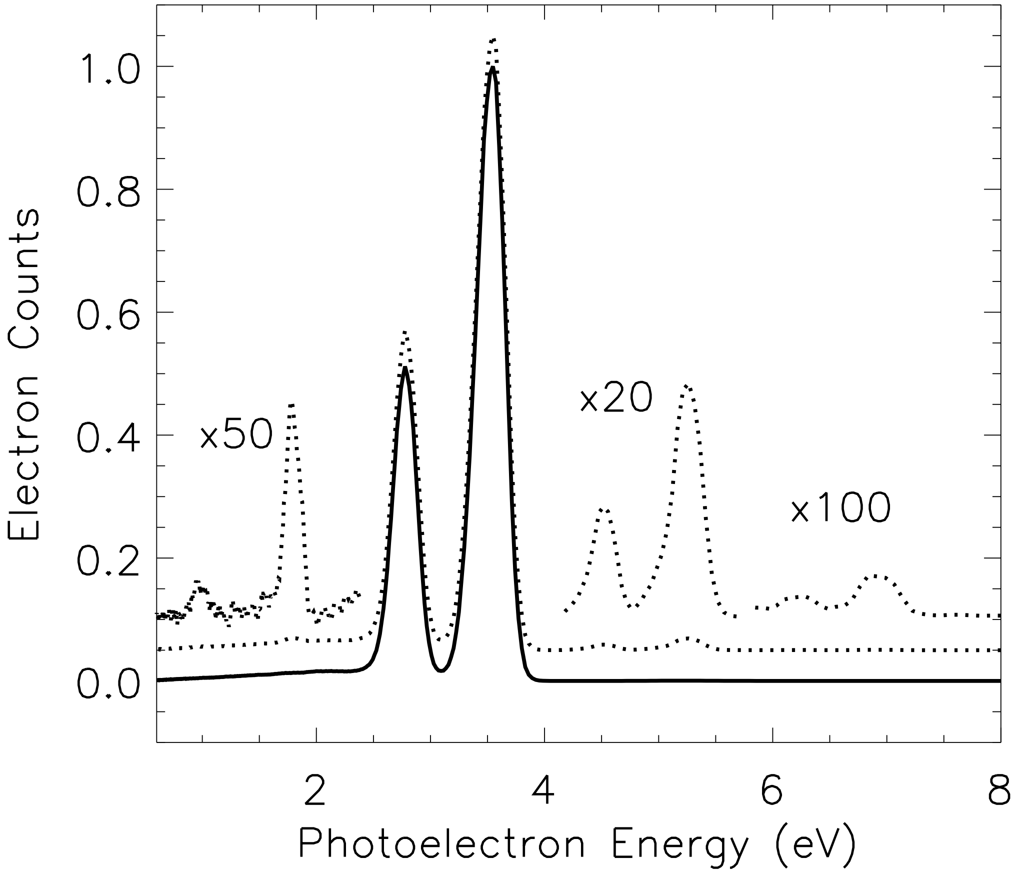

Figure 6.3: Solid line: photoelectron spectrum of Kr gas with the 17th harmonic, showing the spin-orbit split doublet of the Kr^{+} ion state. Dashed line: photoelectron spectrum of Kr gas when the 17th harmonic and an 800 nm dressing beam are overlapped spatially and temporally. The 800 nm dressing beam adds to or subracts from the 17th harmonic ionization in an above threshold ionization process.

Fig. 6.4(b) demonstrates the time-correlation of the sideband peaks as the harmonic pulse is swept across the 400 nm pulse by moving the delay stage. Here we demonstrate that even with a relatively weak 400 nm beam ($\sim$140 μJ per pulse), we are able to observe the ATI process. In this way, a cross-correlation trace due to the overlap of the 17th harmonic and the 400 nm pulses is obtained in a similar fashion as described above. The cross correlation signal with one grating rotated and the iris before the toroidal grating fully open (8 mm) has a FWHM of 888±100 fs, as is shown in Fig. 6.5(a). When the iris before the toroidal grating is reduced to 1 mm, the cross correlation trace in Fig. 6.5(b) is obtained, which has a FWHM of 441±65 fs. This is an indication that the grating produces a temporal stretching of the harmonic pulse, which we will call pulse front or phase front tilt. The more lines on the grating that are illuminated, the greater the stretching effect on the pulse due to each line delaying the pulse front by one wavelength [34].

There is another common stretching effect induced by using gratings with ultrafast pulses called group velocity dispersion (GVD). This is simply the diffraction-angle spreading by the grating of the range of wavelengths that make up the ultrafast pulse. It is not possible to compensate for both pulse front tilt and GVD stretching effects using two gratings, as the required geometry is different. In a typical stretcher/compressor design in most amplified ultrafast lasers, GVD is compensated by having two gratings effectively facing and parallel to each other so that the path-lengths of the different wavelengths will be equivalent. To compensate for pulse front tilt, the gratings must be in the configuration shown in Fig. 2.6, in order that the part of the beam that reflects from the far end of the first grating (with respect to the source) will be the first to hit the second grating, so that the paths of the different spatial sections of the beam will be equivalent. In this case, since the gratings are used at severe grazing angles, pulse front tilt is the dominant stretching effect.

In our case, the second grating is introduced to compensate for the pulse front tilt stretching effect. Although other frequency selection techniques are available such as deformable mirrors and multi-layer mirrors [29, 64], it is necessary in this experiment to have as clean

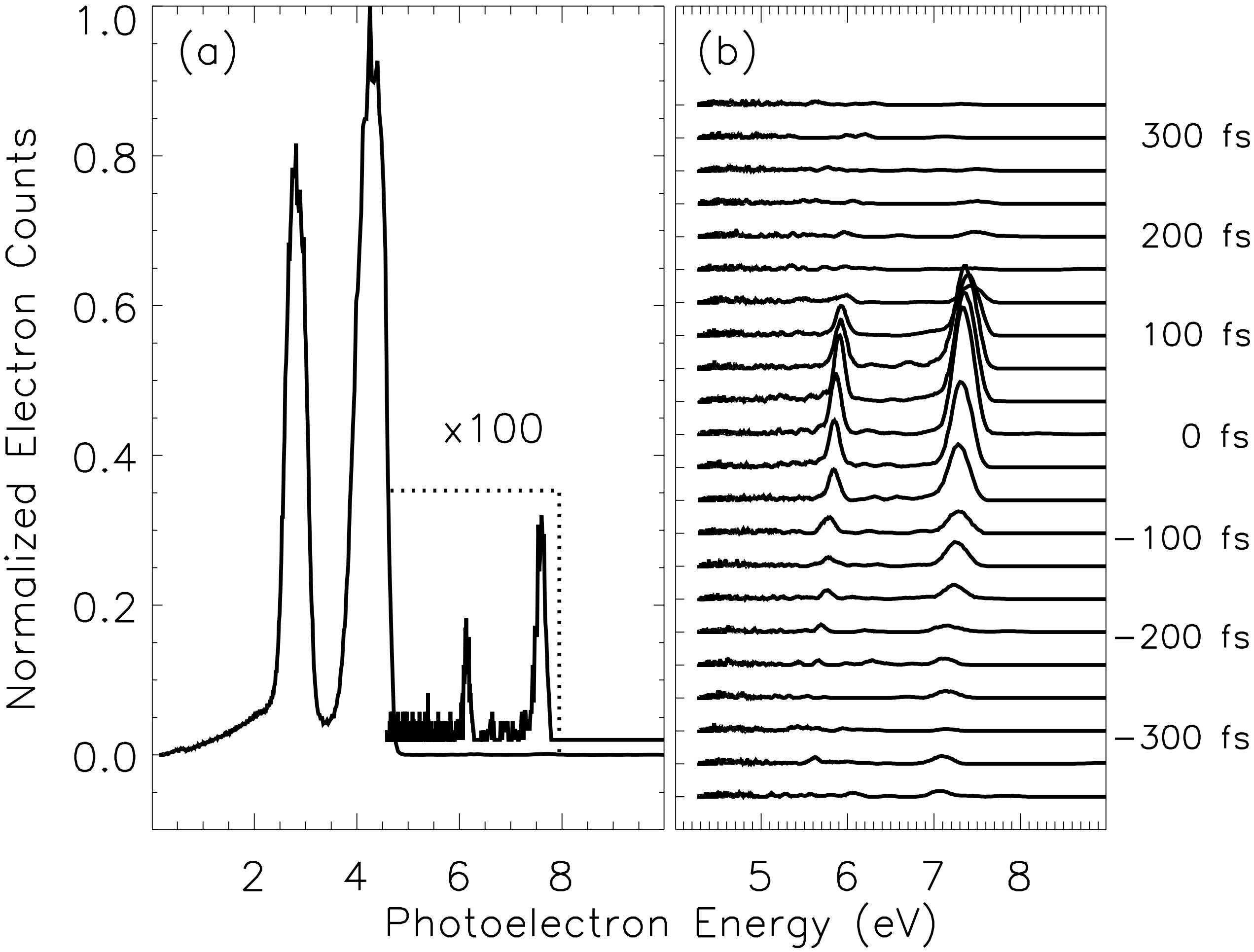

Figure 6.4: (a) A valence level photoelectron spectrum of Xe with the 17th harmonic showing the sidebands created by introduction of the 400 nm dressing pulse with spatial and temporal overlap. The sideband photoelectron peaks are exactly one 400 nm photon higher in energy than the main ionization peaks. (b) The time-correlation of the sideband photoelectron peaks.

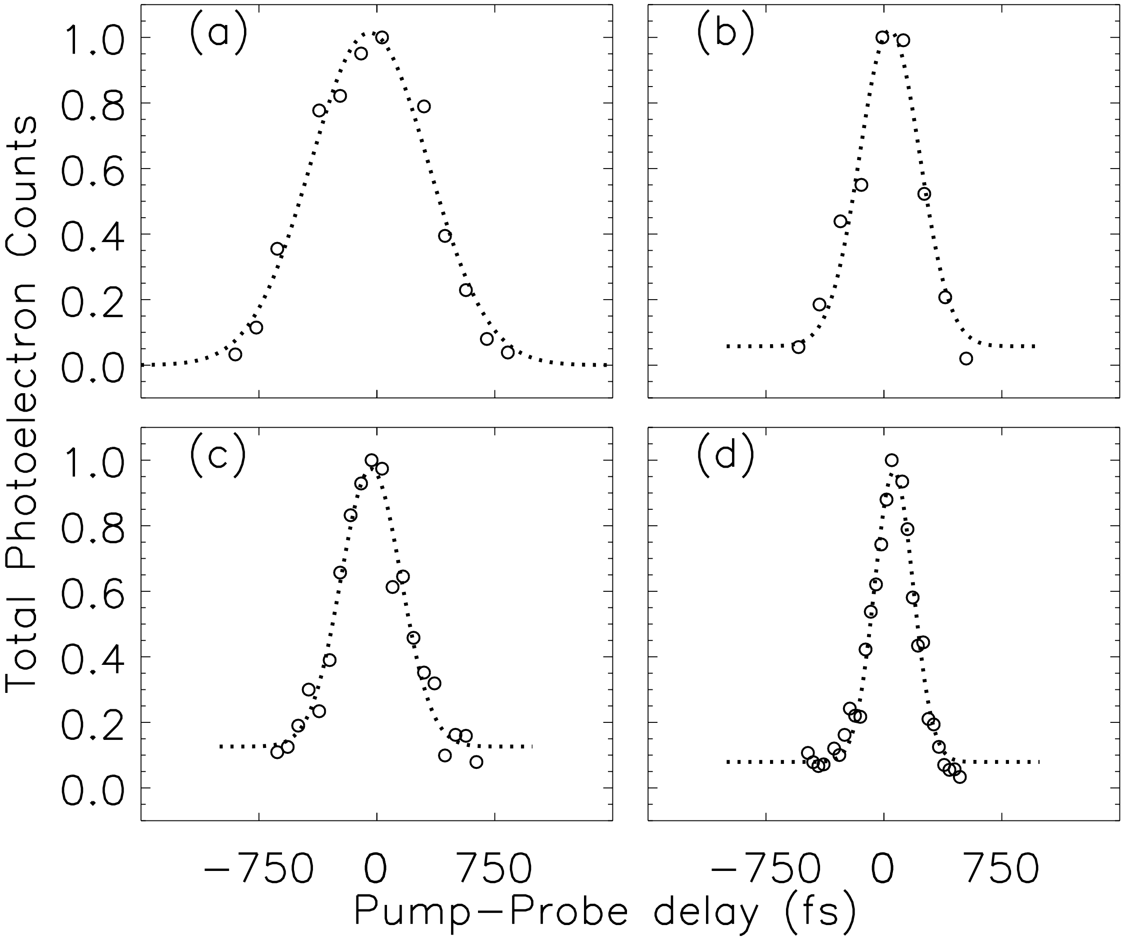

Figure 6.5: Cross-correlation traces of the 17th harmonic + 400 nm in Xe. (a) Toroidal grating rotated to 1st order diffraction, concave grating at 0th order reflection, iris open (8mm), FWHM = 882 ± 105 fs; (b) as (a) except iris at 1 mm, FWHM = 449 ± 64 fs; (c) Both toroidal and concave gratings rotated to 1st order diffraction, iris open (8mm), FWHM = 440 ± 25 fs; (d) as (c) with iris at 1mm, FWHM = 288 ± 12 fs.

a separation of the desired harmonic as possible. This is because pump-probe signatures are small signals (often $\leq 1\%$) above the background signal arising from ground state absorption and ionization of the harmonic. Even a small leakage of neighboring harmonics could mask the desired pump-probe signals. In addition, using gratings allows for a large range of accessible energies with relative ease of switching between harmonics.

When the spherical grating is rotated to 1st order diffraction and the iris before the second grating is 8 mm in diameter, a cross correlation between the 17th and 400 nm beams with a FWHM of 451±32 fs (Fig. 6.5(c)). Comparing this to the width with one grating rotated, an improvement of a factor of 2 in the width of the cross correlation is observed. Again, when reducing the iris to 1 mm, the cross correlation narrows as is shown in Fig. 6.5(d). Although some amount of linear chirp from the gratings is still present, there is still an improvement, with a FWHM of 288±12 fs. Using 84±6 fs as the temporal width of the 400 nm pulse, the shortest 17th harmonic pulse width is calculated to be 275±13 fs.

A ray tracing program was used to find the optimal distance between the two gratings for compression of the harmonic pulse. The distances from the ray tracing optimization are 18.2 cm from the focus in the jet to the center of the spherical grating, 80 cm from the center of the spherical grating to the center of the toroidal grating, and 93.1 cm from the center of the toroidal grating to the slit. The physical dimensions of the system were matched to these numbers with an accuracy of within 1 cm. According to the calculations, the compression would be best for the 21st harmonic for the current chamber dimensions. The distance between the two gratings as well as the number of lines illuminated on the gratings by the harmonic beam are critical parameters in the calculation of the compression. Experimentally, however, it was found that the 19th harmonic has the shortest pulse width. Figure 6.6 demonstrates the shortest soft x-ray pulse achieved to date with this apparatus, with a FWHM of 200±13 fs. Again, using the 84 fs pulse width of the 400 nm pulse, the FWHM of the soft x-ray pulse is calculated to be 182±14 fs. The widths of the neighboring harmonics become wider on either side of the 19th harmonic, with the 21st having a similar width as the 17th harmonic. The temporal widths of all the

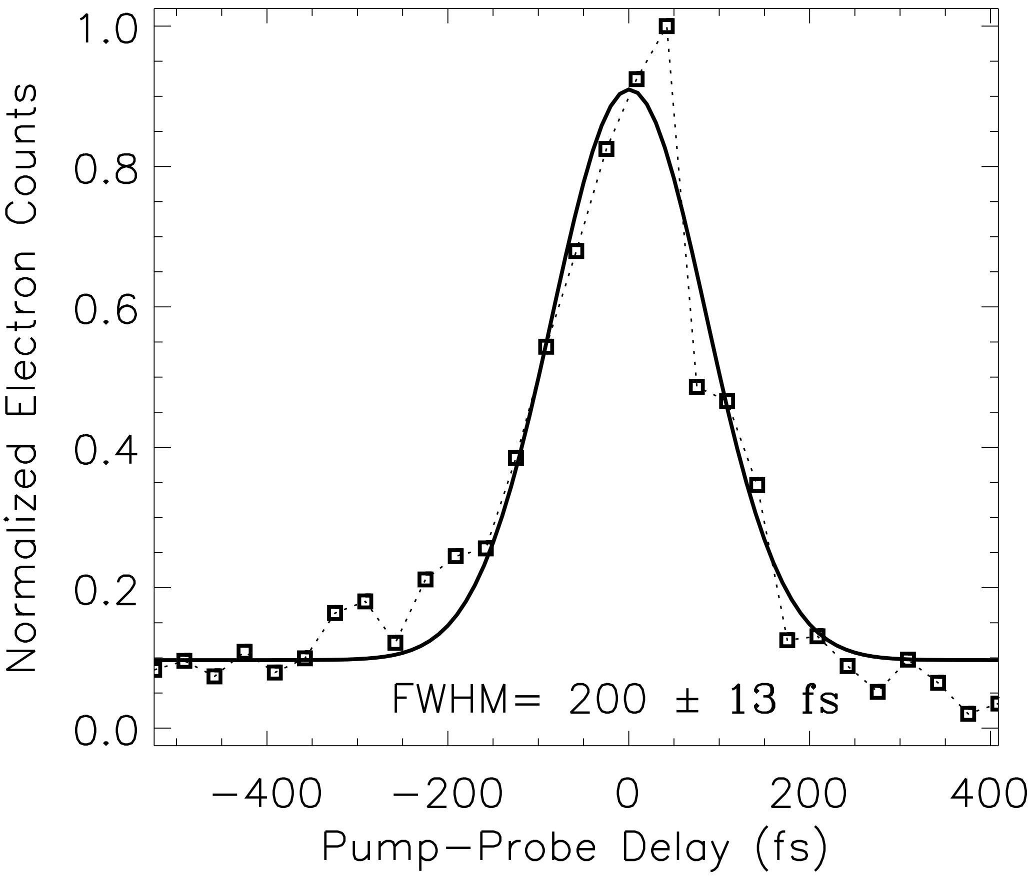

Figure 6.6: Cross-correlation trace of the 19th harmonic + 400 nm in Xe. The shortest soft x-ray pulse measured to date with the instrument described here. Some irregularity in the temporal profile may indicate an irregular spectral profile of the harmonic pulse.

harmonics measured are summarized in Fig. 6.7. It is important to note that the stretching effect of pulse front tilt goes as a function of λ^3, therefore the higher harmonics ($\sim$41st and above) are not expected to suffer from such a large temporal stretching effect, and only the toroidal grating should be required when using the higher harmonics for pump-probe experiments.

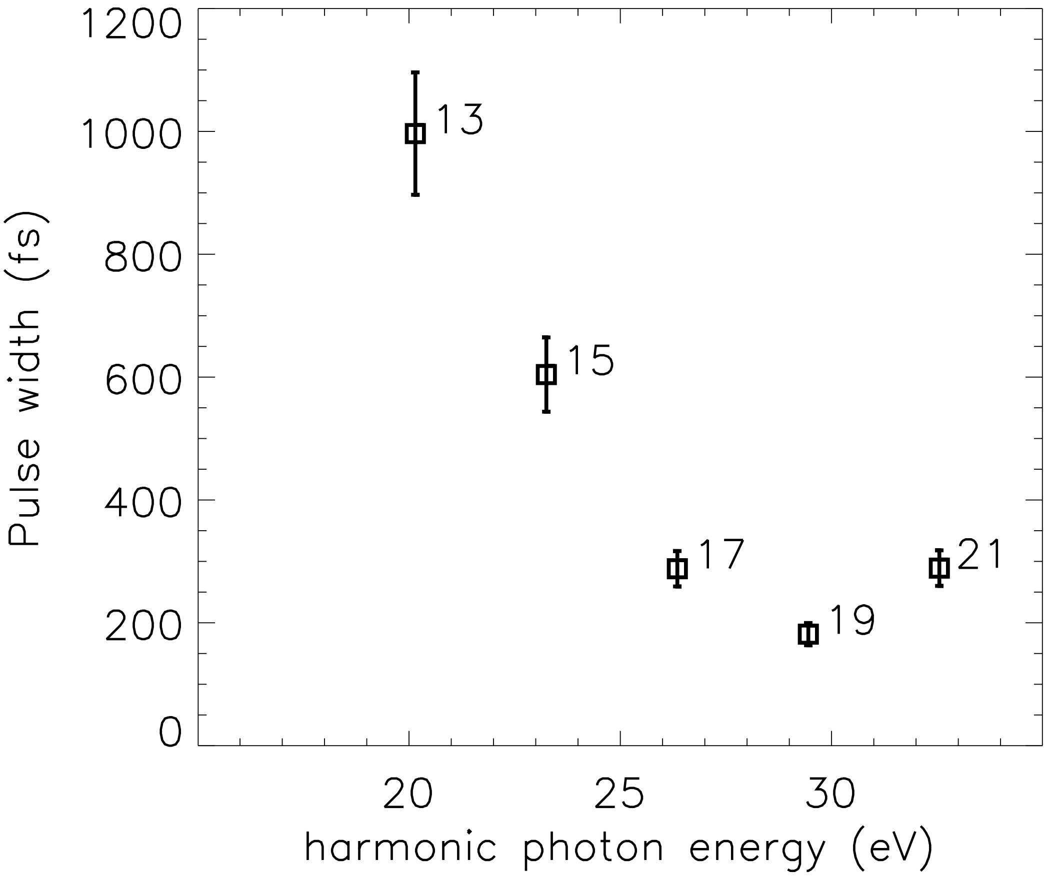

Figure 6.7: The pulse widths of the 13th through the 21st harmonics measured by cross-correlation with a 400 nm pulse. Error bars designate the error in the pulse width given by the Gaussian fitting program.

Chapter 7

Photodissociation of Bromine

7.1 Introduction

As a chemical bond is broken (or made), the electron distribution changes on an ultrafast time scale to accommodate the moving nuclei. To understand how this electron distribution changes with time is not only of fundamental interest but will also provide critical information on the specific chemical system and the dynamics of the ensuing reaction. In a simple system (Br_2), we observe a real time signature of a bond breaking in a gas phase molecule by measuring the kinetic energies of the ejected electrons as a function of pump-probe time delay. The changing electron distribution of the dissociating molecule is reflected in the binding energies of the electrons themselves and thus is detectable in its valence and core level soft x-ray photoelectron spectra.

Bromine was chosen as the initial sample for study for a number of reasons, the most important being that it is a simple system with a straightforward static photoelectron spectrum, and that it also has a relatively strong absorption cross-section at 400 nm (5×10^{-19} cm^2). The results presented here demonstrate that a number of complex issues exist even in a simple system, including above threshold cross-correlation features vs. transient signals, the onset of atomic photoelectron signals, multiple final ion states, and issues of atomic and transient state ionization cross-sections. Here I outline the details of the results for the photodissociation of Br_2 and discuss the analysis of the data and possible interpretations.

7.2 Pump-Probe Photoelectron Spectra in Br_2

The photodissociation scheme for probing the time-resolved dynamics of Br_2 is as follows:

$$\begin{aligned} Br_2(X^1\Sigma_g^+) &\xrightarrow{400nm} Br_2^*(C^1\Pi_u) \rightarrow 2Br(^2P_{\frac{3}{2}}) \\ Br_2 \text{ or } Br &\xrightarrow{47nm} Br_2^+(X,A,B) \text{ or } Br^+(^3P_{2,1,0}) + e^- . \end{aligned}$$

The 400 nm pump pulse excites the neutral Br_2 molecule to the $C^1\Pi_u$ dissociative state, and at time delays ranging from - 500 fs to + 1 ps the 17th harmonic probes the electron distribution by photoelectron spectroscopy. Figure 7.1 gives the potential energy curve diagram of Br_2/Br_2^+ taken from refs. [65] and [61]. This simplified diagram illustrates 4 different processes that are observed in the data presented here. These include: (1) the background signal from ground state ionization by the 17th harmonic, (2) the cross-correlation signals at t=0, (3) ionization of the excited state wavepacket before dissociation is complete, and (4) the ionization of the final Br atom products. These different processes are discussed in more detail below. The diagram shows only the X and C electronic states of neutral Br_2 and the X and A states of Br_2^+ for simplicity, since these are the important electronic states involved in the photodissociation and ionization processes in the pump-probe experiment.

Figure 7.2 expands three pump-probe spectra from the same dotted box in Fig. 5.4, corresponding to pump-probe delays of -500 fs, -100 fs, and +500 fs. In Fig. 7.2, the background between the molecular peaks increases due to saturation of the detector on the main peak in order to amplify the small pump-probe signal. The spectrum corresponding to $\Delta t = -500$ fs is the background signal that appears with the soft x-ray pulse coming before the 400 nm pump pulse. The signal in the Δt=-100 fs spectrum at 7.5 eV binding energy is indicative of a cross-correlation, by means of a two photon (400 nm + 17th harmonic pulses) ionization of the Br_2

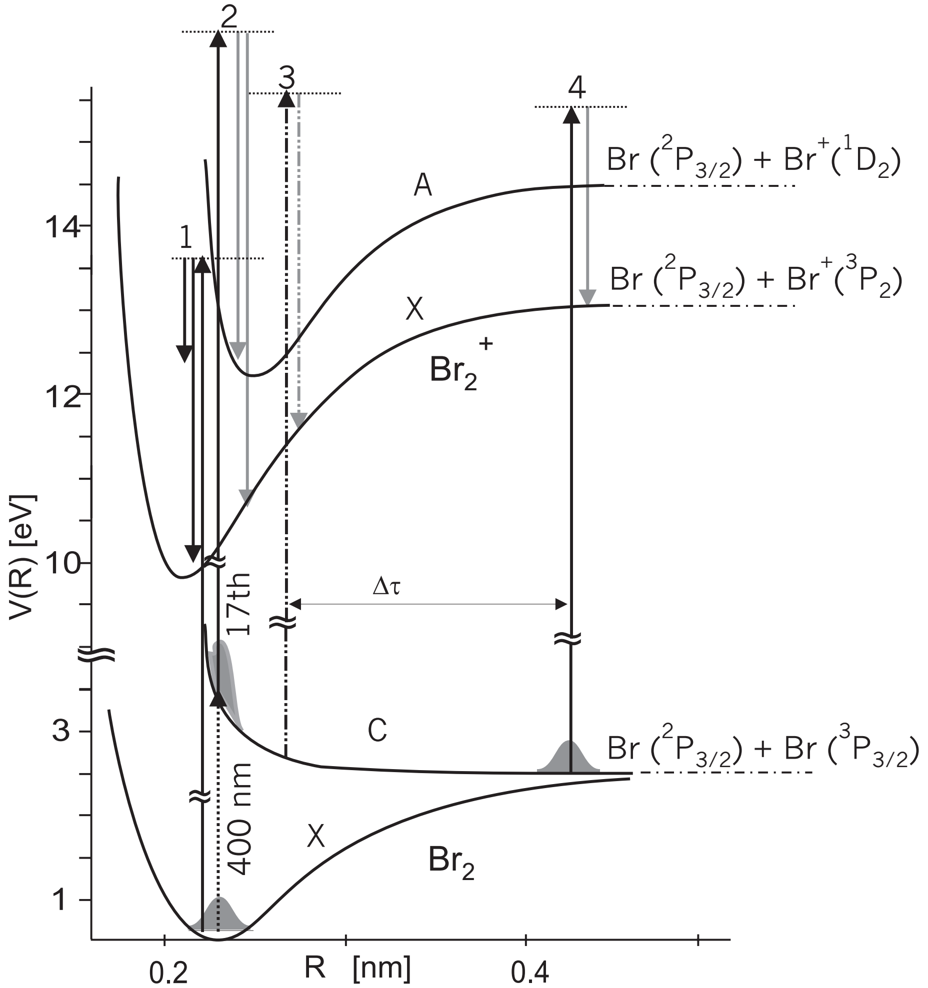

Figure 7.1: A simplified potential curve diagram illustrating the pump-probe sequence and resulting photoelectrons. **Process 1**: Ground state absorption of the 17th harmonic resulting in photoelectrons leaving Br_2^+ in both the X and A state (B ion state not shown). **Process 2**: Two photon ionization with the 400 nm + the 17th harmonic centered at t=0. **Process 3**: Ionization with the 17th harmonic from the excited C state of Br_2^* at a positive time delay (but before dissociation is complete). **Process 4**: After the dissociation is complete, the Br atoms are ionized by the 17th harmonic. The total energy of the probe laser is decreased for simplicity and size of the diagram.

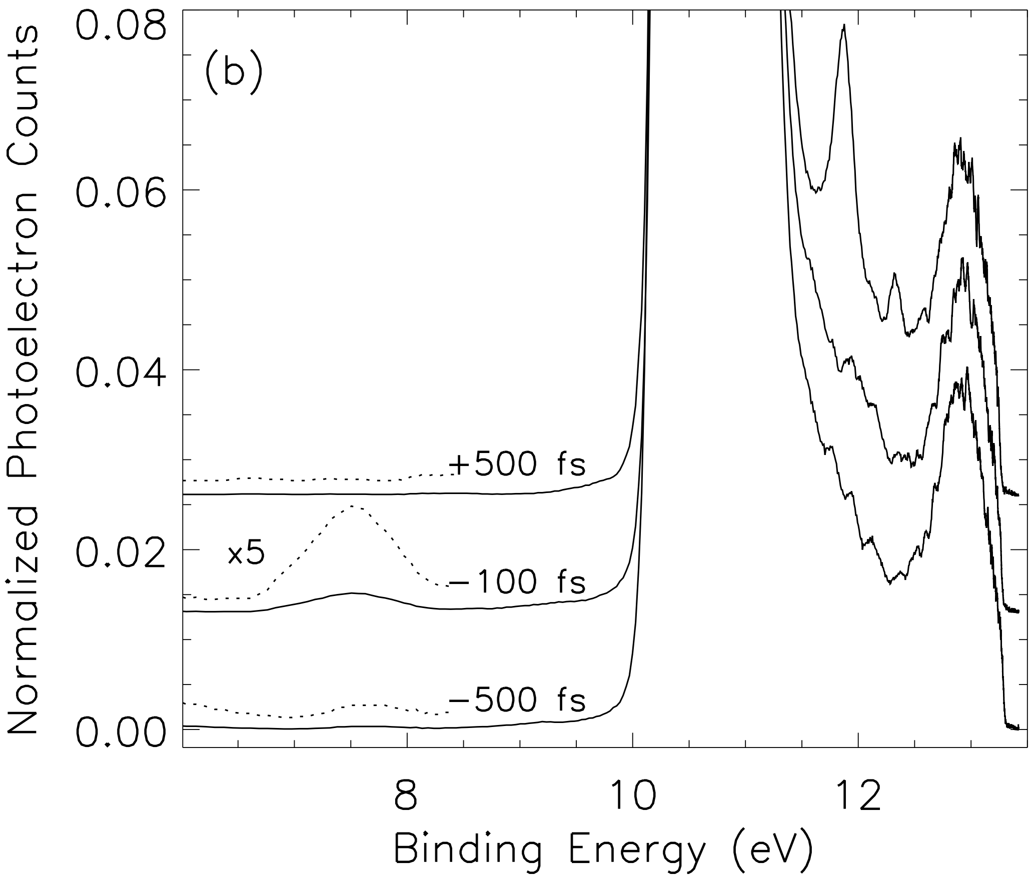

Figure 7.2: Three pump-probe spectra of Br_2: Δt=-500 fs (background), -100 fs (cross-correlation signal), and +500 fs (Br atom signal). The spectra are displaced vertically for clarity.

molecule. There are two processes which could result in a photoelectron signal at this energy. First, the 400 nm pulse promotes the wavepacket resonantly to the excited state and then the wavepacket is instantaneously ionized by the 17th harmonic. Second, a purely above threshold ionization process could also occur (similar to the case in Xe), where the 17th harmonic ionizes Br_2 and the 400 nm adds on to the ionization energy at t = 0. If the signal is due to the wave packet on the dissociative state, then the photoelectron spectra of the dissociative state is observed directly. Due to issues discussed later in this chapter, it is most likely a combination of the two processes. This cross-correlation feature is also useful as an internal determination of the temporal width of the soft x-ray pulse. The cross-correlation signal should be a doublet, mirroring the one-photon ionization molecular peak leading to the X state of Br_2^+, however, it appears at a photoelectron energy where the magnetic bottle resolution is less than the doublet separation. Cross-correlation features are also expected where the Br_2^+ is produced in the A and B states. The A state cross-correlation signal has been observed, appearing as a small shoulder on the low binding energy side of the X state background peak. Although the B state signal has not yet been observed, it is expected to be of a similar binding energy as the atomic signal, further complicating the spectrum. An expanded photoelectron spectrum highlighting the cross-correlation features is shown in Fig. 7.3. A signal in between the cross-correlations leading to the X state and the A state of the ion is attributed to the excited state wavepacket being ionized after sliding down the dissociative curve, which is discussed in more detail later in the chapter. Lastly, in the Δt=+500 fs spectrum, photoelectron peaks from the Br atom are observed at the expected binding energies while the cross-correlation signal is no longer present. This atomic signal persists at long time delays (Δt=100 ps) compared to the time scale of the dissociation dynamics (Δt <500 fs).

In Fig. 7.4, several photoelectron spectra are normalized and the background molecular signal is subtracted so that only the time-correlated signal remains. Figure 7.4 show a series of pump-probe spectra in the relevant energy ranges where the time-correlated peaks of the cross-correlation and atomic peaks appear. The small shift of the photoelectron spectra to lower

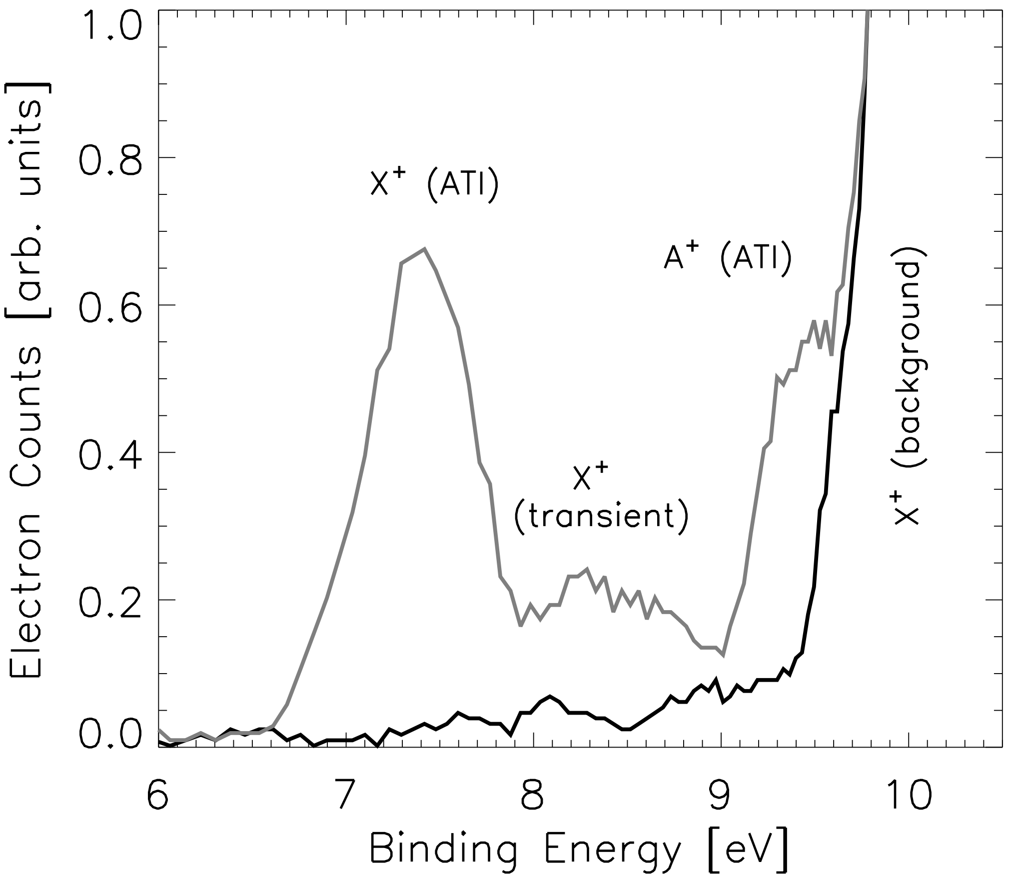

Figure 7.3: An expanded region of the photoelectron spectrum of Br_2 at Δt ~30 fs (gray line) and background at Δt ~-300 fs (black line) showing the cross-correlation features. The feature at 7.4 eV binding energy is the above threshold ionization resulting from the overlap of the 17th and 400 nm pulses where the Br_2^+ is left in the ground X state. The shoulder roughly centered at 9.4 eV is a similar signal, only the Br_2^+ is left in the excited A state. The signal at ~8.5 eV is attributed to the ionized excited state wavepacket as it is sliding down the dissociative curve.

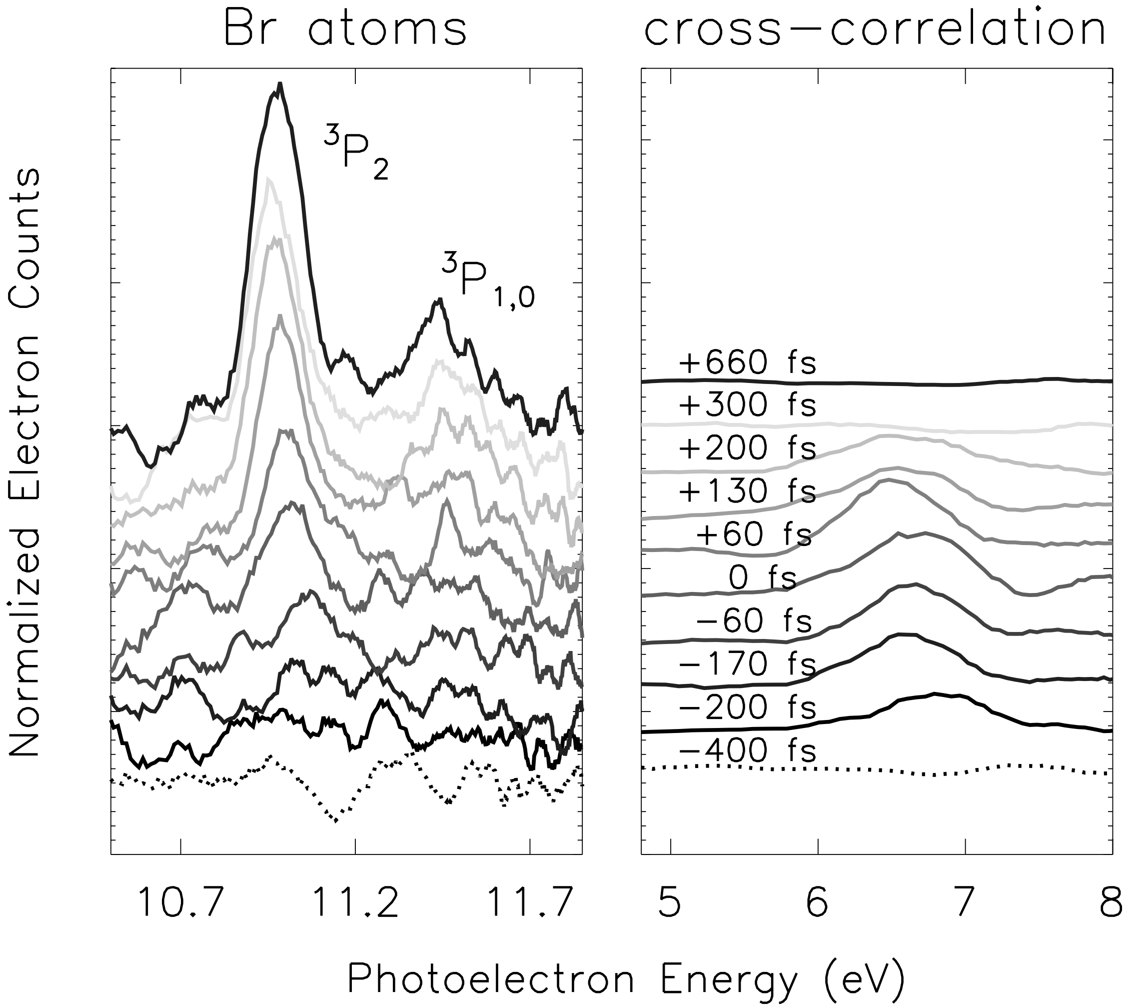

Figure 7.4: Normalized, subtracted pump-probe spectra of Br_2 in the cross-correlation time region (left). The spectra are displaced vertically for clarity. The panel on the right shows the appearance of the Br atom peaks in the photoelectron spectra. The two peaks in the photoelectron spectrum are due to spin-orbit coupling in the final Br^+ state. Numbers on the vertical scale are pump-probe delay in femtoseconds.

binding energies with increasing time delay is the result of a linear chirp in the soft x-ray pulse that is not compensated by the grating pair. From the data, it is clear that the atomic peaks rise very quickly, although their onset is delayed slightly with respect to the cross-correlation.

7.3 Time-traces of cross-correlation and Br atom signals

The delay between the center of the cross-correlation and the atomic rise is more clearly seen in Fig. 7.5 where the total photoelectron counts under both the cross-correlation peak and the atomic peaks are plotted vs. pump-probe delay. The solid line represents a Gaussian fit to the cross-correlation data points (filled circles) corresponding to the following equation:

$$S(t) = S_0 + A \times \exp\left[-4\ln 2\left(\frac{(t-t_0)}{\sigma_{fwhm}}\right)^2\right]. \tag{7.1}$$

S(t) is the total signal, S_0 is the y offset of the curve (or constant background signal), A is the peak height, t_0 is the time value of the peak of the curve, and σ_{fwhm} is the full width at half maximum of the Gaussian curve. The fit to the data gives a full width at half maximum of 300±14 fs and peak time t_0 = 0 ±14 fs. The dotted line is a fit to the rise of the total atomic signal (diamonds) with a smoothed step function given by the following equation:

$$S(t) = \frac{1}{2}erf\left(\frac{(t-\tau_{step})2\sqrt{\ln 2}}{\sigma_{fwhm}}\right) + \frac{1}{2}. \tag{7.2}$$

S(t) is the total signal, τ_{step} is the average time delay between a hypothetical instantaneous photon absorption and product atom formation, and σ_{fwhm} is the full width at half maximum of the above mentioned Gaussian [66]. The best fit to the data was found with $\sigma_{fwhm} = 250\pm13$ fs and $\tau_{step} = 40 \pm 13$fs. The discrepancy between the σ_{fwhm} values obtained from the Gaussian function and the step function could indicate that the atomic rise is less effected by the wings of the cross-correlation between the 400 nm and soft x-ray pulses, and the time resolution is determined by the middle part of the pulse, which would give a smaller value for σ_{fwhm}. However, the dashed line is the same step function fit to the atomic data, only with σ_{fwhm} fixed at the cross correlation value of 300 fs. The value of τ_{step} for the dashed curve is 37±13 fs, well within experimental error for the earlier value.

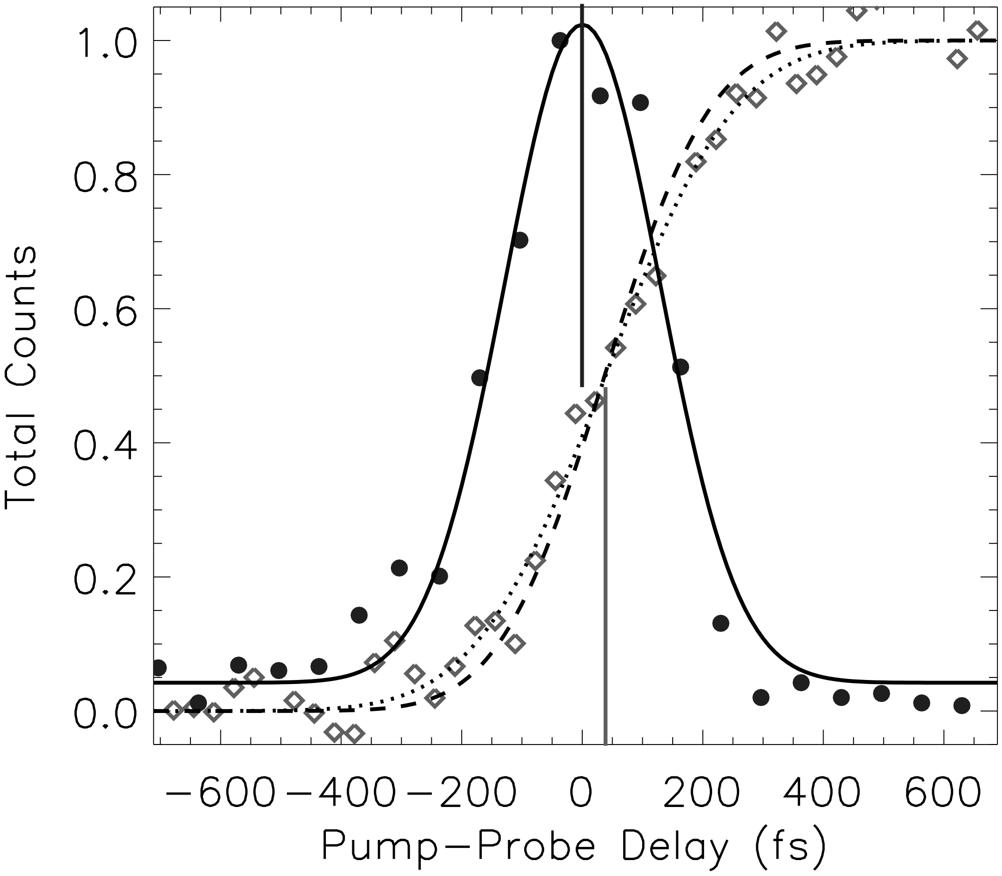

Figure 7.5: Total counts from the cross-correlation peak and the atomic peaks from Fig. 7.4 and additional time delay data not shown are plotted as a function of pump-probe delay between the 400 nm pump and the 17th harmonic probe. The cross correlation signal is fit with Gaussian function of width ∼300 fs and the atomic rise is fit with a step function described in the text. The dotted line fit of the step function allows both τ_{step} and σ_{fwhm} to be variables, while the dashed line fit fixes σ_{fwhm} to 300 fs. The solid lines designate the time delay between the center of the cross-correlation trace and the 'step' of the error function used to fit the rise in atomic signal.

A similar delay is seen when using the 19th harmonic as the probe, which has a shorter duration as discussed in chapter 6. The cross-correlation and atomic signals are about 50% weaker when using the 19th harmonic as the probe compared to the data taken with the 17th harmonic. The time traces for the 19th harmonic data set are shown in Fig. 7.6. In this data set, the cross-correlation is narrower, with a FWHM of 204±17 fs and t_0 of 0±17 fs resulting from the Gaussian fit. There is also a significant shoulder seen in the data at negative times. With a shorter soft x-ray pulse, some irregularities in the temporal profile could indicate structure in the spectral or spatial profile of the soft x-ray pulse, probably caused during the harmonic generation processes itself. The atomic data with the 19th harmonic is more scattered than in the case of the 17th harmonic due to decreased atomic signal. The shoulder of the cross-correlation peak also shifts the atomic curve. Atoms created at the peak of the local maximum (shoulder) will shift the τ_{step} to earlier times. While the parameters for the step function fit to the atomic data have large errors (τ_{step} = 36±21 fs and $\sigma_{fwhm} = 367 \pm 45$ fs), the trend remains same as in the 17th harmonic data. Again, the dashed line in Fig. 7.6 is from equation 7.2, except with the σ_{fwhm} held at 204 fs. The value of τ_{step} then becomes 30 ±20 fs.

This 40 fs delay of the onset of the atomic signal with respect to the center of the cross-correlation suggests a very fast dissociation time for the Br_2 molecule. A first order approximation of the dissociation time of Br_2 is accomplished by using a total energy equation and calculating the integral under the ${}^1\Pi_u$ dissociative curve. From Ref. [67], I use equation (9) as the estimate of the dissociative curve, derived based on experimental lifetime measurements and valid in the region 2.5 $\leq R \leq$3.5 $\mathring{A}$. The equation is as follows:

$$U(R) = U_{limit} + \left(\frac{1.594 \times 10^7}{R^{9.384}} cm^{-1}\right) \text{ (see Fig. 7.7(a)).} \tag{7.3}$$

where U(R) is the potential energy as a function of R, the internuclear distance, and U_{limit} is the atomic limit with respect to the ground state neutral well. The 9.384 power represents the steep repulsion of the dissociative curve. By generating a series of points along this curve, the integral under the curve is determined numerically. First, the integrand relating time of dissociation (t)

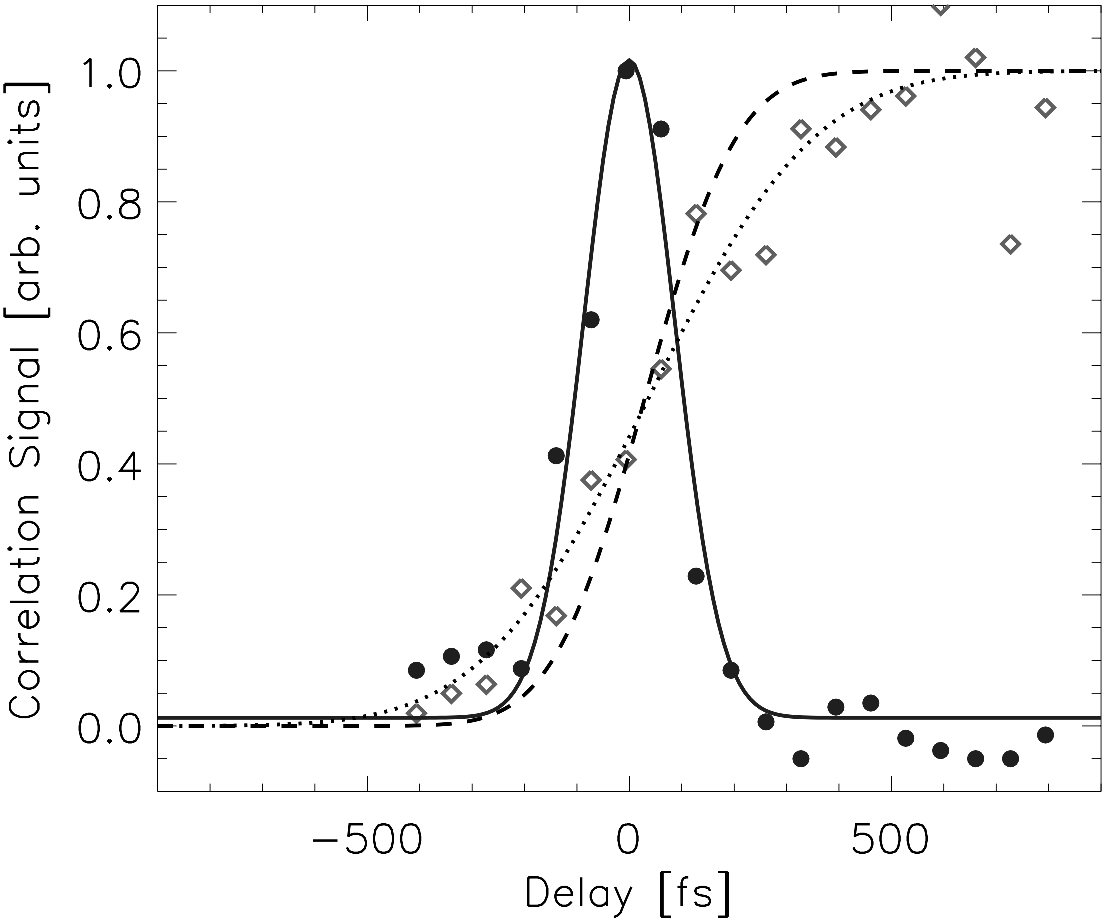

Figure 7.6: A similar plot as Fig. 7.5 except using the 19th harmonic as a probe. The cross-correlation signal has a FWHM of 204±17 fs and t_0 of 0±17 fs, and the fit to the atomic rise gives $\tau_{step} = 36 \pm 21$ fs and $\sigma_{fwhm} = 367 \pm 45$ fs (dotted line) and the dashed line is a fit holding σ_{fwhm} at 204 fs, and τ_{step} then becomes 30 ±20 fs.

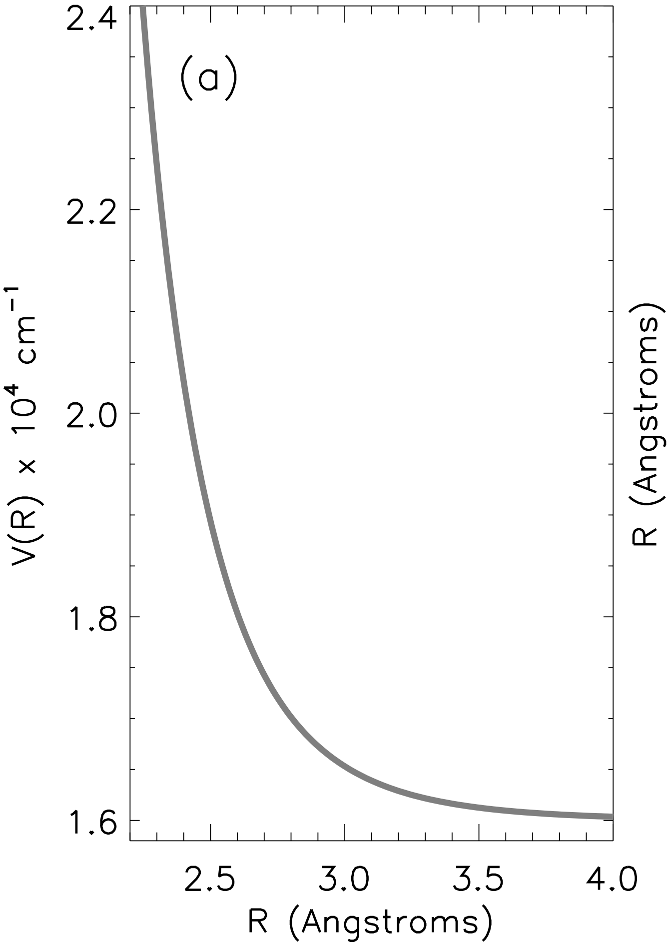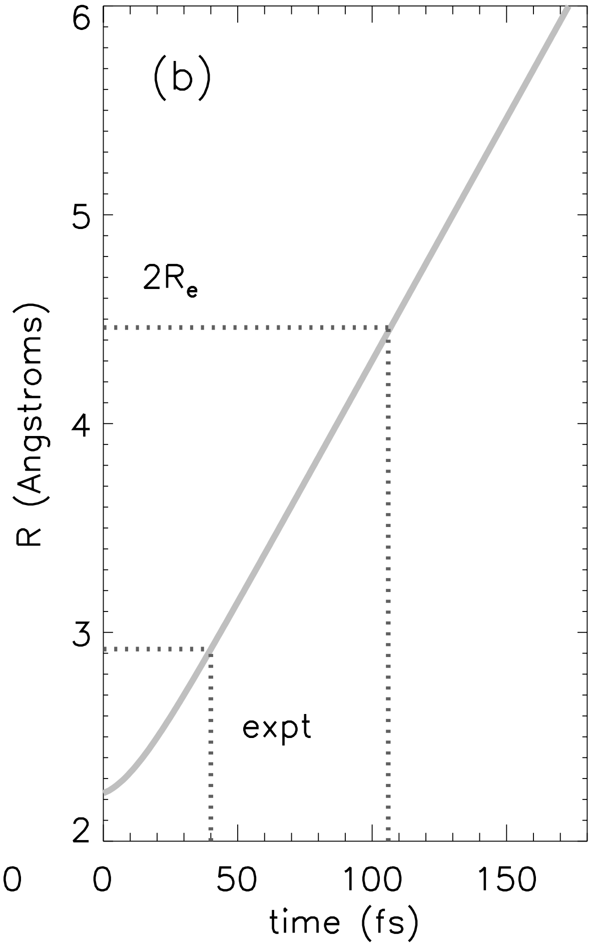

Figure 7.7: (a)The $C^1\Pi_u$ dissociate of neutral Br_2 given by equation 7.3 (b) A curve representing the integral of (a) in fs per $\mathring{A}$. The experimental result of 40 fs implies a bond distance of $\sim$ 3 Å, while a bond distance of 2R$_e$ occurs at a time of 105 fs.

to internuclear distance (R) is calculated from the following equations:

$$\begin{aligned} E_{total} &= E_{KE} + E_{PE} \\ E_{total} &= \tfrac{1}{2}\mu \left(\tfrac{R}{t}\right)^2 + U(R). \end{aligned}$$

Since t and R are the variables, I rearrange to solve for dt as a function of dR:

$$dt = \left(\sqrt{\frac{2}{\mu}(E_{total} - U(R))}\right)^{-1} dR \tag{7.4}$$

where E$_{total}$ (in Joules) is the total energy put into the system, E$_{KE}$ is the kinetic energy of the atoms with respect to the center of mass, E$_{PE}$ is the potential curve given by equation 7.3 (converted to Joules), and μ is the reduced mass of Br$_2$ in kg. Numerical integration of the above integrand results in the curve in Fig. 7.7(b), relating time and internuclear distance (after conversion to fs and $\mathring{A}$).

This calculation reveals that in 40 fs the Br-Br separation will have reached $\sim 3\mathring{A}$ from an initial equilibrium bond distance of $R_e = 2.23\mathring{A}$ in the ground state [65]. This elongated bond distance is in a regime where atomic behavior cannot be ruled out, but it is still closer to R_e than $2R_e$, a bond distance where it is safe to assume the bond is completely broken. Shortly after the two pulses begin to overlap, there is always some percentage of the soft x-ray probe pulse that follows the much shorter 400 nm pump pulse. With an estimated dissociation time of $\leq$40 fs, some signal due to atoms in the interaction region should appear at very early time delays. However, one might also expect a broad peak in the atomic region at early time delays, with signal coming from the dissociating wavepacket over several regions of the dissociative curve. Then at later time delays, the atomic peak should become narrower as the dissociation is nearly complete. The results presented in Fig 7.4 show no visible broadening of the atomic peak at early time delays. However, such a broadening of the signal could be wider than 1 eV considering the energy scale covered by the $^1\Pi_u$ curve. If this is the case, the broad signal might be impossible to detect above the background parent molecule signal level [see Fig. 7.2].

Another explanation of the observations is the possible existence of an ion-induced dipole potential curve that would almost mirror the neutral dissociative curve, except with a very shallow well. This could cause the photoelectron feature arising from the dissociating wavepacket to appear at a nearly constant energy. This could also account for the lack of shift of the atomic Br peaks that is observed. The discrepancy in the σ_{fwhm} values from the cross-correlation and the convoluted step function fit (especially in the data taken with the 19th harmonic) lends some validity to this idea. It is perhaps not complete to describe the dissociation dynamics as an instantaneous step function. The longer σ_{fwhm} from the step function fit of the 19th harmonic data (where the time resolution is the best) could indicate that another process is going on, creating a longer time delay than the width of the cross-correlation.

7.4 Ionization of the excited state wavepacket

The analysis of the dissociative state photoelectron spectra is complicated by multiple final states of the ion and multiple cross-correlation features. If the ion is left in the X state after ionization at a dissociative bond distance of $\sim$ 2.4 Å, a photoelectron peak between the two observed cross-correlation peaks (that leave the Br_2^+ in the X state and A state) is expected. The small peak in Fig. 7.3 at $\sim$ 8.5 eV binding energy could arise from the dissociating wavepacket. This signal rises and decays on the appropriate time scale for it to be a dissociative state photoelectron feature. This transient signal is analyzed more closely as demonstrated in Fig. 7.8. Four time traces are taken from the pump-probe photoelectron spectra with the 400 nm pump and 17th harmonic probe. The features are shifted in electron kinetic energy, but they are collected here on one pump-probe time trace. The black line is the cross-correlation leaving the Br_2^+ ion in the X state (corresponding to the signal from 6.5 to 8 eV binding energy in Fig. 7.3), the dotted line is the cross-correlation leaving the ion in the A state (9-9.5 eV), the medium gray line is the transient signal from 8-9 eV, and the light gray line is a random sampling of background signal from 5-6 eV binding energy. The transient signal clearly rises above the random noise trace and also has a similar Gaussian shape and width as the cross-correlation traces. This is consistent with what would be expected if the excited state wavepacket were ionized after moving out on the dissociative curve. As energy is deposited into kinetic energy of the atoms,

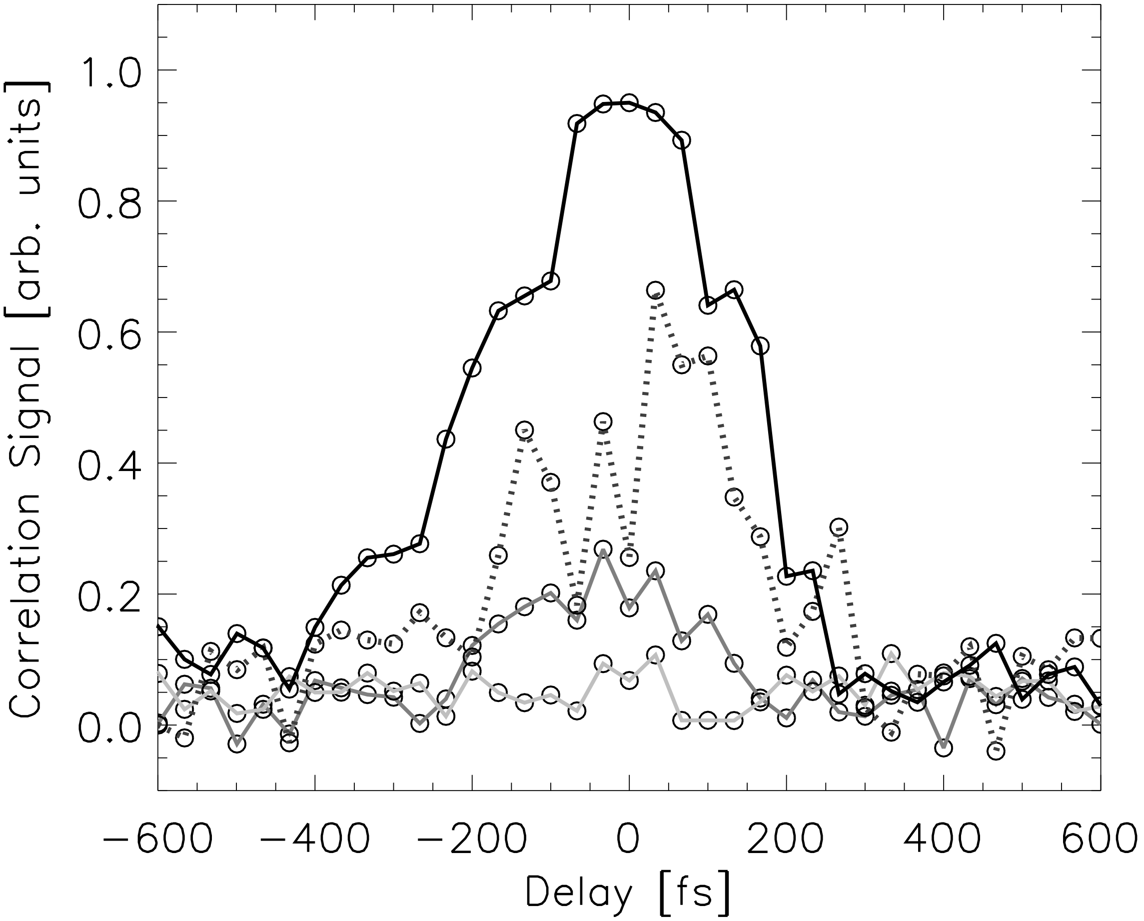

Figure 7.8: Time traces of the cross-correlation features in the Br_2 data (400 nm pump and 17th harmonic probe). Black line: signal from the ATI process leaving the Br_2^+ ion in the ground X state. Dark gray line: signal from the ATI process leaving the Br_2^+ ion in the excited A state. Medium gray line: transient signal from ionization of the excited state wavepacket. Light gray line: random background noise.

less energy is available to the electrons. Figure 7.9 shows similar time traces obtained using the 19th harmonic as a probe. Again, the transient time trace is observed to rise above the noise level with a similar shape as the cross-correlation features.

As mentioned earlier in the chapter, there are two competing two-photon processes; (1) ATI where the harmonic ionizes Br_2 followed by adding one 400 nm photon above the ionization threshold, and (2) the promotion of the excited state wavepacket by the 400 nm pulse followed by ionization with the harmonic. These are indistinguishable at t = 0, as the photoelectron possesses the same energy. If the excited wavepacket from process (2) slides out on the dissociative curve and is then ionized, however, the photoelectron peak will appear at a lower photoelectron energy. This is feasible if the wavepacket quickly falls down the steeply sloped section of the dissociative curve and then moves slowly in comparison when reaching the flatter section. The position of the transient photoelectron peak (Fig. 7.3) indicates that the wavepacket is ionized at an energy of $\sim$17000 cm^{-1} on the $^1\Pi_u$ curve. Looking at the shape of the curve in Fig. 7.7(a), it is reasonable to assume that the wavepacket quickly falls down the steep slope from 25000 cm^{-1} to 18000 cm^{-1}, and is then ionized from the flatter part of the curve.

Scans averaged over a larger number of laser pulses per time step were also taken of this transient signal from time delays of -33 fs to +165 fs with the 19th harmonic as a probe. The relevant part of the photoelectron spectrum for these time delays is shown in Fig. 7.10, as well as time traces for the ATI cross-correlations and transient state. These photoelectron spectra are plotted with photoelectron energy as the x axis instead of binding energy, as in Fig. 7.3. Again, it is clear that the transient signal (shaded region from 4.9 to 5.5 eV) rises above the random noise signal and has a structure similar to the cross-correlation features. From these time traces, as well as from Figs. 7.8 and 7.9, the peak of the transient signal is slightly delayed in time from the peak of the cross-correlation traces. This is also consistent with the wavepacket being ionized after it has moved out on the dissociative curve with a small time delay. However, this observed delay between the peak of the cross-correlation and the peak of the transient signal time trace is very small (10-20 fs) and it is difficult to be certain of such a small time delay with

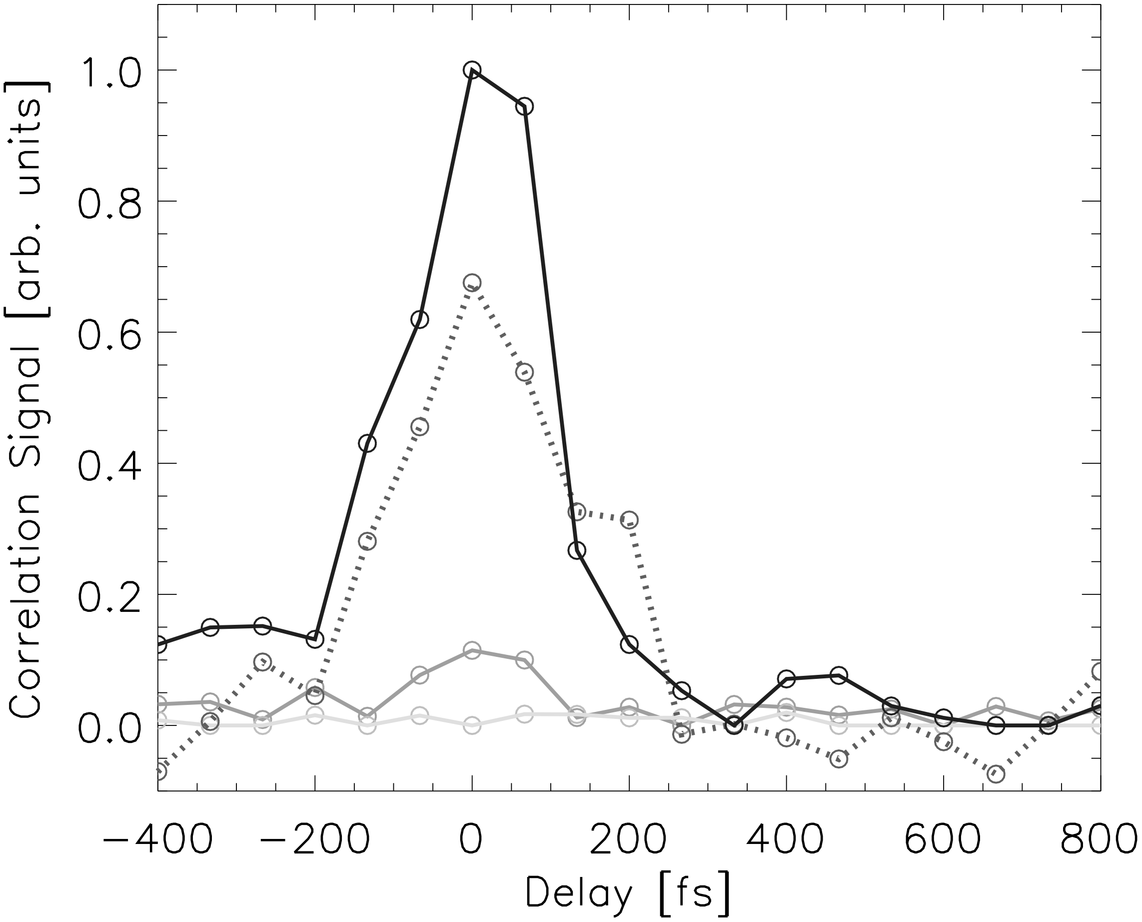

Figure 7.9: Time traces of the cross-correlation features in the Br_2 data (400 nm pump and 19th harmonic probe). Black line: signal from the ATI process leaving the Br_2^+ ion in the ground X state. Dark gray line: signal from the ATI process leaving the Br_2^+ ion in the excited A state. Medium gray line: transient signal from ionization of the excited state wavepacket. Light gray line: random background noise.

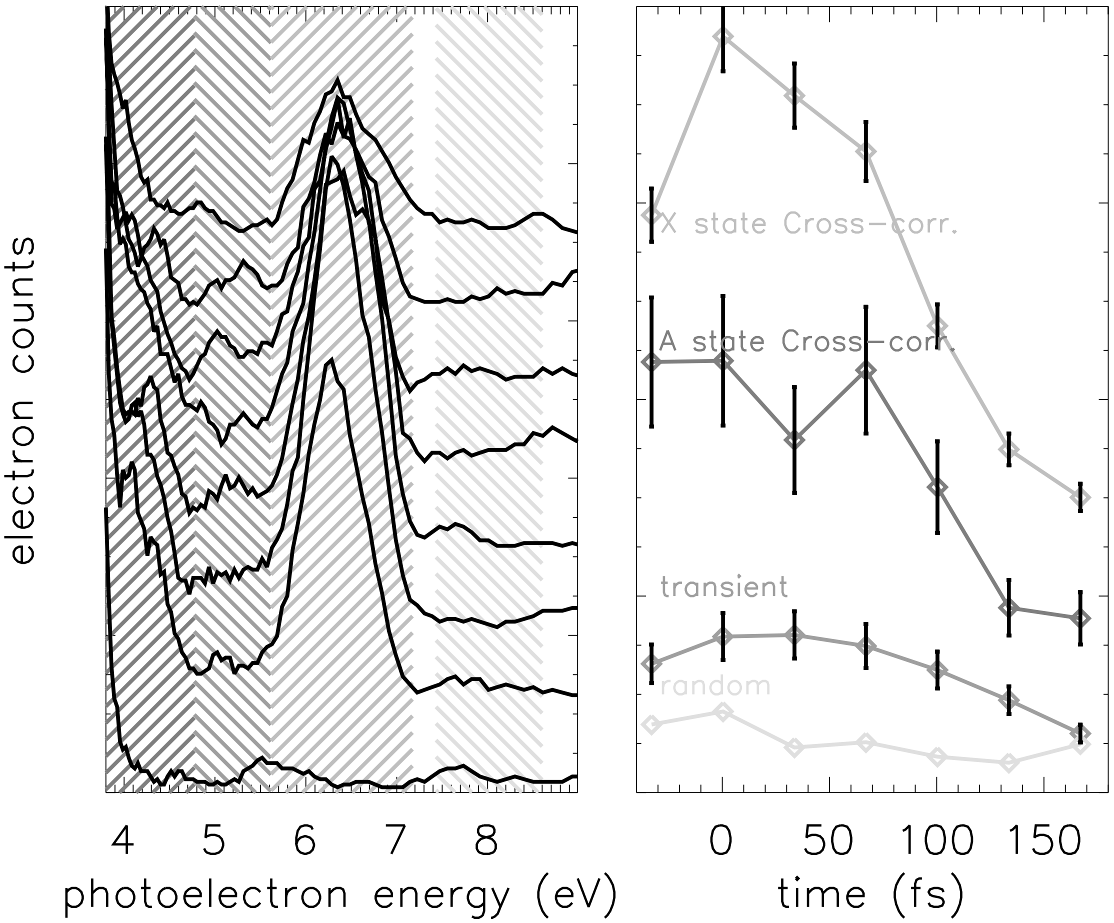

Figure 7.10: Long scans of the cross-correlation photoelectron energy region with the 19th harmonic as a probe. The shaded areas of the photoelectron spectra on the left correspond to the photoelectron energy regions giving rise to the time traces on the right. The photoelectron spectrum on the very bottom is a background, with no 400 nm pump beam, and from there the time delays step up from -33 fs to +165 fs in steps of 33 fs.

errors of ∼10 fs.

7.5 Ionization cross-sections of atoms and transient states

Another important result is the obvious difference in the ionization cross-section between the bromine molecule and the atom at the 47 nm probe wavelength. From the reported absorption cross-section of neutral Br_2 (5 x 10^{-19} cm^2) [6] and laser energy at 400 nm , an estimated 0.02% of the molecules in the interaction region reach the excited dissociative state, leaving the rest in the ground state, as is described in the following calculations:

Percentage of molecules excited from X→C state in Br_2

molecules in interaction region:

$$\begin{aligned}
\mathrm{N} &= 5 \times 10^{-5}\ \mathrm{Torr} \times 3.26 \times 10^{16}\ \mathrm{molecules/cm^3/Torr} \\
\mathrm{N} &= 1.6 \times 10^{12}\ \mathrm{molecules/cm^3}
\end{aligned}$$

flux of 400 nm light:

$$\begin{aligned}
\mathrm{E} &= \frac{\hbar c}{\lambda} \\
\mathrm{E} &= \frac{6.626 \times 10^{-34} J * s \times 3 \times 10^{10} cm/s}{400 \times 10^{-7cm}} \\
\mathrm{E} &= 5 \times 10^{-19}\ \mathrm{J/photon} \\
\text{photons in 150 } \mu\mathrm{J:} &= 3 \times 10^{14}\ \mathrm{photons}
\end{aligned}$$

absorption of Br_2 sample:

$$\begin{aligned}
\mathrm{A} &\cong \sigma N \ell \\
\mathrm{A} &= 5 \times 10^{-19}\ \mathrm{cm^2} \times 1.6 \times 10^{12}/\mathrm{cm^3} \times 1\ \mathrm{cm} \\
\mathrm{A} &= 8 \times 10^{-7} \\
\mathrm{A} \times \mathrm{flux} &= 8 \times 10^{7} \times 3 \times 10^{14}\ \mathrm{photons} \\
\mathrm{A} \times \mathrm{flux} &= 3.2 \times 10^{8}
\end{aligned}$$

$\%$ molecules in C excited state:

$$\frac{3.28 \times 10^{8}}{1.6 \times 10^{12}} \times 100 \quad = \quad \mathbf{0.02\%}$$

The counts in the atomic peaks are compared to the total counts in the A state molecular peak. Any decrease in the molecular A state signal due to the presence of the 400 nm pump beam is imperceptible, therefore it is estimated as being less than the noise level of the data (0.8% of the total A state signal-note, this number is not used in the calculation, but rather the 0.02% from above), while the atomic peak increases by $\sim$ 5% of that same A state signal. Note, the area under the peaks in Fig. 7.2 is not representative of the total counts used in the calculation, because the A state appears compressed on the energy scale. The A state signal is in turn $\sim$ 30% of the total signal originating from the ground state of neutral Br_2. From these numbers we can calculate the ratio of the atomic and molecular cross-section for the 17th harmonic in Br_2, as is shown in Table 7.1.

Table 7.1: A calculation of the enhancement of the atomic cross-section compared to the molecular cross-section for the 17th harmonic of 800 nm. Using 10,000 molecules as an arbitrary number, the raw photoelectron counts are used to calculate the ratio.

Br_2 X to Br_2^+ A		Br ^{2}P to Br^+ ^{3}P	
30%	of 10,000 mol.	0.02%	of 10,000 mol.
3,000	molecules	4	atoms
$43915 \pm 0.8\%^*$	counts	$2218 \pm 7\%^\dagger$	counts
$= 14.6^\ddagger$	counts/molecules	$= 554^\ddagger$	counts/atoms
	554/14.6	~ **40**	

*total counts in A state peak averaged over 10 identical scans
†total counts in atom peaks averaged over 5 identical scans at long delay times
‡similar to cross-section (σ), assuming path length is the same

The enhancement of the atomic signal compared to the molecular signal raises interesting questions about pump-probe spectroscopy with soft x-rays. If the cross-section of the Br atoms was not enhanced, the photoelectron signal would likely be imperceptible above the background noise. From the calculated estimate of the photodissociation yield, the 17th harmonic probe wavelength is $\sim$40 times more sensitive to the atoms than to the ground state molecule (taking into account the stoichiometric ratio of Br_2 to Br). One possibility is that the 17th harmonic accidentally overlaps with a resonance that enhances the atomic cross section. To attempt to fully understand this enhancement in cross-section, several different harmonics (13-21) were used in the same pump-probe experiment. A comparison of the resulting photoelectron spectra is given in Fig. 7.11. The spectra are normalized to the background signal on either side of the atomic peaks. It is clear from Fig. 7.11 that the atomic signal increases with decreasing harmonic number, as the energy of the probe approaches the threshold for ionization.

For the photoelectron spectra in Fig. 7.11, a similar calculation was done to determine the cross-section ratio for harmonics 13-21. A problem arises, however, when comparing data from the various harmonics. The flight tube voltage varies between data sets, causing the number of total counts in the molecular A state to change due to cutting off part of the photoelectron peak. This affects the outcome of the cross-section calculation since the atomic peaks are referenced to the molecular A state peak. To ensure that the calculation of the cross-section enhancement is correct, the ratios of the counts in the molecular A state peak to the counts in the molecular X state peak were determined for the pump-probe scans and then compared to the A/X ratio for a photoelectron scan where the A state was not at the edge of the energy cutoff. Assuming the X state peak is only slightly saturating the detector, which is the case since the spin-orbit doublet is still visible, comparing these two ratios gives a correction factor. The results of these calculations are given in Table 7.2. The final cross-section enhancement factors are plotted

Table 7.2: The corrections and final values for the enhancement of the atomic cross-section compared to the molecular cross-section for harmonics 13-21.

harmonic	$\sigma_{Br}/\sigma_{Br_2}$	error*	correction factor	final $\sigma_{Br}/\sigma_{Br_2}$
13	113.17	5.46	2.02	56.1
15	84.25	1.61	1.73	48.8
17	53.65	4.91	1.16	46.1
19	60.33	1.64	2.35	25.7
21	65.20	0.81	3.00	21.7

*based on the error from averaging several scans with identical detector and flight tube voltage settings, as well as the pressure of Br_2

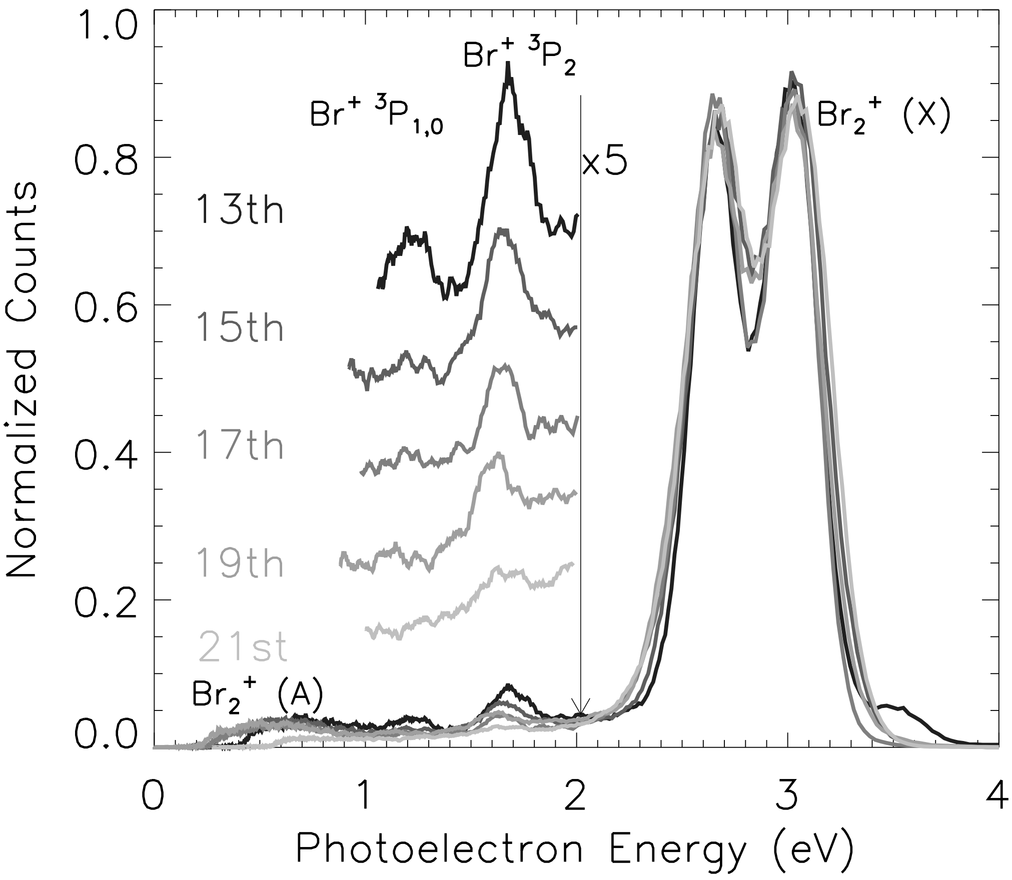

Figure 7.11: Photoelectron spectra of Br_2 at long time delays, after the atomic signal between 1 and 2 eV photoelectron energy has reached a maximum value. The atomic signal clearly increases as the harmonic number decreases. (The background signal in the vicinity of the atomic peaks is used for normalization.)

versus harmonic photon energy in Fig. 7.12. The trend in Fig. 7.12 is consistent with the trend observed in Fig. 7.11, further supporting the calculation of the cross-section enhancement. This figure also demonstrates that the 17th harmonic probe energy was not hitting a resonance in the ionization cross-section for Br, but that the cross-section is similarly enhanced for neighboring harmonics (although to varying degrees). It is also important to notice that even though the atomic signal is enhanced by a factor of $\sim$20 for the 21st harmonic, it is barely visible above the background noise.

An important scientific question is whether the cross-section of the dissociative molecular state is similarly enhanced. If not, a broad signal originating from the dissociative state of the molecule in the atomic photoionization energy region may be easily obscured. Similarly, cross-correlation features from the above threshold ionization process can mask photoelectron signals arising from transient states. For three different scans where the transient signal (discussed in section 7.4) was observed, the percentage of the total two-photon signal around t=0 of each type of signal (ATI signal leaving the Br_2^+ in the X and A states, as well as the transient signal from ionization of the excited state wavepacket) is calculated in Table 7.3. Interestingly, the fraction of transient signal does not change dramatically when going from the 17th to the 19th harmonic, while the atomic cross-section is reduced by a factor of 2 from the 17th to the 19th. This points to the possibility that the cross-sectional enhancements might be different for transient states than for the final atomic products. This type of information is crucial when attempting to measure the time dynamics of transient states.

Table 7.3: The percentages by total counts of the cross-correlation and transient photoelectron signals for three different scans and two probe wavelengths.

scan	Figure	% X ATI	% A ATI	% X transient*
17th + 400 nm	7.8	53.9	33.1	13.0
19th + 400 nm	7.9	56.6	34.7	8.6
19th + 400 nm	7.10	54.4	33.2	12.4

*%of the sum of X state and A state ATI signals and transient signal arising from the intermediate neutral excited state (or total two-photon molecular signal)

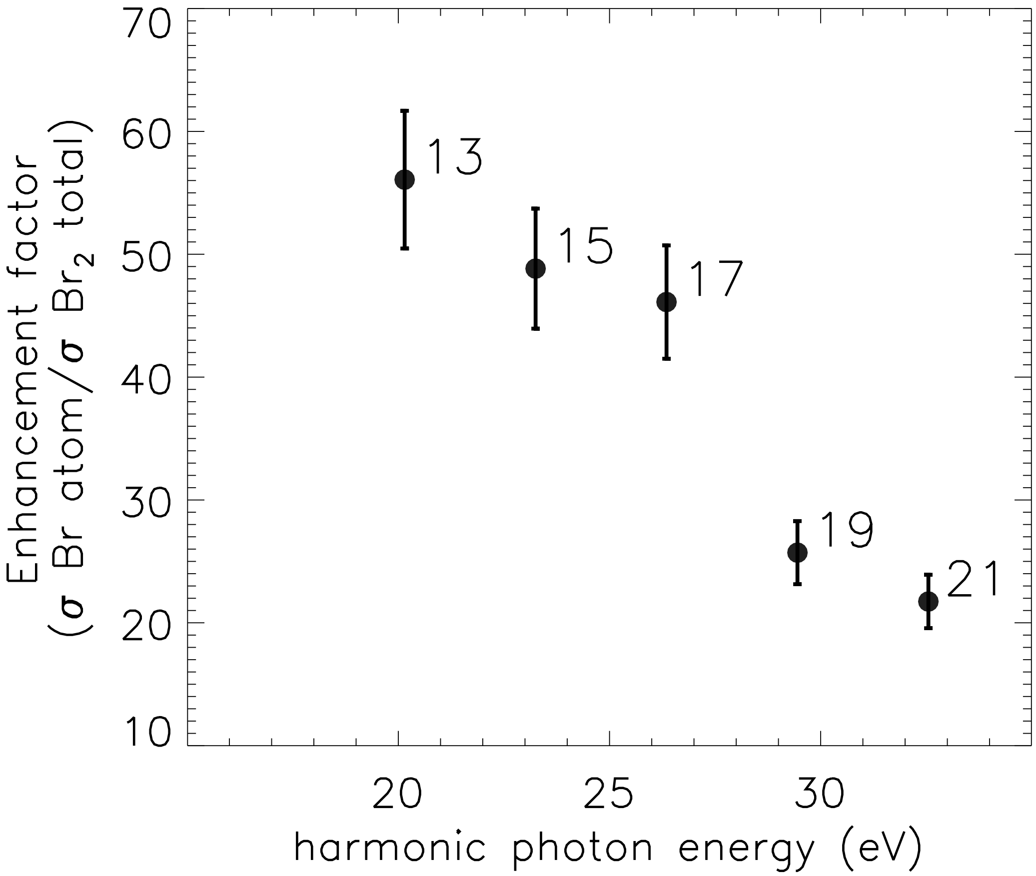

Figure 7.12: The cross-section enhancement factor plotted vs. the harmonic photon energy, demonstrating that the 17th harmonic probe was not sitting on a resonance for atomic Br, but the atom signal is similarly enhanced for several harmonics.

7.6 Conclusions

In a simple molecule like Br_2, we demonstrate the many factors that come into play when measuring ionization from excited states and excited state photodissociation dynamics. These issues have important implications for future pump-probe spectroscopies, specifically with soft x-rays. Electron distributions from excited neutral to ion states, the complication of above threshold ionization features in time-resolved spectroscopy, the time-dependent appearance of atomic photoelectron signals, the enhancement of ionization cross-sections of atomic species vs. molecular species, and the shapes and cross-sections of signals arising from excited transient states are all relatively unexplored phenomena. For neutral gas phase species, UV/visible-pump soft x-ray probe photoelectron spectroscopy proves to be a powerful tool for probing dissociation and excited state dynamics, both in the nanosecond and femtosecond regime.

Bibliography

[1] Atkins. Physical Chemistry. W. H. Freeman and Co., New York, 5th edition, 1994. p. 615.

[2] Johnson, Cutler, Bancroft, Hu, and Tan. High-resolution photoabsorption and photoelectron spectra of bromine-containing molecules at the br 3d edge: the importance of lignad field splitting. J. Phys. B At. Mol. Opt. Phys., 30:4899–4917, 1997.

[3] Greenblatt, Zanni, and Neumark. Time-resolved photoelectron spectroscopy. Science, 276:1675, 1997.

[4] Haight. Photoemission with laser generated harmonics tunable to 80 ev. Applied Optics, 35:6445, 1996.

[5] Cornford, Frost, McDowell, Ragle, and Stenhouse. Photoelectron spectra of the halogens. J. Chem. Phys., 54:2651, 1971.

[6] Hubinger and Nee. Journal of Photochemistry and Photobiology, 86:1, 1995.

[7] Zanni, Taylor, Greenblatt, Soep, and Neumark. Characterization of the i_2^- anion ground state using conventional and femtosecond photoelectron spectroscopy. J. Chem. Phys., 106:19, 1997.

[8] Davies, LeClaire, Continetti, and Hayden. Femtosecond time-resolved photoelectron-photoion coincidence imaging studies of dissociation dynamics. J. Chem. Phys., 111:1–4, 1999.

[9] Fischer, Vrakking, Villeneuve, and Stolow. Femtosecond time-resolved zero kinetic energy photoelectron and photoionization spectroscopy studies of i_2 wavepacket dynamics. Chem. Phys., 207:331–354, 1996.

[10] Vorsa, Campagnola, Nandi, Larsson, and Lineberger. Photofragmentation of i_2^- ar_n clusters: Observation of metastable isomeric fragments. J. Chem. Phys., 105:2298–2307, 1996.

[11] Vorsa, Nandi, Campagnola, Larsson, and Lineberger. Recombination dynamics of photodissociated i_2^- in size selected ar and co_2 clusters. J. Chem. Phys., 106:1402–1410, 1997.

[12] Sanov, Sanford, Nandi, and Lineberger. Spin-orbit relaxation and recombination dynamics in $\mathrm{i}_2^-(\mathrm{co}_2)_n$ and i_2^-(ocs)$_n$ cluster ions: A new type of photofragment caging reaction. J. Chem. Phys., 111:664–675, 1999.

[13] Faeder and Parson. Ultrafast reaction dynamics in cluster ions: Simulation of the transient photoelectron spectrum of i_2^- ar$_n$ photodissociation. J. Chem. Phys., 108:3909–3914, 1998.

[14] Gruebele and Zewail. Femtosecond wavepacket spectroscopy: Coherences, the potential and structural determination. J. Chem. Phys., 98:883–902, 1993.

[15] Ben-Nun, Levine, and Fleming. Solvent-induced nonadiabatic transitions in iodine: An ultrafast pump-probe computational study. J. Chem. Phys., 105:3035–3056, 1996.

[16] Sorensen, Bjorneholm, Hjelte, Kihlgren, Ohrwall, Sundin, Svenson, Buil, Descamps, L'Huillier, Norin, and Wahlstrom. Femtosecond pump-probe photoelectron spectroscopy of predissociative rydberg states in acetylene. J. Chem. Phys., 112:8083–8042, 2000.

[17] Blanchet and Stolow. Nonadiabatic dynamics in polyatomic systems studied by femtosecond time resolved photoelectron spectroscopy. J. Chem. Phys., 108:4371–4374, 1998.

[18] Ferray, L'Hullier, Li, Lompre, Manifray, and Manus. Multiple-harmonic conversion of 1064-nm radiation in rare-gases. J. Phys B, 21:L31, 1988.

[19] McPherson, Gibson, Jara, Johann, Luk, McIntyre, Boyer, and Phodes. Studies of multiphoton production of vacuum ultraviolet-radiation in the rare-gases. J. Opt. Soc. Am. B, 4:825, 1987.

[20] Wahlstrom, Larsson, Persson, Starczewski, Salieries Svanberg, Balcou, and L'Huillier. High-order harmonic-generation in rare-gases with an intense short-pulse laser. Phys. Rev. A, 48:4709, 1993.

[21] Zhou, Peatross, Murnane, and Kapteyn. Enhanced high-harmonic generation using 25 fs laser pulses. PRL, 76:752–755, 1996.

[22] Lewenstein, Balcou, Yu, Ivanov, L'Huillier, and Corkum. Theory of high-harmonic generation by low-frequency laser fields. Phys. Rev. A, 49:2117, 1994.

[23] Sanpera, Watson, Lewenstein, and Burnett. Harmonic-generation control. Phys. Rev. A, 54:4320, 1996.

[24] Corkum. Plasma perspective on strong-field multiphoton ionization. Phys. Rev. Lett, 73:1994, 1993.

[25] Schafer and Kulander. Harmonic generation from ultrafast pump lasers. PRL, 78:638–641, 1997.

[26] Salieres, Antoine, de Bohan, and Lewenstein. Temporal and spectral tailoring of high order harmonics. Phys. Rev. Lett., 81:5544–5547, 1998.

[27] Kan, Capjack, and Rankin. High harmonic generation. Phys. Rev. A, 52:R4336, 1995.

[28] Probst and Haight. Unoccupied molecular orbital states of tris (8-hydroxy quinoline) aluminum: Observation and dynamics. Appl. Phys. Lett., 71:202–204, 1997.

[29] Siffalovic, Drescher, Spieweck, Wiesenthal, Lim, Weidner, Elizarov, and Heinzmann. Laser-based apparatus for extended ultraviolet femtosecond time-resolved photoemission spectroscopy. Rev. Sci. Instr., 72:30–35, 2001.

[30] Bauer, Lei, Read, Tobey, Murnane, and Kapteyn. Direct observation of a chemical reaction on a pt surface with high-order harmonics. 2001.

[31] Haight, Hayden, Longo, Neary, and Wagner. Mars: Femtosecond laser mask advanced repair system in manufacturing. J VAC SCI TECHNOL B, 17:3137, 1999.

[32] Eaton. Studies of nonlinear femtosecond pulse propagation in bulk materials. PhD thesis, University of Colorado, 1999.

[33] Margaritondo. Introduction to Synchotron Radiation, volume p. 59. New York, Oxford University Press,), 1988.

[34] Villoresi. On the optical analysis of the x-ray path-lengths in the diffraction of femtosecond xuv and soft x-ray pulses. Laser and particle beams, 18:529, 2000.

[35] Kruit and Read. Magnetic-field parallelizer for 2-pi electronspectrometer and electron-image magnifier. J. Phys. E. Sci. Instrum., 16:313, 1983.

[36] Turner, Baker, Baker, and Brundle. Molecular Photoelectron Spectroscopy. John Wiley and Sons Ltd, London, 1970.

[37] Wahlstrom, Larsson, Persson, Starczweski, and Svanberg. High-order harmonic generation in rare gases with an intense short-pulse laser. Phys. Rev. A, 48:4709–4720, 1993.

[38] Balcou, Huillier, and Escande. High-order harmonic generation processes in classical and quantum anharmonic oscillators. Phys. Rev. A, 53:3456–3468, 1996.

[39] Svensson, Kikas, Ausmees, Osborne, Aksela, Naves de Brito, and Nommiste. Absolute photoionization cross sections of excited he states in the near-threshold region. J. Phys. B, 28:L293, 1995.

[40] de Lisio, Altucci, Bruzzese, De Filippo, Solimen, Bellini, and Foggi. Harmonic generation in an ionized gas medium with a 100-femtosecond, high repetition rate laser source at intermediate intensities. Appl. Phys. B, 64:323, 1997.

[41] L'Huillier, Lewenstien, Balcou, Salieres, Ivanov, Larsson, and Wahlstrom. Phase-matching effects in strong-field harmonic-generation. Phys. Rev. A, 48:R3433, 1993.

[42] L'Huillier. Generation and applications of high order harmonics: An alternative coherent short-pulse xuv source. Inst. Phys. Conf. Ser., 151:445, 1996.

[43] Salieres, L'Huillier, and Lewenstein. Coherence control of high-order harmonics. Phys. Rev. Lett., 74:3776, 1995.

[44] L'Huillier, Balcou, Candel, Schafer, and Kulander. Calculations of high-order harmonic generation processes in xe at 1064 nm. Phys. Rev. A, 46:2778, 1992.

[45] Cardona and Eds. Ley. Photoemission in Solids I: General Principles. Springer-Verlag, Berlin, 1978. with additional corrections.

[46] Kimura, Yamazaki, and Achiba. He I (584 å) photoelectron spectra and photoionization cross sections of atomic chlorine and bromine. Chem. Phys. Lett., 58:104–107, 1978.

[47] Lappert, Brian Pedley, Sharp, and Guest. Bonding studies of compounds of boron and elements of groups 3-5. J. Chem. Soc. Dalton Trans. 2, 72:539, 1976.

[48] Hufner. Photoelectron Spectroscopy. Springer-Verlag, New York, 1995. p. 365.

[49] Fuggle and Mrtensson. Core-level binding energies in metals. J. Electron Spectrosc. Relat. Phenom., 21:275, 1980.

[50] Masui, Shigemasa, Yagishita, and Sellin. New measurements of the widths of the xe 4d levels. J. Phys. B, 28:4529, 1995.

[51] Ausmees, Osborne, Moberg, Svensson, Aksela, Sairanen, Kivimaki, Naves de Brito, Nommiste, Jauhiainen, and Aksela. Observation of anomalous behavior of the xe 4d photoelectron satellites. Phys. Rev. A, 51:855, 1995.

[52] Chang, Rundquist, Wang, Christov, Kapteyn, and Murnane. Temporal phase control of soft-x-ray harmonic emission. Phys. Rev. A, 58:R30, 1998.

[53] Balcou, Salieres, Budil, Ditmire, Perry, and L'Huillier. Z. Phys. D., 34:107, 1995.

[54] Larsson, Mevel, Zerne, L'Huillier, Wahlstrom, and Svanberg. Two colour time-resolved spectroscopy of helium using high-order harmonics. J. Phys. B, 28:L53–L58, 1995.

[55] Altucci, Delfin, Roos, Gaarde, L'Huillier, and Mercer. Frequency-resolved time-gated high-order harmonics. Phys. Rev. A, 58:3934, 1998.

[56] Pratt. Excited-state molecular photoionization dynamics. Rep. Prog. Phys., 58:821, 1995.

[57] Kimura. Development of laser photoelectron spectroscopy based on resonantly enhanced multiphoton ionization. JOURNAL OF ELECTRON SPECTROSCOPY AND RELATED PHENOMENA, 100:273–296, 1999.

[58] Kimura. Molecular dynamic photoelectron spectroscopy using resonant multiphoton ionization for photophysics and photochemistry. International Reviews in Physical Chemistry, 6:195, 1987.

[59] Kimura, Takahashi, Okuyama, and Plazibat. Application of mpi photoelectron spectroscopy to excited molecules. use of tunable vuv laser radiation. J. of Elect. Spec. and Rel. Phen., 51:383, 1990.

[60] Capelle, Sakurai, and Broida. Lifetimes and self-quenching cross sections of vibrational levels in the b state of bromine excited by a tunable dye laser. J. Chem. Phys., 54:1728, 1971.

[61] Herzberg. Molecular Spectra and Molecular Structure: Spectra of Diatomic Molecules. New York; Prentice-Hall, 1939.

[62] Clyne and Heaven. Theoretical treatment of the spontaneous predissociation of br$_2$ b $^3\pi$. J. Chem. Phys., 76:5342, 1982.

[63] Bouhal, Evans, Grillion, Mysyrowicz, Breger, Agostini, Constantinescu, Muller, and von der Linde. Cross-correlation measurement of femtosecond noncollinear high-order harmonics. J. Opt. Soc. Am. B, 14:950–956, 1997.

[64] Zeek, Maginnis, Backus, Russek, Murnane, Mourou, Kapteyn, and Vdovin. Pulse compression by use of deformable mirrors. Opt. Lett., 24:493–495, 1999.

[65] Peterson and Smith. Chem. Phys., 30:407, 1977.

[66] Kim, McCamant, Shu, and Mathies. J. Phys. Chem. B, 105(2001):1240, 2001.

[67] Clyne, Heaven, and Tellinghuisen. Theoretical treatment of the spontaneous predissociation of br$_2$, b$^3\pi(0_u^+)$. J. Chem. Phys., 76:5341, 1982.

[68] Trembaly, Larzilliere, Combet-Farnoux, and Morin. Photoelectron spectrosocpy of atomic iodine produced by laser photodissociation. Phys. Rev. A, 38:3804–3807, 1988.

[69] Nugent-Glandorf, Scheer, Krishnamurthy, Odom, and Leone. Photoelectron spectroscopic determination of the energy bandwidths of high-order harmonics (7th-55th) produced by an ultrafast laser in neon. Phys. Rev. A, 62:23812–1–7, 2000.

[70] Gisselbrecht, Descamps, Lynga, L'Huillier, Wahlstrom, and Meyer. Absolute photoionization cross sections of excited he states in the near threshold region. PRL, 23:4607–4610, 1999.

[71] Durfee, Rundquist, Backus, Herne, Murnane, and Kapteyn. Phase matching of high-order harmonics in hollow waveguides. PRL, 83:2187–2190, 1999.

[72] Krause, Schafer, and Kulander. Calculation of photoemission from atoms subject to intense laser fields. Phys. Rev. A, 45:4998, 1992.

[73] Shon, Suda, and Midorikawa. Generation and propagation of attosecond pulses in he gas with sub-10-fs driver pulses. Phys. Rev. A, 60:2587, 1999.

[74] Platonenko and Strelkov. Generation of a single attosecond x-ray pulse. Quant. Elec., 28:749, 1998.

[75] Glover, Schoenlein, Chin, and Shank. Observation of laser assisted photoelectric effect and femtosecond high order harmonic radiation. Phys. Rev. Lett., 76:2468, 1996.

[76] Bouhal, Salieres, Breger, Agostini, Hamoniaux, Mysyrowicz, Antonetti, Constantinescu, and Muller. High-order harmonic-generation in rare-gases - a new source in photoionization spectroscopy. Phys. Rev. A, 58:389, 1998.

[77] Ditmire, Crane, Nyuyen, DaSilva, and Perry. Energy-yield and conversion-efficiency measurements of high-order harmonic radiation. Phys. Rev. A, 51:R902, 1995.

[78] Watson, Sanpera, and Burnett. Pulse-shape effects and blueshifting in the single-atom harmonic-generation from neutral species and ions. Phys. Rev. A, 51:1458, 1995.

[79] J.C. Diels and W. Rudolph. Ultrashort Laser Pulse Phenomena. Academic Press, San Diego, 1996.

[80] de Lange. Laser photoelectron spectroscopy: mixed traits of excited states. JOURNAL OF THE CHEMICAL SOCIETY-FARADAY TRANSACTIONS, 94:3409–3419, 1998.

[81] Nilsen, Hansen, Selsto, and Madsen. Laser excitation of angular rydberg wavepackets. JOURNAL OF PHYSICS B-ATOMIC MOLECULAR AND OPTICAL PHYSICS, 32:4995–5007, 1999.

[82] Mecking and Lambropoulos. Nondispersing radial rydberg wavepackets in doubly core-driven two-electron atoms. JOURNAL OF PHYSICS B-ATOMIC MOLECULAR AND OPTICAL PHYSICS, 31:3353–3361, 1998.

[83] RAITHEL, HELD, MARMET, and WALTHER. Rubidium rydberg atoms in strong static fields. JOURNAL OF PHYSICS B-ATOMIC MOLECULAR AND OPTICAL PHYSICS, 27:2849–2866, 1994.

[84] GROCHMALICKI and LEWENSTEIN. Excitation of rydberg wavepackets by short laser-pulses. JOURNAL OF PHYSICS B-ATOMIC MOLECULAR AND OPTICAL PHYSICS, 21:3285–3302, 1988.

Appendix A

Absorption spectrum of Bromine

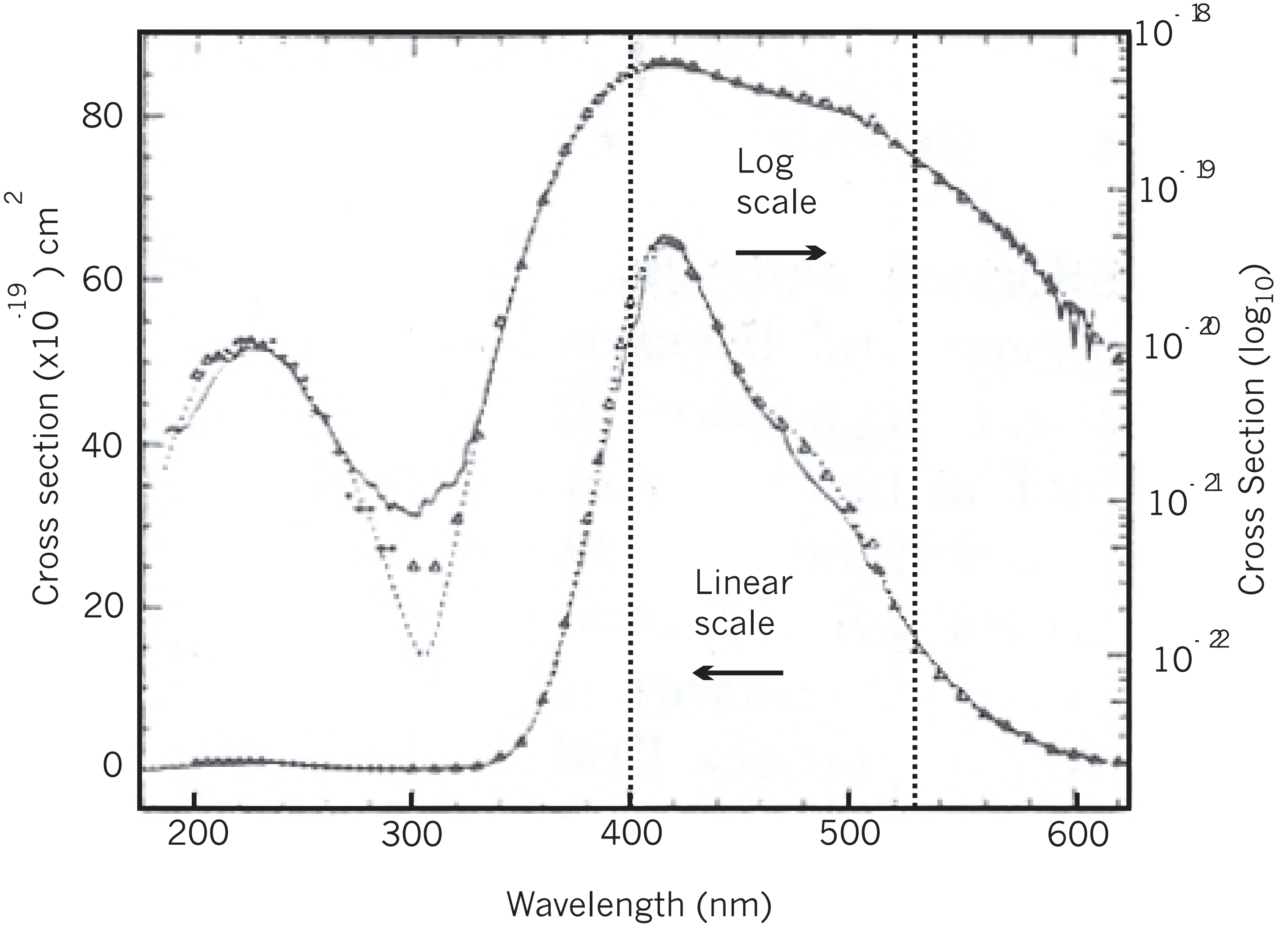

Figure A.1: Absorption spectrum of Br_2 from ref. [6], with lines drawn at 400 nm and 527 nm.

Appendix B

Rydberg wavepackets in Krypton

While looking for a 3+1’ multiphoton photoelectron signature in Kr using ultrafast 266 nm and 800 nm pulses, we inadvertently stumbled across a long lived signal coming from a Rydberg wavepacket excitation. The energy level diagram of Kr is shown in Fig. B.1. Three photons of 266 nm light (black arrows) possess an energy which is slightly below the ionization threshold of Kr, with enough bandwidth to excite a large number of Rydberg levels. At t = 0, when the two pulses overlap, photoelectron signals are observed from a 3+1’ (1), 3+2’ (2), and 3+3’ (3) (overlapped with a 4 photon signal from the 267 only) multiphoton ionization, (where the gray arrows represent the 800 nm photons in Fig. B.1). At long times, however, these photoelectron signals persist at a reduced count rate. An example of the photoelectron spectrum at long time delays (∼500 fs) is given in Fig. B.2. The labels (1), (2) and (3) relate the photoelectron peaks in Fig. B.2 to the photon process in Fig. B.1. There are 3 sets of doublet peaks separated by ∼1.5 eV (the energy of an 800 nm photon). Each doublet represents the spin orbit splitting in the Kr^+ ion. The doublet labeled (1) results from ionization of the Rydberg wavepacket with one 800 nm photon. The second doublet peaks (labeled (2)) are photoelectrons from ionization of the Rydberg wavepacket with 2 photons of 800 nm. The photoelectron peaks labeled (3) do not change with pump-probe delay and are attributed to a 4-photon ionization of Kr with the 266 nm laser.

Taking the total photoelectron counts in the peak at 0.8 eV (leaving the Kr^+ ion in the high energy spin orbit state) from Fig. B.2 and plotting this versus pump-probe delay gives the

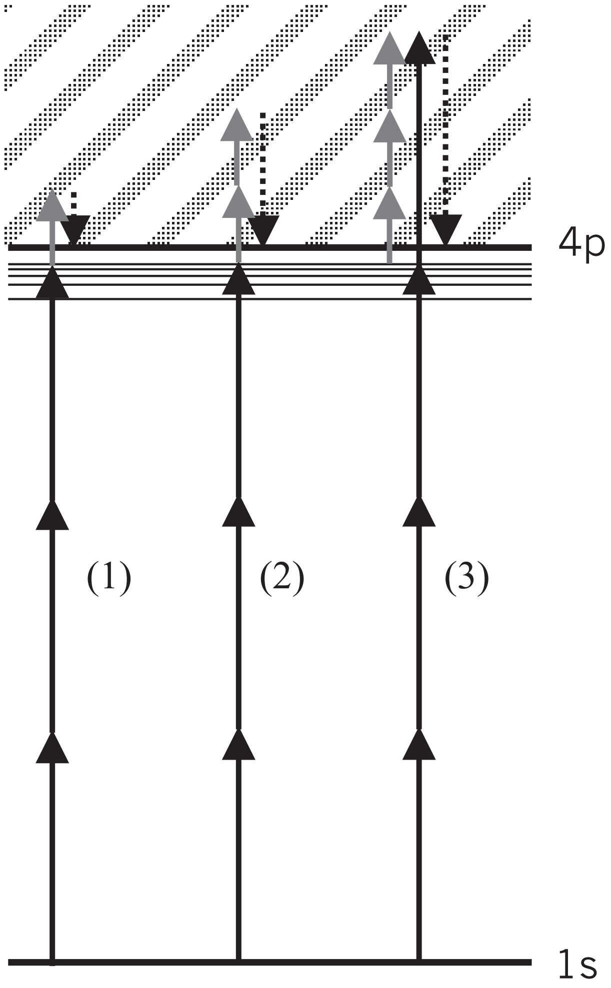

Figure B.1: An energy level diagram showing the excitation of a Rydberg wavepacket in Kr by a 3-photon absorption of 266 nm (black arrows). When an 800 nm pulse (gray arrow) is introduced, the Kr is ionized by a 1, 2, or 3 photon addition of the 800 nm photon. Note that the ionization of Kr with 4 photons of 266 nm is identical in energy to the 3+3’ multiphoton ionization at t = 0.

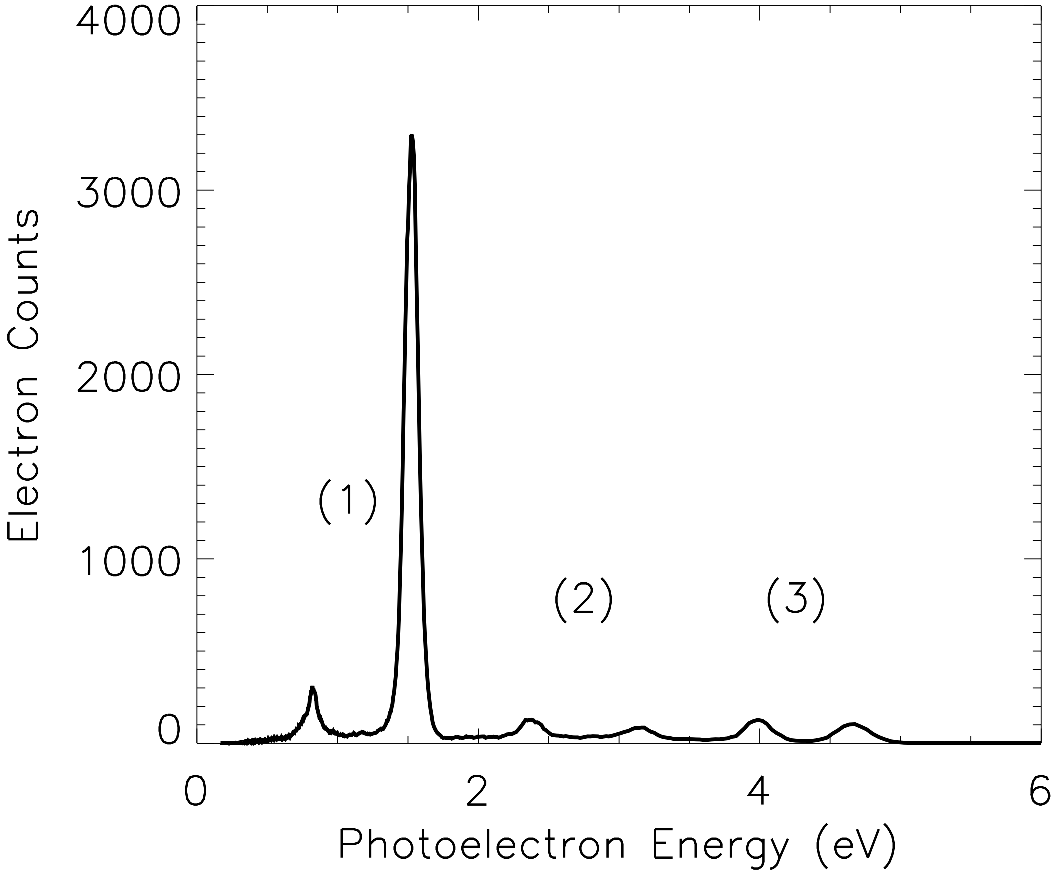

Figure B.2: Photoelectron spectrum of Kr with a time delay between the 267 nm pulse and the 800 nm pulse of 500 fs.

black curve in Fig. B.3. A fast oscillatory structure with a period of $\sim$60 fs is observed on top of a slower oscillation of about 2 ps. The peak at 1.5 eV (leaving the Kr^{+} ion in the low energy spin orbit state) in Fig. B.2 shows primarily the slow 2 ps oscillation (shown as the dark gray line in Fig. B.3). When the black time trace is normalized to the dark gray time trace (effectively taking out the slow 2 ps oscillation), the light gray time trace results, showing only the fast oscillatory structure.

The energy/pulse of the 266 nm beam remained constant at $\sim$60 μJ, but the 800 nm beam was varied in an attempt to understand the oscillatory structure of the photoelectron signals. In Fig. B.3, the 800 nm power was held at 1.4 mJ/pulse. Fig. B.4, however, shows the same time traces as in Fig. B.3, but with the 800 nm beam reduced to 200 μJ/pulse by reducing the first iris inside the chamber (effectively blocking 85% of the beam). The difference between the time-correlation of the two photoelectron peaks (leaving the ion in two different spin-orbit states) is unclear, unless some coupling between spin orbit energy levels and the Rydberg energy levels exists. However, it is still the same 800 nm photon which ionizes the Rydberg wavepacket, and it would seem unlikely that the spin orbit states of the ion would yield different signals.

The Rydberg progressions leading up to the ionization threshold in Kr are given in Fig. B.5, calculated from Charlotte Moore's Rydberg equations. The probability of ionizing a Rydberg wavepacket is greater when the electron is near the nucleus, which is likely the cause of the fast oscillatory structure of the photoelectron signal. The period of the fast oscillation (60 fs or 555 cm^{-1}) could be due to a beating between two Rydberg energy levels. In other words, both energy levels are excited by the bandwidth of the laser and the frequency of recurrence of the wavepacket then becomes the difference in energy between these two states. The energy difference between the ns = 10 and 11 calculated Rydberg levels is 545 cm^{-1}, which is likely well within the error of the experimental measurement (perhaps properly fitting the data with a sin wave would give a more accurate number for the oscillation period with uncertainties, a Fourier transform of the data was attempted, but there are not enough points for a good result). The slow oscillatory structure is more puzzling. In the field of a high peak power laser, the Rydberg levels

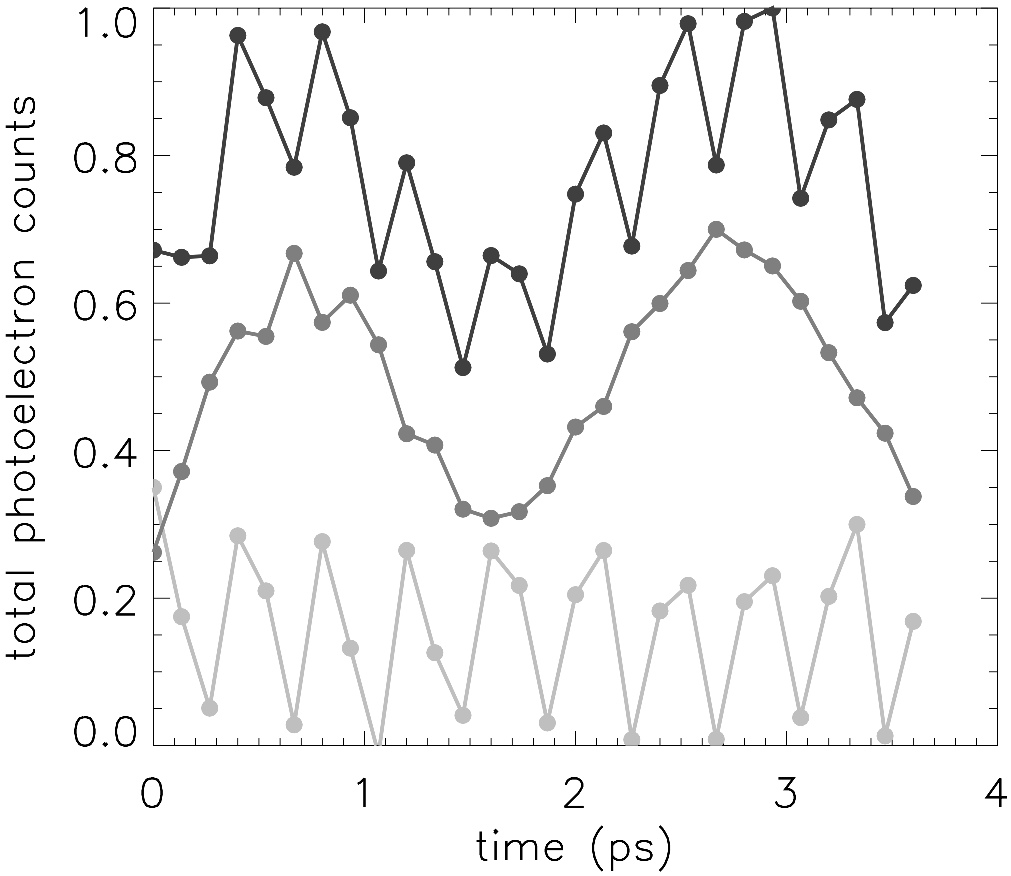

Figure B.3: Time traces of the photoelectron signal resulting from the ionization of a Rydberg wavepacket in Kr. The black trace represents the total counts in the photoelectron peak at 0.8 eV, and the dark gray from the photoelectron peak at 1.5 eV in Fig B.2. The light gray line is the black trace normalized to the dark gray trace, showing the fast oscillatory structure.

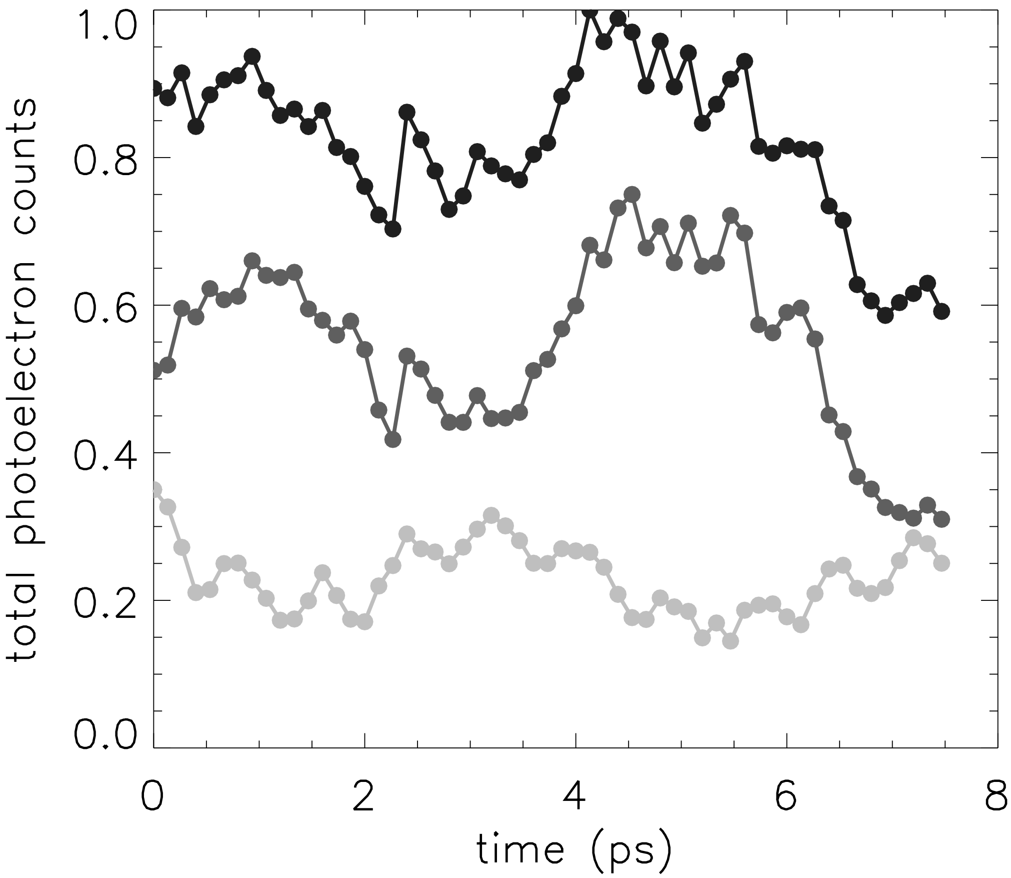

Figure B.4: The same time traces as in Fig. B.3, with the power of the 800 nm beam reduced to 200 mW average power.

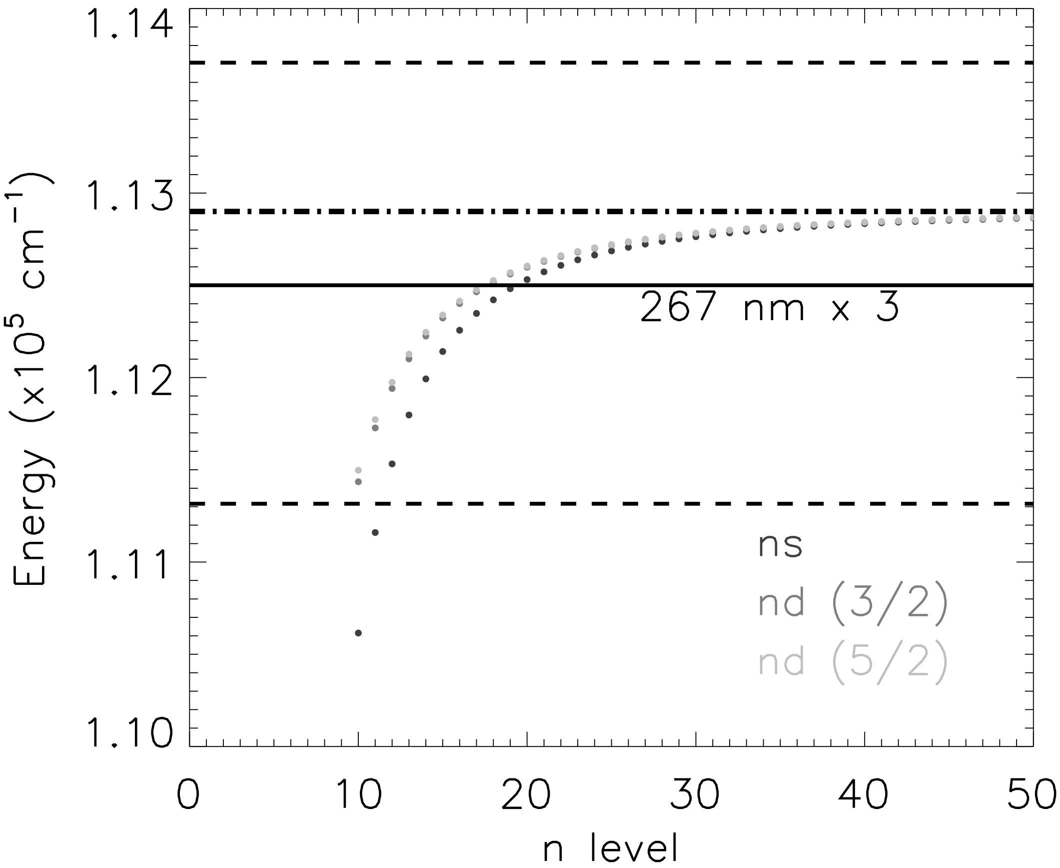

Figure B.5: Rydberg energy levels in Kr, showing the ns, nd3/2 and nd5/2 progressions. The energy of three 266 nm photons is designated by the solid black line. The dotted lines represent the energy bandwidth (FWHM) of the 266 nm pulse.

can be shifted in energy due to an AC stark effect. If a large number of energy levels (shifted to varying degrees) are populated, a slow oscillatory structure from the addition of many faster oscillations could result. The data was never fully analyzed, but some work was done by Ed Grant, which is summed up in a Microsoft Excel file named 'Kr Rydberg states(Ed).xls'. Some helpful references are [81, 82, 83, 84].